

A general self-consistent framework for studying cumulative displacement damage in nanostructured metals based on parameter passing and structural feedback between atomic and coarse-grained techniques

Xiangyan Li^{a, 1}, Yange Zhang^{a, 1}, Yichun Xu^{a, 1}, Xuebang Wu^{a, *}, Xianping Wang^a, B.C. Pan^b, C.S. Liu^{a, **}, Q.F. Fang^a, Jun-Ling Chen^c, G.-N. Luo^c, Zhiguang Wang^d, X. Liu^e

^a Key Laboratory of Materials Physics, Institute of Solid State Physics, Chinese Academy of Sciences, P.O. Box 1129, Hefei 230031, PR China

^b Hefei National Laboratory for Physical Sciences at Microscale and Department of Physics, University of Science and Technology of China, Hefei 230026, PR China

^c Institute of Plasma Physics, Chinese Academy of Sciences, Hefei 230031, PR China

^d Institute of Modern Physics, Chinese Academy of Sciences, Lanzhou 730000, PR China

^e Southwestern Institute of Physics, Chengdu, Sichuan 610041, China

E-mail: xbwu@issp.ac.cn and csliu@issp.ac.cn (C.S. Liu)

¹ These authors contributed equally to this work.

Abstract

Nano-crystalline metals (NCs) exhibit radiation-tolerance due to the sink of grain boundaries (GBs) for radiation-induced defects such as self-interstitial atoms (SIAs) and vacancies (Vs). However, the relevant mechanisms for the radiation damage accumulation and GB structural relaxation under high radiation field in NCs are still not well understood due to the lack of self-consistent across-scale techniques for simulating radiation-induced microstructures evolution. In this article, by combining coarse-grained and atomistic simulations, we proposed a coupling method to investigate the evolution of the microstructure and SIA/V-GB interaction under cumulative irradiation in NC iron. The SIA overloaded effect was revealed in iron GBs at a high radiation dose rate and/or low temperature. Two types of GB structural response were observed to cumulative irradiation. With the SIA accumulated at the GB, the new GB phase formed and then a critical concentration of the SIA at the GB transited to the small quantity of the V during the GB structural recovery, accompanied by the local GB motion. Consequently, the GB's role for Vs nearby alternated between the trapping and annihilation center with radiation dose. Alternatively, GB developed to a

disordered structure after trapping abundant SIAs. The GB response pattern to cumulative irradiation that is related to the SIA formation energy at the GB or the GB thermal stability is well manifested in the cumulative distribution function of the defects formation energy and its energy level density. The present work reveals the dynamic healing picture for radiation damage near the GB under cumulative irradiation.

Keywords: nano-crystalline; grain boundary; radiation-resistance; structural relaxation; self-healing

1. Introduction

Current and future generation nuclear reactors call for structural materials with outstanding properties that can withstand hundreds of atomic displacements per atom (dpa) produced by neutron damage []. Radiation to the material creates defects of self-interstitial atoms (SIAs), vacancies (Vs) and their clusters (V_n/SIA_n) in the material []. These defects often induce the degradation of materials performance in terms of irradiation dislocation hardening, creep, void swelling, and helium embrittlement []. Engineering materials with a high density of defect sinks, such as GBs in nano-crystalline metals (NCs) with the grain size below 100 nm, has been proved to be one of the fundamental options for mitigating these deleterious effects over the past 50 years []. The novel radiation resistance of NCs is apparently manifested by the formation of a defect denuded zone near the GB, as observed in irradiation experiments of metals [] and oxides []. Quite recently, the NCs iron (Fe) with high thermal stability have been prepared successfully [] and see a promising application in extreme irradiation environments [].

Until now, great effort has been made to reveal the atomic origin of the radiation-tolerance of NCs, focusing on the fundamental interactions of the V/SIA with the GB in several metals []. It is found that the GB has two basic roles either as a trapping center for the SIA/V or as the annihilation catalyst for the SIA-V recombination. On the one hand, the trapping of the SIA/V by the GB suppresses the formation of the large immobile defect clusters in the grain interior, leading to the low defect density in the grain interior in NCs. The mechanism is supported by the rate theory models of the grain size effect on the GB sink strength [], the in-situ observation of defect cluster absorption by GBs in Kr ion irradiated NC nickel []. Atomic simulations suggest that the low V/SIA formation energy at the GB and low diffusion energy barrier near the GB acts as the respective energetic and kinetic driving force for the V/SIA segregation to the GB []. On the other hand, several distinct annihilation mechanisms/processes have been proposed in recent years []. In NC copper (Cu), the SIA was observed to firstly segregate to the GB and then recombine from the GB. Consequently, the V near the GB was efficiently annihilated via a low energy barrier process. Such interstitial emission (*IE*) was

shown to work near the GB/surface in Fe, tungsten (W), and Cu []. Recently [], it was found that the SIA motion along the GB carrying with the low-energy barrier annihilation region around the SIA coupled with the diffusion of the V towards the GB could also anneal radiation damage in NC Fe []; the coupling mechanism also applies to SIA-V annihilation in W and Cu GBs/surfaces []. The SIA-cluster was found to be reflected back into the grain interior as approaching the locally dense GB and annihilate the V near the GB in W [], although the SIA-V annihilation could be via the *IE* and coupling mechanisms near the locally loose GB region.

Despite these advances, significant scientific questions remain unanswered, such as how the microstructure near the GB evolves and how the GB relaxes under a harsh cumulative irradiation condition. Given that the experimental observation was conducted after a certain radiation dose, the defects accumulation and GB relaxation mechanisms are critical to understanding the final experimental observations. First, the complex experimental conditions and multiple SIA/V-GB interatomic processes render the defects accumulation and GB structural relaxation mechanism hard to access. As illustrated in supplementary Fig. S3, the experimental conditions consist of multiple parameters spanning a large range (supplementary Table S1), including radiation conditions of temperature (T), radiation dose (rd) and radiation dose rate (τ), and the grain size (L). The radiation response of the GB is related to the atomic processes in the bulk, near the GB and within the GB, and also the process associated with GB motion. In different parameter regimes, the system could have various defects accumulation mechanisms, involving distinct atomic processes. Second, one also has simulation technique challenge facing the prediction of the response of the GB to cumulative irradiation damage of a certain dose due to the possible evolution of the SIA/V-GB interaction with radiation dose. The popular simulation methods for exploring cumulative irradiation response of NCs are molecular dynamics (MD) and object kinetic Monte Carlo (OKMC) []. In MD simulation of cumulative irradiation damage, the repeating ion bombardments with certain kinetic energy continuously hit the simulation cell at a certain incident angle at an certain time interval, as

performed in Fe [], and Cu []. Chen et al. discovered that the SIA-V annihilation at GBs was mediated by the formation of chain-like defects []; they concluded that the GBs act as highly efficient defect sinks that cannot saturate under extreme radiation conditions. Using similar methods, Jin et al. found the synergistic motion of the stacking fault tetrahedra and GBs under repeated bombardments to the GB in Cu []. Our simulations on a Fe GB also revealed such mechanism (supplementary Figs. S1 and S2). Although these MD simulation results reveal the cascade-GB interaction, the short simulation time interval (an inherent limitation of MD) between collision cascades yields a dose rate several orders of magnitude higher than that in experiments. As a result, the revealed microstructure relaxation mechanism/process near the GB may not occur in the other parameter regime of the real experiments. Alternatively, with the basic SIA/V-GB interaction processes as input, the long-time evolution of the radiation-induced microstructure could be accessed by OKMC. However, the OKMC model would fail to work if new process emerges as defects accumulate with radiation dose. Therefore, in the OKMC model it requires not only the fundamental atomic processes to drive the microstructure evolution but also the feedback on the modification of the processes from the microstructure subjected to a specific dose of radiation. Such coupling between coarse-grained and atomistic simulation is critical for accurately accessing the long-term radiation response of NCs, which may also be encountered in stochastic cluster dynamics (SCD) simulation of defects accumulation inside Fe grains and in GB [].

In this work, we proposed a computational *predictor-corrector* framework for simulating displacement damage accumulation and structural relaxation in NC Fe by combining molecular statics (MS), MD and OKMC. The method takes advantage of the coarse-grained technique to access the long term evolution of the microstructure and the atomic technique to explore the structural transition. The atomic model with reproduced defect structure at a radiation dose drawn from OKMC simulations was relaxed by using MD at a certain temperature. As a feedback of atomistic simulations to OKMC, the new relaxation process was reconsidered in the OKMC model to correct the initial OKMC simulation results. In addition, via calculating

cumulative distribution function for the defect energy level and its density, the fine and sensitive method was developed for characterizing the modification of the whole and local GB structures and the GB's role for the V by the SIA segregation. NC Fe was chosen as a prototypical model system since ferritic steels with body-centered cubic (bcc) α -Fe as the matrix structure are widely used in nuclear reactors as structure materials []. Besides, the basic defect properties, e.g. defect formation energy, diffusion energy barrier and defect-GB binding energy in Fe are of the same order of magnitude as that in Cu, Ag and Au []. The present results may exhibit universality. In the parameter regime of a high dose rate, a low temperature and a small grain size considering experimental conditions [], the SIA overloaded effect was revealed in Fe GBs and an alternating evolution of GB structure and the role of trapping and annihilation of Vs was reported.

2. Computational method

2.1. Interatomic potential and GB models

2.1.1. Interatomic potential

The inter-atomic potential proposed by Mendelev et al. as part of their embedded-atom-method [39] (Potential 2 in Ref. [39]) was used to model the inter-atomic interaction in Fe. Tests show that this potential correctly predicts the properties of the point defects, e.g., the V/SIA formation energy (1.71/3.53 eV) and diffusion energy barrier (0.63/0.33 eV), and the stable configuration of the SIA in the bulk Fe ([110] dumbbell) []. The potential has been widely used for studying radiation damage and defect behavior in Fe [].

2.1.2. Atomic GB models

The atomic GBs studied in this work include 13 high-angle and small-angle symmetric tilt GBs with two kinds of the tilt axes of $[0\ 0\ 1]$ and $[1\ 1\ 0]$. These GBs are $\Sigma 5(210)/[001]$, $\Sigma 5(310)/[001]$, $\Sigma 13(510)/[001]$, $\Sigma 13(320)/[001]$, $\Sigma 25(430)/[001]$, $\Sigma 85(760)/[001]$, $\Sigma 85(13\ 1\ 0)/[001]$, $\Sigma 3(111)/[110]$, $\Sigma 3(112)/[110]$, $\Sigma 9(114)/[110]$, $\Sigma 9(221)/[110]$, $\Sigma 11(113)/[110]$, $\Sigma 11(332)/[110]$. The GBs have been frequently modeled []. The creation and relaxation procedures are identical to the previously reported

procedures [29]. Periodic boundary conditions were applied in the two directions parallel to the GB plane. The vacuum of 15 Å was added in the direction normal to the GB plane and the size in the direction is about 30 Å. The GB system energy was minimized through the rigid-body translations of one grain relative to the other, followed by the full atomic relaxation in all three Cartesian directions at 0 K. After relaxation, the GB energy density (E_{GB}) per unit area, as defined in Ref. [], was calculated. The relaxed GB structures are shown in supplementary Fig. S4. It can be seen, different GBs have distinct structures. Similar GB structures are obtained in other work []. It is found that the twin boundary of $\Sigma 3(1\ 1\ 2)/[1\ 1\ 0]$ (supplementary Fig. S4(i)) has the lowest E_{GB} of 0.26 J/m² due to smaller distortion compared to other GBs; similar structure-energy relation was found in W []. The GBs of $\Sigma 3(1\ 1\ 1)/[1\ 1\ 0]$ (supplementary Fig. S4(h)) and $\Sigma 9(2\ 2\ 1)/[1\ 1\ 0]$ (supplementary Fig. S4(k)) have higher E_{GB} of about 1.3 J/m². In the main text of the article, these GBs will be shown to have rather different defects accumulation and structural relaxation properties, which is correlated with E_{GB} . The stability of the GB structure was also investigated by performing MD simulations at 300 K for about 50 pico-seconds (ps). The velocity-Verlet algorithm was employed to solve the Newton motion equation. The time-step was set 2 femto-seconds (fs).

2.1.3. Coarse-grained GB models

For OKMC simulating defects accumulation in NCs, the coarse-grained GB models of the square-shaped cubic cells are built (Fig. 1(a)). Periodic boundary conditions were applied in the three Cartesian directions. Based on the previous atomic calculations of the basic SIA/V properties near the GB[], the whole model was divided into the bulk region, the region nearby the GB and the GB plane. In the three regions, the defects have corresponding energetic and kinetic properties, simplified by using different physical pictures in the following text. In the OKMC model, the different regimes of the τ - L - T space were accessed with specific defect-GB interaction parameters. The values of these parameters of τ , L , T were assigned based on experimental conditions [] in order to make comparison of the theoretical simulation results with the experimental results []. Parameter τ was assigned to be three levels of 10^2 , 10^{-2} and 10^{-5}

dpa·s⁻¹; L was given of 10, 50, 100 and 200 nm; T was given of 100, 200, 300 and 600 K [实验]. The purpose of choosing different values of the relevant parameters is to explore parameter-regime dependence of the defects accumulation and SIA/V-GB interaction pictures. The other defect-GB interaction parameters were obtained from MS calculations. For a large L , it is hard to reach several dpa in a three-dimensional (3D) GB model due to the large number of objects included in the model. The two-dimensional (2D) GB models were thus also built, while in 3D models L was only given 10 nm.

2.2. Framework of the predictor-corrector method for simulating displacement damage accumulation and structural relaxation in NC-Fe

The proposed *predictor-corrector* method combines the MS, OKMC and MD, as illustrated in Fig. 1(b). The MS was adopted to parameterize a set of unit processes/events. In addition to the defect production, the fundamental atomic processes include diffusion of the V_n/SIA_n , annihilation of the $V_{n1}-SIA_{n2}$, clustering of the V_n/SIA_n , dissolution of the V_n/SIA_n in the bulk, near the GB and within the GB, and emission of the V_n/SIA_n from the GB. These basic processes drive the microstructure evolution from one basin to another. Since all the unit processes about the behavior of a single V_n/SIA_n or V_n-SIA_n interaction near the GB known have been incorporated into the model, it is expected that the model is accurate enough to describe the structural evolution as the radiation dose is lower than a certain level. The OKMC model at this stage gives the SIA_n/V_n distribution and concentration with radiation dose, as illustrated in Fig. 1(b) by the curve of $C_{SIA,V} \sim dose$. The OKMC modeling method based on MS-characterized basic processes during this stage was termed as the *predictor*.

The next step is the *corrector*. The curve $C_{SIA,V} \sim dose$ was sampled to obtain the corresponding defects distribution at a specific radiation dose and at an elevated temperature. The atomic model with reproduced defect structure at a radiation dose was relaxed by using MD at a certain temperature. And then, the defects properties of the model were calculated by the MS. After the procedure, the $C_{SIA,V}$ dependent E_{GB} and SIA/V-GB interactions were obtained, as illustrated by the curve of $E_{GB} \sim C_{SIA,V}$ (Fig. 1(b)). Once new atomic

process was found, the process was again incorporated into the OKMC model to correct the initial OKMC prediction of the microstructure evolution based on the new set of unit processes of the V_n/SIA_n . In principle, the prediction-correction procedure is repeated. The details of the *predictor-corrector* method are described as follows.

2.2.1. MS calculation of the V/SIA properties near the GB

MS was used to calculate fundamental interaction parameters of the SIA_n/V_n with the GB, including V/SIA formation energy ($E_{V/SIA}^f$) [], V/SIA-GB binding energy, V/SIA diffusion energy barriers near the GB and within the GB, V-V/SIA-SIA binding energy within the GB. Results for $\Sigma 5(310)/[001]$ are summarized in supplementary Fig. S5. Based on the defects formation energy, the stable configurations of the defects at the GB were meanwhile found; the V/SIA configurations at the other several GBs are shown in supplementary Fig. S6. Note that, the stability of the site for the V/SIA was also examined at 300 K by using MD. It is found that the site only for di-V/SIA obtained at 300 K is slightly different to that at 0 K. The energy difference is less than 0.2 eV. The V/SIA segregation energy, characterizing the energetic driving force for a V/SIA to segregate to the GB from the bulk, was defined as the reduction in the system energy as the defect migrates to the GB from the grain interior, which equals the bulk defect formation energy minus the defect formation energy at the GB. In some other references, the segregation energy is also termed as the V/SIA-GB binding energy.

The energy barrier for the V/SIA to overcome to be reemitted from the GB ($E_a^{VE/IE}$) was also defined. The barrier equals the sum of the V/SIA diffusion energy barrier in the bulk and the V/SIA segregation energy. The time needed for the V/SIA emission from the GB ($t_{VE/IE}$) was calculated via $t_{VE/IE} = \nu_0^{-1} e^{E_a^{VE/IE}/k_B T}$, where prefactor ν_0 was given 10^{12} /s, Boltzmann constant k_B has a value of 8.517×10^{-5} eV/K, and T is the system temperature. To show whether the V/SIA tends to be clustered within the GB, the binding energy of the V-V/SIA-SIA at the GB ($E_b^{V-V/SIA-SIA}$) was defined. $E_b^{V-V/SIA-SIA}$ was calculated by $E_b^{V-V/SIA-SIA} = 2E_{V/SIA}^f - E_{V_2/SIA_2}^f$. By this definition, a positive value of the binding energy means attraction between two Vs/SIAs, while a

negative value indicates the repulsion between the two defects of the same type.

The standard nudged-elastic-band (NEB) method [38] was employed to calculate the V/SIA migration energy barriers near the GB and along the GB. As calculating the V/SIA migration along the GB, the GB was termed as a two-dimensional plane. Two non-equivalent migration paths were determined. To do this, the energy barriers along all the possible migration paths connected from the initial site to the other two nearest sites were calculated. For example, for the V diffusion from site A to B, the common nearest site C of sites A and B was firstly searched. The energy barriers along the paths A-B and A-C-B were then calculated; the path with the minimal energy barrier was chosen as the most kinetically favorable one in the direction from A to B. Similarly, the migration with low energy barrier on the other direction was calculated. The states that have been relaxed for calculating defects formation energy were employed as the possible initial and final states of a diffusion process. The dense images of 28 intermediate images were inserted between the initial and final states by using the linear interpolation method.

2.2.2. Model assumption and parameters for the OKMC simulating V/SIA accumulation in NC Fe

Based on the spherical approximation of an object (Fig. 1(d–e)), the radius of an object of the V_n/SIA_n was defined as follows:

$$\frac{4\pi}{3}R^3 = n\frac{a_0^3}{2}, r(n) = R + r_{shell}, \quad (1)$$

where a_0 is the lattice constant of 2.855 Å. As shown in Eq. 1, the radius of an object ($r(n)$) includes two parts: the core part R and the shell part r_{shell} . Considering the large stress filed of the SIA_n in the bulk, r_{shell} for a bulk SIA_n was given a larger value than that for the bulk V_n . By definition, the radius for a SIA_n/V_n in the bulk and within the GB is given by Eqs. 2–5, as follows:

$$r(bulk, V, n) = 5.0 + a_0 \times \left(\frac{3\pi}{8}\right)^{1/3} \times n^{1/3}, \quad (2)$$

$$r(bulk, SIA, n) = 7.5 + a_0 \times \left(\frac{3\pi}{8}\right)^{1/3} \times n^{1/3}, \quad (3)$$

$$r(GB, V, n) = 5.0 + a_0 \times \left(\frac{3\pi}{8}\right)^{1/3} \times n^{1/3}, \quad (4)$$

$$r(GB, SIA, n) = 5.0 + a_0 \times \left(\frac{3\pi}{8}\right)^{1/3} \times n^{1/3}, \quad (5)$$

In Eqs. 2–5, the radius is in unit of Å. Note that, only when the two defects are both in the bulk or both at the GB, the defects were viewed as spherical objects. As we treated the interaction of the V_n nearby the GB with the SIA_n at the GB, the SIA_n within the GB was given a limited radius such as 10.0 Å because of the localization of the SIA composing the SIA_n at the GB (Fig. 1(d)).

In the OKMC model for simulating cumulative irradiation damage in nano-crystal Fe, for a transition with an energy barrier of E_m , the rate r was calculated via $r = \nu_0 \exp[-E_m / (k_B T)]$. The detailed procedure for calculating r of different types of events is as follows.

(a). Defect production

For a given dose rate τ and grain size L , the SIA/V production rate ($rcVI$) was calculated by $rcVI = \frac{V_{model}}{V_{atom}} \times \tau$, where the volume of the calculation cell (V_{model}) is L^3 and the volume of an atom (V_{atom}) is $\frac{a_0^3}{2}$. Note that, in a 2D OKMC GB model, V_{model} is L^2 and V_{atom} is $\frac{a_0^2}{2}$. As the defect production event was chosen during the implementation of the OKMC program, a pair of V and SIA was placed randomly in the calculation cell.

(b). Diffusion of the V_n/SIA_n in the bulk, near the GB and within the GB

Within the three regions, the V_n/SIA_n migrates over half the lattice constant each time in one direction. Diffusion of the V_n/SIA_n in the bulk was set to be 3D random walk. Only the small V_n with n less than 5 was set to be possibly mobile at an elevated temperature (at a high temperature, such simplification may be insufficient to correctly predict the microstructure evolution). The energy barrier for the small V_n/SIA_n diffusion in the bulk was from Ref. [1]. Considering higher mobility of the SIA_n than the V_n , only SIA_n with n larger than 10 was set to be immobile, while the barrier for the SIA_n ($3 < n < 10$) diffusion was set to be that for SIA_3 (the size limit set here for the mobile V_n/SIA_n ensures the preferential absorption of the SIA_n by the

GB over the V_n). The diffusion energy barriers for the bulk SIA_n/V_n are summarized in supplementary Table S2.

The physical picture for the V_n/SIA_n behavior near the GB considered in the OKMC model includes GB-enhanced diffusion of the V_n/SIA_n nearby. Diffusion of a V_n/SIA_n near the GB was considered to be one-dimensional walk. Only the V_n with n less than 5 was considered to be possibly trapped by the GB (such approximation may not hold true at a high temperature, as proofed by the absorption of defects clusters by the GB in experiments []). The energy barrier for the GB trapping of the V_n was set to be a half of the barrier for the V_n diffusion in the bulk given the accelerated diffusion of the V_n by the GB []. Since the SIA_n near the GB was spontaneously trapped by the GB, the energy barrier for the SIA_n migration near the GB was set to be zero. The energy barriers for the SIA_n/V_n migration near the GB are shown in supplementary Table S2. The up limit of n was set 500. The trapping radius of the GB for the V_n and SIA_n was set to be 5 and 10 Å, respectively. To execute the trapping of a V_n/SIA_n by the GB, the V_n/SIA_n was put at the GB plane. In the present square-shaped model, there are three GB planes. The plane with the shortest distance from the V_n/SIA_n traps the V_n/SIA_n . The simplified picture is illustrated in Fig. 1(d) and (f). Diffusion of the V_n/SIA_n within the GB was modeled to be 2D; only the single V/SIA was considered to be mobile within the GB (Fig. 1(e)). The energy barriers for the V_n/SIA_n migration on the two nonequivalent directions within the GB are shown in supplementary Tables S3 and S4.

(c). Annihilation of the V_{n1} - SIA_{n2} in the bulk, near the GB and within the GB

As both the V_{n1} and SIA_{n2} are located in the bulk or within the GB, the energy barrier for the annihilation of the V_{n1} with SIA_{n2} was set to be zero. For the annihilation of the V_{n1} near the GB with the SIA_{n2} at the GB (Fig. 1(f)), the considered annihilation mechanisms include the annihilation induced by the SIA-emission [] and the V-hop []. Given the results of MS calculations that reveal the formation of the spontaneous annihilation region surrounding the SIA_n at the GB [], the radius of such region was set to be 5 Å. Out of the region, the energy barrier for the recombination varies lineally with the distance of the V_{n1}

from the border of the annihilation region; the barrier converges to the value for the V_{n1} migration in the bulk. The approximation picture is illustrated in Fig. 1(f). After annihilation, the defect with a larger size survives with the reduced size of $|n1 - n2|$.

(d). Clustering of the V_n/SIA_n in the bulk and within the GB

The energy barrier for the V clustering in the bulk was set to be half that for the single V migration in the bulk. Only the cluster V_n with n less than 5 was allowed to be trapped by another V_n . Considering the high mobility of the SIA, the energy barrier for the SIA clustering in the bulk was set to be zero.

For the SIA/V clustering within the GB, the energy barrier was set to be the half of the minimal barrier for the V/SIA migration along the GB if the binding energy of the V-V/SIA-SIA is positive; otherwise, the barrier for the clustering was assigned to be the V/SIA migration energy barrier along the GB minus the V-V/SIA-SIA binding energy. Only the single V/SIA was allowed to be trapped by another cluster. The binding energies are given in supplementary Tables S5 and S6.

(e). Dissolution of the V_n/SIA_n in the bulk and within the GB

Each time, only one V/SIA was dissolved from the V_n/SIA_n . The energy barrier for the V/SIA dissolution from a V_n/SIA_n in the bulk and within the GB was set to be the sum of the migration energy barrier for the single V/SIA and the binding energy of the V- V_n/SIA_n in the corresponding region. Only small clusters with n less than 4 were allowed to be dissolved. To execute the V/SIA dissolution from a V_n/SIA_n , a V/SIA composing the V_n/SIA_n was put at a site that is d away from the V_n/SIA_n ; distance d is the sum of radius of the V_{n-1}/SIA_{n-1} and that for the V/SIA plus 10 Å to avoid the re-trapping of the V/SIA by the V_n/SIA_n in the next OKMC step.

(f). Emission of the V_n/SIA_n from the GB

The energy barrier for the V_n/SIA_n emission from the GB is the sum of the V_n/SIA_n segregation energy and the V_n/SIA_n migration energy barrier in the bulk, as listed in supplementary Tables S7 and S8. Each

time, only one of the V/SIA of the V_n/SIA_n was emitted from the GB. During executing the emission event, the emitted V/SIA was put the bulk site that is d away from the GB. To avoid the subsequent frequent re-trapping of the V/SIA by the GB, the distance d was set to be the GB trapping radius for the V/SIA plus 5 Å. Note that the emission described here is different to the SIA-emission that induces the annihilation of the V nearby [], which is the atomic detail for the V-SIA annihilation near the GB.

We found that, as all the atomic processes in the bulk, near the GB and along the GB were incorporated into the model, the long timescale or high radiation dose could not be accessed in some cases. The preferentially segregated SIA at the GB was observed to frequently migrate within the GB at high temperature, and consequently the V in the bulk region nearly remained immobile. In these cases, the diffusion of the V/SIA along the GB was inhibited. In the one hand, such picture corresponds to the GB with large V/SIA diffusion energy barrier along the GB. In the other hand, in the case of the very small barrier for the V/SIA along the GB, such assumption implies that the SIA quickly adjusted its position during the occurrence of other events.

2.2.3. Details for MD simulating GB thermodynamics under different levels of V/SIA concentration

With the defects distribution in hand, the structure and energetics of the GB under different levels of V/SIA concentration were investigated. After loading a certain number of the V/SIA into the GB, the system was firstly relaxed at 0 K by using the steepest descent method, followed by the MD relaxation at 300 K. After the relaxation, the E_{GB} and corresponding structure with a certain V/SIA concentration were obtained. To obtain the statistical results of the GB structure and E_{GB} , 10 distinct MD simulations were performed.

To access more discrete V/SIA concentration values at the GB, the number of the structural unit in the two directions parallel to the GB varies. Depending on the size of the minimal structural unit of a GB, the number lies in the range 2–5. In addition, different SIA loaded styles were considered given the short time scale of MD and the resulted possibly metastable state of the GB with the loaded defects. In Style1 (Fig. 1(g)), the site for the single SIA/V occupation within the GB is first found based on the calculation of the

energetic property of the SIA/V near the GB. Then, a certain number of SIAs/Vs are put at these sites to produce the required SIA/V concentration. It could expect that such style would generate a defect structure close to the stable state under a low dose. In Style2 (Fig. 1(h)), the SIA/V is put near the GB one at a time, followed by the MD relaxation at a certain temperature, e.g. 300 K. The sequentially added SIAs/Vs are finally trapped at the GB.

To characterize the GB structure with different concentrations of defects, some other more effective methods were developed in addition to the E_{GB} and the visualization method. Because, the GB was found to develop to many rather different local structures under accumulated radiation damage, while E_{GB} measuring the stability of the whole GB structure, is insensitive to the local GB structure. Based on the V formation energy near the GB with a certain SIA concentration at the GB (C_{SIA}^{GB}), we calculated the cumulative distribution function of the defects energy level and the density of a specific energy level. The distribution function and density were found to be sensitive to the distinct local GB structures.

For a given GB with a certain concentration of SIAs, the V formation energy at the sites within the range with a radius of 10 Å was calculated. Results suggest that, such width of the range is large enough for covering the region affected by the GB. The defects energy level cumulative distribution function ($C(E_V^f)$) is calculated as

$$C(E_V^f) = \frac{\sum_i N_i(E_{Vi}^f \leq E_V^f)}{N_{tot}}, \quad (6)$$

where N_i is the number of sites with E_{Vi}^f less than E_V^f , and N_{tot} is the total number of sites in the calculation region. $C(E_V^f)$ could give the cumulative probability of the V with a certain energy level (E_V^f). Generally the V near the GB has multiple discrete levels of the formation energy near the GB [], which makes the occurrence of the terrace on the $C(E_V^f)$ curve. The E_V^f of the end point of the terrace defines the V energy level. Note that, since only the sites near the GB are underlined, the sites in Eq. 6 are restricted to ones with E_{Vi}^f less than the bulk V formation energy a certain value, e.g. 0.3 eV. Otherwise, the bulk sites take a too large fraction of the calculated region to effectively analyze the evolution of the site property (trapping or

annihilation) with radiation dose.

According to the physical meaning of the E_V^f (e.g. a negative value of E_V^f often indicates the instability of the site and the spontaneous annihilation of the V with the SIA []), the $C(E_V^f)$ was further divided into several regimes. The site density within a specific regime (C_{reg}) was calculated as

$$C_{reg} = N_{tot} \times [C(E_{Vj}^f) - C(E_{Vi}^f)] / S_{GB}, \quad (7)$$

where E_{Vi}^f and E_{Vj}^f are the lower and upper limits of the E_V^f in the regime, and S_{GB} is the GB area. The density could give the information on the relative importance of a certain atomic process.

3. Results

3.1. OKMC simulations of microstructure evolution near $\Sigma 5(3\ 1\ 0)/[0\ 0\ 1]$ under cumulative irradiation

With the fundamental interaction parameters of the SIA/V with the GB of $\Sigma 5(3\ 1\ 0)/[0\ 0\ 1]$ (as summarized in supplementary Fig. S5) in hand, OKMC simulations were firstly performed to explore defects behavior in the GB system under cumulative irradiation. The parameters L , T and τ are varied. To characterize the evolution in the microstructure driven by the defects accumulation in the system, we calculated the defects concentration and distribution near the GB and at the GB, as well as their variation with radiation dose. For the L of 10 nm, results are mainly presented in Fig. 2, while results for other cases are shown in supplementary Figs. S7 and S8. We found that defects accumulation behavior depends on the parameter regimes of L - T - τ space, as illustrated in Fig. 2(j) for the defects concentration level in different parameters regimes. Apparently, in most of cases the SIA concentration in the bulk (C_{SIA}^{bulk}) is lower than the bulk V concentration (C_V^{bulk}); it is in agreement with the atomic calculation predicting the preferential segregation of the SIA to the GB over the V []. Particularly, in a system with a small L , e.g. 10 nm, the extremely small value of C_{SIA}^{bulk} was observed, indicating that no SIAs survive in the bulk under such condition. It may be due to the too small value of L for the SIA to aggregate to large stable SIA_ns. Such phenomenon weakly depends on T and τ possibly because of the very low diffusion energy barrier of the SIA near the GB.

In contrast, T and τ significantly affects V accumulation near the GB. At a high T and/or low τ , the system has a low C_V^{bulk} . Especially, as L is smaller than 100 nm, T is higher than a certain level e.g. 300 K and τ is lower than a level e.g. 10^{-5} dpa·s⁻¹, there is nearly no V surviving near the GB, as suggested by the quite low level of C_V^{bulk} . This is in agreement with the expectation that the GB system with a small L should well self-heal the radiation damage subjected to under a certain kinetic condition. It could be attributed to the enhanced diffusion/annihilation of the V [] and reduced formation probability of immobile V_n near the GB in the corresponding parameter regime. It also implies that the radiation resistance of NC Fe in the regime could be explained based on the fundamental SIA/V segregation and annihilation processes included in the OKMC model (Fig. 1(b)).

Besides these observations consistent with our intuition, we however also observed exceptional results. In a certain regime of the L - T - τ e.g. a low T and high τ , C_V^{bulk} increases with radiation dose, even if when L is as small as 10 nm (Fig. 2(a-c)); it implies that the V accumulates in the bulk with radiation in the considered parameter regime. Meanwhile, SIAs accumulate at the GB, as indicated by the increase in C_{SIA}^{GB} with dose (Fig. 2(e-g)). Besides, further examination of the defect distribution near the GB (Fig. 2(k-n) and supplementary Fig. S8) suggests that after a certain dose, the C_V^{bulk} reaches a peak in the bulk region quite near the region with a very low C_V^{bulk} in the vicinity of the GB; C_V^{bulk} also decreases with the increase in the V distance to the GB due to the periodical property of the OKMC model. These results suggest that the OKMC model containing annihilation and segregation processes of the SIA/V predicts the accumulation of radiation damage in the bulk region near the GB and at the GB, which seems to contract the self-healing property of the small-sized GB system with low-energy barriers for the V/SIA diffusion and annihilation nearby []. Then, we are naturally faced with the following issues: whether both C_V^{bulk} and C_{SIA}^{GB} would continue to increase as radiation proceeds and how the accumulated defects modify the GB structure and consequently affect the SIA/V behavior near the damaged GB (Fig. 2(k-n)). If the trend of C_V^{bulk} and C_{SIA}^{GB} fails to increase after a critical dose, it requires the clarification of new atomic processes or mechanisms occurring, which have to

be incorporated into the OKMC model to correctly predict the radiation damage accumulation in NC Fe together with the ones in Fig. 1(b).

3.2. MD simulations of the structural relaxation of the GB $\Sigma 5(3\ 1\ 0)/[0\ 0\ 1]$ with accumulated defects

To answer the questions raised above, we sampled the OKMC-calculated $C_{SIA/V}^{bulk} / C_{SIA/V}^{GB}$ -dose curve (Fig. 4(a–d)) and revisited to the defects accumulation and structural relaxation mechanisms near the GB on the atomic scale by using MD. We concentrated on the regime of the L - T - τ parameter space where the radiation damage could not be well healed as predicted by initial OKMC simulation results (Fig. 2). Although the OKMC simulations reveal that Vs accumulate near the GB and SIAs aggregate at the GB, firstly only SIAs were contained in the atomic models at the GB to explore how the GB relaxes after it absorbs defects. To do this, a certain number of SIAs were loaded into the GB by using the method as described in section 2.2.3; the relation of the C_{SIA}^{GB} to radiation dose and L - T - τ could be obtained by referring to AI in Fig. 2(e). The GB with SIAs was relaxed sequentially at 0 and 300 K. The E_{GB} was then calculated. By analyzing the change in E_{GB} and the corresponding GB structural variation process, we revealed the GB structural response to cumulative irradiation.

Figure 3(a) shows the E_{GB} profile as a function of C_{SIA}^{GB} . The profile could be divided into three stages with different features of the E_{GB} changes with C_{SIA}^{GB} . From C_0 to about C_c , the E_{GB} nearly increases linearly with C_{SIA}^{GB} , as reported in Ref. [] for one Fe GB of $\Sigma 17(5\ 3\ 0)/[0\ 0\ 1]$. Such tendency could be derived from the definitions of the E_{GB} , E_f^{SIA} and $E_b^{SIA-SIA}$ (supplementary text S1). For the isolated SIAs at the GB in the case of a low C_{SIA}^{GB} produced by a low dose irradiation, the slope of the curve only depends on the E_f^{SIA} at the GB. Yet, with more SIAs introduced into the GB, C_{SIA}^{GB} is over than the level of C_{SIA1}^{GB*} (Fig. 3(a)), the growth in E_{GB} slows down, as shown in Fig. 3(a) from C_c to C_e . During this growth stage from C_0 to C_e , a noticeable change in E_{GB} was observed. The increase in E_{GB} due to the SIA accumulation at the GB could be readily understood based on the contribution of the defect formation to E_{GB} . However, as C_{SIA}^{GB} increases to a certain level (C_{SIA2}^{GB*} in Fig. 3(a)), the E_{GB} no longer increases but exhibits a drop trend with the increasing in the C_{SIA}^{GB} .

The decrease trend holds from C_e to C_g . The different dependence of E_{GB} on the C_{SIA}^{GB} from C_d to C_g to that from C_0 to C_d was termed as the SIA overloaded effect. Of course, the overloaded SIAs at the GB would also affect the GB structural transition and the subsequent defect-GB interactions. After C_g , the E_{GB} seems to increase and decrease periodically (“Cycle1” and “Cycle2” in Fig. 3(a)), although it changes smaller than that from C_0 to C_g (“Cycle0” in Fig. 3(a)).

To reveal the GB structural evolution and corresponding relaxation mechanism during the different $E_{GB} \sim C_{SIA}^{GB}$ stages in Fig. 3(a), we examined the relaxed GB structure after each loading of the SIAs into the GB with focus on the effect of the overloaded SIAs on the GB structure. Several typical GB structures with different levels of C_{SIA}^{GB} are shown in Fig. 3(b–j). We found that, from C_0 to C_c , the GB containing a low concentration of SIAs remains its basic structure (Fig. 3(b) and (c)) as a pure one without defects (supplementary Fig. S4(b)); in other words, the structural unit along the GB is not modified by the absorbed SIAs. Meanwhile, the loaded SIAs also maintain their identity at the GB, as shown in Fig. 3(b) and (c) by the red spheres with high potential energies. The structural observation here is consistent with the linear dependence of E_{GB} on C_{SIA}^{GB} (from C_0 to C_c in Fig. 3(a)), as predicted by the supplementary text S1 on the theoretical derivation of the relation of the E_{GB} to C_{SIA}^{GB} . It also implies that, in this SIA concentration range or corresponding dose range, the OKMC modeling results (Fig. 2) are correct due to the fidelity of the important SIA-induced annihilation process incorporated into the OKMC model.

Nevertheless, from C_d to C_e , parts of the loaded SIAs were found to disappear after the GB relaxation. Particularly, the new GB structure was formed as more SIAs were introduced into the GB (Fig. 3(e)). The structure with the E_{GB} of $1.35 \text{ J}\cdot\text{m}^{-2}$ is obviously different to that for the pure GB with the E_{GB} of $0.98 \text{ J}\cdot\text{m}^{-2}$. The atom separation distance in the new GB system also exhibits unique quasi-continuous distribution compared to the discrete distribution in a pure GB (inset figure in Fig. 3(e)). In the latter section, we will show the new GB structure has its special defects properties. In some cases of MD simulations, we also observed the formation of the other new GB structures induced by the introduced SIAs (supplementary Fig.

S9(a) and (b)). Similar formation of the new GB phases induced by the defects accumulation at the GB has been reported in several face-centered cubic (fcc) GB systems []. Therefore, the interaction among excess SIAs and the new phase formation could give rise to the reduced growth rate in E_{GB} from C_d to C_e (Fig. 3(a)); the attraction between SIAs and the transition of the loaded SIAs to components of the GB release the system energy. From C_e to C_g , the GB gradually recovers to its original structure, accompanied by the migration of the local GB parts (Fig. 3(f)). More specifically, some Vs in the form of V-SIA-V complexes appear near the sites of the lost SIAs at the GB. Finally, the SIAs and Vs coexist at the GB. The recovery of the GB structure via the GB migration and V formation could thus lead to the decrease trend of the E_{GB} with C_{SIA}^{GB} from C_e to C_g in Fig. 3(a). The C_{SIA}^{GB} -dependent GB structural relaxation behavior suggests that it requires different OKMC modeling schemes before and after the critical radiation dose. For example, as $C_{SIA}^{GB*}=2.5 \text{ nm}^{-2}$ (Fig. 3(a)), we could obtain the critical dose of about 0.75 dpa for a given radiation condition of $L=10 \text{ nm}$, $T=300 \text{ K}$, and $\tau=10^{-2} \text{ dpa}\cdot\text{s}^{-1}$ (Fig. 2(g)).

Since from C_0 to C_g , the SIA accumulates at the GB, followed by the GB relaxation and recovery, the period from C_0 to C_g could be considered as a cycle, as marked by *Cycle0* in Fig. 3(a). As the GB in Fig. 3(g) containing a certain concentration of Vs and SIAs is selected as the starting structure for absorbing the subsequent SIAs, it could expect the similar behavior of the GB to that in *Cycle0*. For instance, we observed the formation of new GB phases, although it is not so frequent due to the existence of the Vs. We more frequently observed SIA-V transition during the GB relaxation and also found the enhanced GB mobility. Therefore, as the GB continuously absorbs SIAs, new atomic process occurs; the overloaded SIAs could not only affect E_{GB} variation trend but also modify the GB structure.

3.3. SIA-V transition process near $\Sigma 5(3\ 1\ 0)/[0\ 0\ 1]$

To reveal the transition process for the SIA to the V and the underlying physical reason, we analyzed the atom displacements field near the GB during the structural relaxation. Fig. 4 shows the atom displacements of the GB of $\Sigma 5(3\ 1\ 0)/[0\ 0\ 1]$ with a certain concentration of the SIA at 300 K for 50 ps

relative to the initial GB state. As the SIA was put near the GB in *Style2* (Fig. 1(h)), the atom displacement was induced by both the SIA segregation and GB relaxation. Furthermore, the atom displacement due to the formation of new GB phases (Fig. 3(e)) relative to a pure GB is also involved in the transition. The atoms that are aligned in one column near the GB in the final state are however not well aligned in the initial state, e.g. atoms in columns *C* and *D* (Fig. 4(b)). Consequently, the displacement field is complex (Fig. 4(a)). Yet, we still could observe that it lacks one atom in column *GI* in the final state, forming a V at the GB; meanwhile, in the initial state the atoms or SIAs are not fully occupied in one column (Fig. 4(c)). We speculated that the overloaded SIAs at the GB occupied one atom column after transition, forming regular atom columns but with a certain number of Vs due to the incomplete occupation of the atoms in the column.

Such picture was further validated in another simple model where SIAs were loaded into the GB via *Style1* (Fig. 1(g)); the SIAs were intentionally put at the SIA site at the GB to avoid the coupling of the displacement fields of the SIA segregation and that for the SIA-V transition. After comparing the GB position before and after relaxation, we found that the GB migrated to the nearest state (Fig. 4(d)). Besides, the displacement fields near the GB core are significantly different from that far from the GB. Some regular displacement patterns correspond to the intrinsic motion of the atoms during the GB migration, while others were induced by the transition from the SIA to V. Fig. 4(e) shows the corresponding atoms in the initial and final states. The above transition picture was confirmed, as illustrated in Fig. 4(f). The SIA_i in a GB structure unit was initially aligned along the tilt axis. The number of defects locations along the tilt axis in a computational cell is N . As the number of SIAs i approaches to N , the GB structure was transformed to the structure with a V_j ($j=N-i$) after tens of ps at 300 K. Meanwhile, the j atoms on the opposite GB side move to the GB plane and become the SIA_j , leaving a V_j behind. The structure of a V_j - SIA_j - V_j forms (the MS calculation suggests that the energy of the GB with a V-SIA-V complex is about 0.1 eV lower than that for the GB with a V). As for the transition from a new GB phase (Fig. 3(e)), it could be considered as transition of the atoms in Fig. 4(d) and (e) with extra displacements related to the new GB phase.

The energetic driving force for the SIA-V transition was then analyzed. In supplementary text S1, we have derived the relation of the GB energy variation (ΔE_{GB}) to the defects formation energy ($E_{SIA/Vf}^{GB}$) and the defects concentration (C) at the GB approximately as $\Delta E_{GB} = E_{SIA/Vf}^{GB} \times C$. Therefore, the two factors of $E_{SIA/Vf}^{GB}$ and C influence ΔE_{GB} and further affect the transition process. As shown in supplementary Fig. S5, E_{SIAf}^{GB} is lower than E_{Vf}^{GB} , implying that it is energetically unfavorable for the SIA to transit to the V. Only when the excess SIAs are transited to the minority of Vs could ΔE_{GB} be greatly reduced during the transition.

3.4. Evolution in the GB's role for Vs under cumulative damage

OKMC simulations in Fig. 2 and supplementary Figs. S7 and S8 suggest that at a specific radiation condition the V mainly survives near the GB. Meanwhile, Figs. 3 and 4 show the variation in E_{GB} and GB structural evolution during the cumulative irradiation. Thus, it is of meaning to explore the corresponding variation of the GB's role as a sink for the V during the cumulative radiation. Previously [], it has revealed that the GB mainly has two kinds of roles for the V either as the trapping center for the V or as the catalyst for the V-SIA annihilation, closely related to the sign and magnitude of E_V^f . To reveal the evolution in the GB's role for Vs under accumulated radiation damage, we calculated the E_V^f near the GB with different concentration of SIAs as well as the cumulative distribution function of the E_V^f ($C(E_V^f)$). As shown in Fig. 5(a), the GBs with several levels of C_{SIA}^{GB} (atomic structures in Fig. 3(b-j)) have characteristic $C(E_V^f)$. Depending on the level of the C_{SIA}^{GB} , the $C(E_V^f)$ for these GBs could be divided into three categories. The pure GB (supplementary Fig. S4(b)) only has E_V^f distribution in the regime of the large positive E_V^f ($[E_V^f, E_{Vf}^{bulk}]$). The GB in Fig. 3(e) has a quasi-continuous distribution of the E_V^f , starting from zero point to the E_{Vf}^{bulk} ($[0, E_{Vf}^{bulk}]$). The GBs with the other levels of the C_{SIA}^{GB} have similar $C(E_V^f)$, featured by the high contribution of large negative E_V^f . Actually, the different features of the $C(E_V^f)$ suggest the changes brought about by the accumulated SIAs at the GB related to the V-GB interaction in terms of the V-GB interaction nature and binding strength. Specifically, the sign of the E_V^f is positive for the V near a pure GB, and then the sign becomes negative as for the GB loaded with a certain number of SIAs. However, above a critical value of

the C_{SIA}^{GB} , the sign for most of sites is positive again. We also found that the V-GB binding strength is greatly enhanced, as manifested by the occurrence of small but positive E_V^f on $C(E_V^f)$. This could arise from the enhanced effect in the new GB phase with a high atomic density and the binding of the V to the V transited from the SIA. The variation in the V-GB binding energy will affect the basic behavior of the V near the GB. Therefore, as the C_{SIA}^{GB} varies, the V-GB interaction nature would be modified; meanwhile, the GB's role for the V may dynamically change.

To better characterize evolution of the V-GB interaction, we further categorize the sites near the GB with different C_{SIA}^{GB} of SIAs based on the feature of the $C(E_V^f)$. Considering the physical meaning of E_V^f , the $C(E_V^f)$ was further divided into three groups (*Reg1*, *Reg2*, and *Reg3* in Fig. 5). The Vs in each regime has a E_V^f within a certain range, which was considered as an general energy level for the V. In *Reg1*, the V has clear energy levels of large positive value and small displacement after relaxation of the GB with the V (Fig. 5(b)). It implies that after the bulk V enters *Reg1*, the system energy reduces but the V remains locally at the site. Therefore, the region could be considered as a trapping region for the bulk V. In *Reg3*, the V also has a large magnitude of E_V^f , but the value is negative; the atom has a large displacement after relaxation of the system with a V in the region (Fig. 5(b)). We have shown that it forms the spontaneous annihilation region near the trapped SIAs with such E_V^f feature []. And thus, *Reg3* could be defined as the recombination region. We also found additional feature of E_V^f that has a very small value close to zero in *Reg2*, e.g. the results for the C_{SIA}^{GB} of C_e in Fig. 5(a). It may be related to the locally disordered structure (Fig. 3(e)).

To further qualitatively describe the probabilistic V-GB interaction and its evolution with the C_{SIA}^{GB} , we further introduced the concept of the density of the V energy level (characterized by E_V^f) in the three regimes. Combining the physical meaning of each regimes and the density variation with the C_{SIA}^{GB} , we could obtain the evolution information of the GB's role for the V. Fig. 5(c)) presents the calculated density ($C_{Reg1,Reg2,Reg3}$) for each GB system loaded with different C_{SIA}^{GB} of SIAs. As can be seen from Fig. 5(c), $C_{Reg1,Reg2,Reg3}$ varies remarkably with C_{SIA}^{GB} , suggesting that $C_{Reg1,Reg2,Reg3}$ is more sensitive than E_{GB} (Fig. 3(a)) to the microstructure and

may serve as a more effect method for characterizing the GB structural evolution during irradiation. However, the accumulated SIAs at the GB have totally different effects on C_{Reg1} and C_{Reg3} given their individual trends (Fig. 5(c)). Specifically, from I to PI , C_{Reg3} increases with C_{SIA}^{GB} , implying a more important role of the GB in annihilating the V nearby as more SIAs accumulate at the GB due to the more contribution of the atomic processes related to annihilation e.g. IE to alleviate the Vs near the GB with the SIAs aggregated at the GB. Such enhanced effect of the GB's role in annihilating defects could be readily understood based on the natural extension of the annihilation region near the multiple SIAs compared with the single SIA. Meanwhile, the reverse trend for C_{Reg1} with C_{SIA}^{GB} was observed within the same C_{SIA}^{GB} range, e.g. from $I0$ to SI within the first Cycle of $Cycle0$. It indicates that the GB's role as a trapping center for the V becomes weakened. Exactly, parts of the trapping sites for the V near a pure GB were changed to the annihilation sites near the GB with a low concentration of SIAs (Fig. 3(a–c)). The reason could be the instability of more sites near the GB induced by the more SIAs at the GB. Note that, for a smaller E_b (as described in the caption of Fig. 5), C_{Reg1} would increase with C_{SIA}^{GB} , suggesting that the SIAs at the GB only slightly affect the stability of the sites with positive E_V^f . From PI to BI , C_{Reg3} reduces greatly with C_{SIA}^{GB} , indicating the weak role of the GB in annihilating the V nearby. This is consistent with the structural observation in Fig. 3(b–e) that at BI corresponding to the C_{SIA}^{GB} of C_e the loaded SIAs become components of the new GB phase. After SI , C_{Reg1} increases greatly and reaches its peak value at TI , while C_{Reg3} has a quite small value. It suggests that near the new GB phase, the V interacts with the GB mainly via the trapping process. The extended strain field near the GB (Fig. 3(e)) by the large atom density could account for the enhanced trapping for the V. The similar trends of C_{Reg1} and C_{Reg3} were observed from TI to $S2$ or from BI to $P2$ to that from I to PI . The structural reason for the trends is also similar. In the two cases, the accumulated SIAs at the GB induced the transition of the trapping site to the annihilation sites due to the lost identity of the SIAs at the GB. Only the initial GBs at $I0$ (supplementary Fig. S4(b)) and TI (Fig. 3(e)) have different phases. The special structural reason during this concentration range includes the recovery of the GB from TI to $S2$. Therefore, within the

first cycle of *Cycle0*, we revealed an alternating evolution of the GB's role of trapping and annihilation of Vs compared to the previously known unique role of the GB either as a trapping center for the V or as the annihilation catalyst []. Furthermore, the alternating pattern or mechanism leads to the different dominated roles that the trapping and annihilation play in the V-GB interaction within different C_{SIA}^{GB} ranges or equivalently under different radiation conditions. For instance, by comparing the magnitude of C_{Reg1} and C_{Reg3} , we found that the trapping plays a dominated role in removing the V near the GB from *I0* to *J0*, while from *J0* to *P1* the annihilation dominates. The present results suggest that, the previous reported self-healing mechanisms for radiation damage in NCs based on the SIA behavior near the GB (e.g. the annihilation induced by the *IE* []) and the coupling of the V migration towards the GB with the SIA moving along the GB) may fail under extreme irradiation conditions due to either the new phase formation of the GB or the GB structural recovery.

After *Cg*, although no fine features were observed on $C_{Reg1,Reg2,Reg3}$ compared with that within *Cycle0*, some similar trends were still noticed. The C_{Reg1} for a GB with a certain concentration of SIAs is much higher than C_{Reg3} and also than C_{Reg1} for a pure GB without SIAs, indicating that the trapping is a more basic process than annihilation in the GB system exposed to continuous irradiation. It could arise from the formation of the V after GB structural transition (e.g. Fig. 3(g)). Basically, C_{Reg1} and C_{Reg3} show a reverse trend with C_{SIA}^{GB} . Exception was encountered during a certain C_{SIA}^{GB} range (e.g. from about 17 to 21 nm⁻²) where C_{Reg1} and C_{Reg3} increase simultaneously due to the formation of the V. Finally, some special features were observed on the curve of the C_{Reg2} with C_{SIA}^{GB} , which reflects the structural meaning of C_{Reg2} and its connection to GB structures. For example, C_{Reg2} reaches a peak at U1 in Fig. 5(c) where the new GB phase also forms (Fig. 3(e)). Besides, C_{Reg2} has a larger value within *Cycle1* and *Cycle2* where the GB consists of V-SIA complexes and is not so regular compared to a pure GB.

3.5. Evolution in the kinetic property of Vs under accumulated damage

We next examined the V kinetics near several typical GB structures as observed in Fig. 3(b–j), including

a pure one (Fig. 6(a)), the GB with multiple SIAs with well-defined identity (Fig. 6(b)), the GB with a new phase (Fig. 6(c)), and the GB after recovery (Fig. 6(d)). We calculated the V migration energy barriers along one typical paths near these GBs by using the NEB method (section 2.2.1) []. As seen in Fig. 6(e), all the profiles show a decreasing trend with the V closing to the GB, implying the enhanced kinetics of the V near the GBs. The difference is also significant. Comparing the results for the GB in Fig. 6(a) and Fig. 6(b), we found that the V is finally trapped at the GB along the diffusion and trapping path of *path1*, while along *path2* the V would be annihilated at site *E2* within the annihilation region *Reg3*. Furthermore, the energy barriers along *path2* are smaller than that along *path1*, indicating that SIAs at the GB promotes the V diffusion and annihilation near the GB via reducing the energy barriers. These results are consistent with previous results []. Comparing the results along *path1* and *path3*, we found that the energy barriers for the V diffusion along *path3* are also smaller than that along *path1*, implying that the kinetics for the V near the new GB phase is further enhanced than that near a pure GB. Since both sites *G1* and *F3* locate within *Reg1*, *path1* and *path3* are diffusion-trapping paths for the V. We also found the promoted diffusion of the V along *path4* near a GB containing the V after recovery compared to that along *path1*. Therefore, no matter how the GB relaxes after trapping a concentration of SIAs from the bulk region nearby, the diffusion of the V near these GBs is always accelerated due to three factors of the accumulation of a specific concentration of SIAs, or the new phase formation of the GB or V formation after the GB structural recovery.

These enhanced processes for the V predicted by the above MS calculations of the V kinetics near the GBs were validated by MD simulations of the V behavior near the three typical GB structures at 300 K (Fig. 6(f–h)). A certain concentration of Vs were initially put near the GB. We found that after 50 ps at 300 K, the Vs near the pure GB remain immobile (Fig. 6(f)), while the Vs near the new GB phase were trapped by the GB (Fig. 6(g)). The Vs closer to the GB after the GB's recovery also segregated to the GB (Fig. 6(h)). Therefore, it becomes easier for the Vs near the GB to enter the GB with a new phase or containing Vs after recovery.

3.6. Defects accumulation and structural relaxation mechanisms in the other GBs

The above OKMC, MS and MD results (Figs. 1–6) are obtained in the GB of $\Sigma 5(3\ 1\ 0)/[0\ 0\ 1]$. To show whether the defects accumulation features and GB structural relaxation mechanisms apply to the other GBs, we also performed extended similar simulations in several other GBs (the relaxed pristine structures of these GBs are given in supplementary Fig. S4). We compared the atomic and coarse-grained defects behavior in these GBs. We found that both the V and SIA distributes within several layers near the GB (supplementary Fig. S6). The V locates at the stable site of the GB as a point (Fig. S6). However, the SIA configurations are complex (supplementary Fig. S6). In addition to the point configuration at the GBs of $\Sigma 5(2\ 1\ 0)/[0\ 0\ 1]$, $\Sigma 13(5\ 1\ 0)/[0\ 0\ 1]$, $\Sigma 13(3\ 2\ 0)/[0\ 0\ 1]$, $\Sigma 85(13\ 1\ 0)/[0\ 0\ 1]$, $\Sigma 3(1\ 1\ 1)/[1\ 1\ 0]$, $\Sigma 9(2\ 2\ 1)/[1\ 1\ 0]$, other configurations were also found, including the dumbbell at the GBs of $\Sigma 25(4\ 3\ 0)/[0\ 0\ 1]$, $\Sigma 85(7\ 6\ 0)/[0\ 0\ 1]$, $\Sigma 9(1\ 1\ 4)/[1\ 1\ 0]$, $\Sigma 11(1\ 1\ 3)/[1\ 1\ 0]$, $\Sigma 11(3\ 3\ 2)/[1\ 1\ 0]$ and the crowdion at the GB of $\Sigma 3(1\ 1\ 2)/[1\ 1\ 0]$. The different SIA configurations at the GB may be related to the atom density near the GB core. For example, the twin boundary of $\Sigma 3(1\ 1\ 2)/[1\ 1\ 0]$ with the SIA of a crowdion has the largest atom density near the GB core.

The OKMC parameters also depend on the GB structures (supplementary Tables S3, S4, and S6–S8). Based on the MS parameters, particularly the emission energy barrier for the V/SIA from the GB (E_a^{VE}/E_a^{IE}) and the corresponding time (t_{VE}/t_{IE}), prejudge the V/SIA behavior near the GB. We found that the twin boundary has the lowest $E_a^{VE/IE}$. Consequently, only at the twin boundary is $t_{VE/IE}$ on the order of one hour at room temperature, while in the other GBs $t_{VE/IE}$ is far larger than one hour, particularly for the SIA). Thus, the V/SIA could be reemitted from the twin GB once segregated to the GB at an elevated temperature. The further OKMC simulations of a single SIA/V behavior suggest that at 300 K, the SIA near all the GBs first randomly walks in the bulk region and finally gets trapped at the GB; it is tightly bound at the GB after trapping (supplementary Fig. S10(a)). Yet, the V was observed to be occasionally reemitted from the twin GB at 300 K after segregation to the GB (supplementary Fig. S10(b)). As the T increases to 400 K, both the

SIA and V were frequently remitted from the GB (supplementary Fig. S10(c) and (d)), particularly for the V (supplementary Fig. S10(d)). It could expect that the difference in the defect accumulation rates in the two GBs is not significant at a low T . The emission in the twin boundary enhances bulk V accumulation rate and decreases the healing efficiency for radiation damage in the bulk region by the GB at the parameter regime of a high T and a low τ . Therefore, in the parameter regime we are interested in e.g. low T and high τ , the reemission of the SIA/V from the GB may not affect the SIA/V accumulation and GB relaxation mechanism significantly; of course, the critical dose for the new GB relaxation mechanism to occur (point A on the curve of $C_{SIA,V} \sim dose$ in Fig. 1(b)) would be modified once the reemission was activated.

We next mainly explored the curve of $E_{GB} \sim C_{SIA,V}$ in the other GBs by performing similar relaxation simulations to that in $\Sigma 5(3\ 1\ 0)/[0\ 0\ 1]$. Yet, MD simulations at 300 K suggest that different GBs have distinct intrinsic mobility, as measured by the GB migration distance within a time interval (supplementary Fig. S11). Some of the GBs remain immobile at room temperature, e.g., the GBs of $\Sigma 5(2\ 1\ 0)/[0\ 0\ 1]$ and $\Sigma 5(3\ 1\ 0)/[0\ 0\ 1]$. However, the GBs of $\Sigma 25(4\ 3\ 0)/[0\ 0\ 1]$, $\Sigma 85(7\ 6\ 0)/[0\ 0\ 1]$, $\Sigma 85(13\ 1\ 0)/[0\ 0\ 1]$, $\Sigma 3(1\ 1\ 1)/[1\ 1\ 0]$, $\Sigma 9(2\ 2\ 1)/[1\ 1\ 0]$ and $\Sigma 11(3\ 3\ 2)/[1\ 1\ 0]$ were observed to move and even disappeared via interacting with the free surface in the GB system. We thus only present results for the GB that did not disappear after MD simulations of the GB relaxation for 50 ps. Figure 7(a–i) presents the E_{GB} profiles as a function of C_{SIA}^{GB} in these relatively stable GBs. First, it was noticed that the magnitude of ΔE_{GB} varies greatly in different GBs. Since E_{GB} measures the thermodynamic stability of a GB, it implies different effects of the SIAs at the GB on the GB's stability, depending on the GB structure. As seen in Fig. 7(j), the maximal ΔE_{GB} basically increases with E_{SIAf}^{GB} linearly. As a result, the loading of the SIA to the GB with a lower SIA stability (a large E_{SIAf}^{GB}) would cause the GB to be more easily instable. Figure 7(j) also suggests that ΔE_{GB} exhibits an approximately negative relation to the E_{GB0} . Given the meaning of E_{GB0} as the indicator for the intrinsic thermodynamic stability of a pure GB and the ΔE_{GB} as an indicator for the radiation-stability of the GB, such relation may reveal the contradiction of the two types of stabilities. To maintain a relative stability of a GB

under radiation, a specific intrinsic stability of the GB is required.

We also found that the profiles in $\Sigma 5(2\ 1\ 0)/[0\ 0\ 1]$ (Fig. 7(a)), $\Sigma 3(1\ 1\ 2)/[1\ 1\ 0]$ (Fig. 7(e)) and $\Sigma 11(3\ 3\ 2)/[1\ 1\ 0]$ (Fig. 7(i)) exhibit a obviously periodical trend similar to that in $\Sigma 5(3\ 1\ 0)/[0\ 0\ 1]$ (Fig. 3(a)) (labeled as *Type 1* in Fig. 7). However, for the other GBs a different trend was observed, where the E_{GB} firstly increases and then basically becomes constant (Fig. 7(b–d) and (f–h) labeled as *Type 2*). Given the SIA-V transition during the GB structural relaxation, the two different types of the GB energy response to the accumulated SIAs at the GB could be related to the distinct SIA/V energetic properties at the GB. As shown in Fig. 7(j), the GBs of *Type 1* were found to have a large absolute difference between C_{SIA}^{GB} and C_V^{GB} ($|E_{SIA}^{GB} - E_V^{GB}|$), while the $|E_{SIA}^{GB} - E_V^{GB}|$ is small in the GBs of *Type 2*. This could be readily understood, since a small value of $|E_{SIA}^{GB} - E_V^{GB}|$ implies that the slight variation in the GB energy would be induced after the transition of the SIA to V at the GB.

Based on the structural response of the GB to irradiation, the GBs were further divided into two categories of Type I and Type II. The GBs of *Type 1* and some of GBs of *Type 2* belong to *Type I*. These GBs have similar defects accumulation and structural relaxation behavior to that in $\Sigma 5(3\ 1\ 0)/[0\ 0\ 1]$. The loaded SIAs also become components of the GB and new ordered GB structures form (Fig. 7(a1–e1) and (i1)). As the concentration of the SIA at the GB increases to a certain level, the GB migrates locally, accompanied by the transition of the SIA to V. These GBs were found to have high SIA/V formation energy at the GB ($E_{SIA/V}^{GB}$) (Fig. 7(k)). The others belonging to *Type II* exhibit the unique response to the V/SIA accumulation at the GBs (Fig. 7(f1–h1)). We frequently observed the formation of the disordered GB structures during the loading of the SIAs to the GBs, which could arise from the low thermal stability of the GBs as suggested by the small $E_{SIA/V}^{GB}$ in these GBs (Fig. 7(k)). These GBs have a quasi-continuous distribution of the E_V^f after absorbing a certain concentration of SIAs, as shown in supplementary Fig. S13 for the case of $\Sigma 9(1\ 1\ 4)/[1\ 1\ 0]$.

Figure 7(a2–i2) further presents the evolution of $C_{Reg1,Reg2,Reg3}$ with C_{SIA}^{GB} in the two types of GBs. For the GBs

of *Type I*, the similar profiles were observed to that for $\Sigma 5(3\ 1\ 0)/[0\ 0\ 1]$, including the alternating variation in the C_{Reg1} and C_{Reg3} . It indicates the mutual transition of the GB's role of the trapping and annihilation for the V during the SIA loading to the GB. However, for the twin boundary of $\Sigma 3(1\ 1\ 2)/[1\ 1\ 0]$, we frequently observed the simultaneous increase of the C_{Reg1} and C_{Reg3} . This is due to the very small segregation energy of the V at the pure GB (0.18 eV in supplementary Table S8). Consequently, C_{Reg1} increases from zero point. Therefore, an additional picture about defects accumulation and GB structural relaxation works in the twin boundary via the synergistically enhanced trapping and annihilation of the V. For the GBs of *Type II*, C_{Reg1} is much larger than C_{Reg2} and C_{Reg3} , indicating that the trapping is a main process for the GB absorbing the V nearby. It can also be seen that C_{Reg2} is close to C_{Reg3} ; besides, both C_{Reg2} and C_{Reg3} do not change apparently with C_{SIA}^{GB} , compared to that in the GBs of *Type I*. Such variation feature well corresponds to the disordered GB structure of *Type I*. The level of C_{Reg3} may be related to the E_{SIAf}^{GB} in the GBs (supplementary Fig. S12). The small E_{SIAf}^{GB} in the GBs of *Type II* leads to the small level of C_{Reg3} , in agreement with the GB classification based on $E_{SIA/Vf}^{GB}$ (Fig. 7(k)).

3.7. OKMC remodeling of defects accumulation and structural relaxation near the GB

By performing MD simulations of the GB structure predicted by the OKMC simulation and the V-GB interaction, we have revealed the new processes of the GB relaxation and its interaction with the V. Considering these new atomic processes, we remodeled the defects accumulation and structural relaxation near the GB by using the OKMC method. The main features captured into the new OKMC model include the disappearing of the SIAs at the GB after a critical C_{SIA}^{GB} and the simultaneous GB migration as observed in the GBs of *Type I*. The effect of the formation of the new GB phase on the V nearby is similarly reflected by the transition of the annihilation region to the trapping region. As for the GB of *Type II*, it does not involve the SIA-V transition, while the trapping for the V always works (Fig. 7(f2–h2)). In the remodeling of the defects behavior, we mainly considered the GB of *Type I*. Since the GB only directly interacts with the V near itself, we thus defined the V concentration near the GB (C_V^{nearGB}). By examining its variation combined

with the snapshots of the defects microstructure, we explored the evolution of the V-GB interaction mechanisms with radiation dose.

Figure 8 presents the OKMC simulation results of the variation in C_{SIA}^{GB} and the corresponding C_V^{nearGB} with radiation dose at several values of T and τ (see supplementary Fig. S14 for the results of $T=300$ K and τ of 10^{-5} dpa·s $^{-1}$). As seen from Fig. 8(a–c), different to the old OKMC model prediction of C_{SIA}^{GB} to increase continuously with radiation dose (Fig. 2(e–g)), the new OKMC model predicts that C_{SIA}^{GB} no longer increases after a critical dose at the most considered radiation conditions (Fig. 8(a–c)) except at the condition of T of 300 K and τ of 10^{-5} dpa·s $^{-1}$ where both the C_{SIA}^{GB} and C_V^{nearGB} remain at a low level (blue curves in Fig. 8(c)). This is consistent with the MD simulation results and the preset picture in the OKMC model. Noticeable feature was also observed on C_V^{nearGB} . At T of 100 K and τ of 10^2 dpa·s $^{-1}$, it was found that C_V^{nearGB} firstly increases and then decreases from 0 to about 0.1 dpa (if there is no SIA-V transition process, C_V^{nearGB} would always decline due to the annihilation of the V with the sufficient amount of SIAs collected at the GB). During this period (as illustrated in Fig. 8(a) by P), the SIAs gradually accumulate at the GB (Fig. 8(d) and (e)), and finally a region free of Vs but with a high concentration of SIAs at the GB was formed (Fig. 8(e)). The period well corresponds to the trapping-annihilation transition stage (from $I0$ to $P1$ in Fig. 5(c)). Since 100 K is too low to activate the trapping, the annihilation plays a more and more important role in removing the V near the GB as more SIAs are stored at the GB. Such increase-decrease trend in C_V^{nearGB} was repeatedly observed as radiation continues; similar pattern in the microstructure also occurred repeatedly (Fig. 8(d), (e) and (f), (g)). Besides, the peak value of C_V^{nearGB} becomes large in the following several periods. In addition, there is no such V accumulation stage at relative high T of 200 and 300 K (Fig. 8(b) and (c)), which could be attributed to the effective absorption and annihilation of the V by the GB due to GB-enhanced diffusion and annihilation of the V nearby. Furthermore, after the critical C_{SIA}^{GB} , C_V^{nearGB} immediately reaches a peak value. Examining the microstructure, we found that these features could arise from the V accumulation in the bulk region near the GB (Fig. 8(e) and (g)) and the formation of V clusters (Fig. 8(h–k)). Consequently, after the SIA transition

and the simultaneous GB migration, more Vs enter the GB interacting region.

4. Discussion

4.1. The pattern for the defects accumulation and GB structural relaxation under continuous radiation

As mentioned in the introduction, the real radiation conditions (T , τ , rd , L) are complex and span a large parameter range over which radiation damage could accumulate or be healed through distinct mechanisms. We summarized the main parameters in irradiation experiments on typical Fe and W systems (supplementary Table S1), given the importance of the two systems in the nuclear engineering application. Fig. 9(a') shows the experimental parameters distribution in the T - τ space. In the parameter regime of a small L in NCs, a high T and a low τ (Regime A in Fig. 9(a')), OKMC simulations (Fig. 2, supplementary Figs. S7 and S8) have shown that radiation damage could not accumulate in the system. The self-healing property for radiation damage in the parameter regime could be accounted for by the basic segregation and annihilation processes promoted by the GB, e.g. V-hop and IE [] (of course, IE has also been shown to work at a T [] in Regimes $B1$ and $B2$).

In the other regimes of low T and/or high τ) of the authors' interest (Regimes $B1$, $B2$ and $B3$), the present study however reveals an alternative pattern or mechanism for the defects accumulation and GB structural under continuous radiation, involving the cooperative relaxation of the defects and GB. As illustrated in Fig. 9(a-j), the defect-GB interaction evolves with the distribution of the defects or radiation dose (Fig. 2) in terms of the change of the energetic and kinetic properties of the V near the GB and at the GB, and also the modification of the GB structure, energetics, and the kinetics by the segregated defects at the GB (Figs. 3–7, supplementary Figs. S4–S6, S9, S10, S12). Prior to irradiation, a pure GB could serve as a sink for the SIA and V due to the well-known energetic and kinetic reasons (supplementary Figs. S5 and S6, []), as shown in Fig. 9(a) for the trapping region for the V near the GB. After the SIA escaping the annihilation with a bulk V and segregation at the GB, the annihilation region forms around the SIA [] (Fig.

9(b)); the V near the region could be recombined via previously reported IE at a low energy barrier (process ① in Fig. 9(b)) []. Due to the preferential absorption of the SIA over the V, there is a net increase in the SIA concentration at the GB (Fig. 9(c)), while the V in the bulk region far away from the annihilation region accumulate in the grain interior (Fig. 2(k–n), Fig. 8(d–k)).

Above a critical SIA concentration, the SIAs at the GB lost their identity accompanying the formation of a new GB phase forms (Fig. 9(d)). Near the new GB structure, the V diffusion is further accelerated compared to that near a pure GB in Fig. 9(a) (Fig. 6), leading to the trapping of the V by the GB via a low energy barrier process ② (Fig. 9(d)). With the relaxation of the defects near the GB and the SIAs at the GB, the V in the bulk region far away from the GB meanwhile gets clustered (Fig. 9(d)) or assemble in the neighboring hood of the GB. From Fig. 9(a) to (d), the GB energy increases with the SIA accumulation at the GB (Fig. 9(i)). During the period, the functional region for the V near the GB evolves from the trapping region for the GB (*Regime1* in Fig. 9(j)) to the annihilation region (*Regime3* in Fig. 9(j)) and finally to *Regime2* with E_V^f close to zero (Fig. 9(j)). With the SIA continuing to accumulate at the GB, the GB begins to recover to its original structure via the transition of the excess SIAs trapped at the GB to the minority of the V at the GB and the GB migration (Fig. 9(e)). The GB energy also decreases remarkably, while the functional region returns to the trapping region for the V. Consequently, the V on the one side of the GB (e.g. V3 in (Fig. 9(e))) that initially locates in the bulk enters the GB's interaction range and could be trapped by the GB. Particularly, the V near the local GB structure containing Vs could also easily segregate to the GB (Fig. 9(f)) due to the enhanced binding of the V to the GB and diffusion by the Vs at the GB (Fig. 6). The subsequently segregated SIAs could annihilate the V at the GB (process ⑤ in Fig. 9(g)). Meanwhile, the bulk V-cluster (V_n) located near the GB could also be trapped by the GB due to the GB motion (process ⑥ in Fig. 9(g)). Such cycle (*MI* in Fig. 9) repeats over radiation dose (supplementary Table S1) involving the collection of the SIAs at the GB, the formation of new GB phase, the SIA-V transition and the GB motion, and the interaction of the V/ V_n with the GB. Depending on the GB structure, the alternative response

mechanism for the GB cumulative irradiation exists ($M2$ in Fig. 9). The GB with low defect formation energy could also develop to the disordered structure with the defects accumulated within the GB.

The revealed defects accumulation and GB structural relaxation mechanisms ($M1$ and $M2$ in Fig. 9) in a model system of Fe would apply to other systems, e.g. NCs Au and W, although the exact transition kinetics may depend on the material type and GB characters. The systems of Fe and Au have similar relative defects properties, e.g. the higher mobility of the SIA compared that for the V, which induces the common phenomenon of the preferential segregation of the SIAs at the GB over the V. Despite the different levels of defects migration energy barriers in bulk Fe and W (0.63 versus 1.80 eV for V migration), only the T range of a low T is affected. For example, the T of 563 K in irradiation experiments on W [] could be considered as a low T for W. These results also motivate investigating the defects accumulation processes and interface/boundary relaxation mechanisms in nano-composites [] and oxide dispersion strengthened materials [].

4.2. Implication of the GB relaxation mechanism for designing the radiation resistance of a nano-structured metal

Reducing the grain size in NCs is a well-known option for enhancing the radiation resistance of a poly-crystal metal. Our results provide another atomic insight into radiation damage reduction in NC metals from the view of the coupling relaxation of the defects and the GB structure, and have implications for designing and optimizing radiation-resistant NCs. The present work reveals several compromise approaches to tailor radiation performance of NCs.

First, although the radiation damage near the GB could be healed via the interaction of the defects with the GB, the damage at the GB should not be neglected. Generally, it is considered that the defects segregate to the GB in NCs and then are eliminated at the GB via complex annihilation mechanisms near the GB []. The trapping of the defects by the GB alleviates the defects accumulation in the grain interior, reducing possible swelling. Yet, depending on the radiation conditions and the energetic and kinetic properties of the

defects in the grain interior, near the GB and at the GB, the SIA/V could accumulate within the GB. The SIA-V transition mechanism revealed in the present work could prevent the over-accumulation of the defects at the GB. Consequently, the GB owes a sustainable capacity for absorbing defects from the grain interior. The mechanism is related to the defects behavior within the GB and the GB relaxation mechanism, e.g. GB migration. The GB motion leads to competing effects related to the radiation performance. In addition to the trapping of the V/SIA by a static GB via the motion of the defects, a moving GB could more effectively absorb the V/SIA in the grain interior []. And consequently, the defects accumulation rate in the grain interior is lower than that near a static GB. Nevertheless, it is well known that the GB migration would lead to the grain growth. The reduction in the trapping efficiency caused by the increase in the grain size could cancel the enhanced trapping of the V/SIA by a moving GB.

Second, there should be compromise between radiation stability of the GB and the intrinsic stability of a pure GB. The present study suggests that the GB stability is reduced as radiation defects accumulate at the GB. Furthermore, the magnitude of the increase in the GB energy is basically inversely correlated with the GB energy of a pure one.

Third, there is contradiction between the GB absorption rate for defects and the GB's thermal stability. To maintain the basic mechanical property of a GB, it is rational to select the GB that has a low V/SIA accumulation rate as the one with better radiation performance (Regime A in Fig. 9(a')). To improve the trapping efficiency of the defects by the GB, it qualitatively requires the increase in the binding energy of the defects with the GB. For example, the twin boundary binds with the V/SIA weakly compared to other GBs, and consequently the defects accumulation rate in the grain interior is larger than in other GBs at 400 K. To obtain better radiation resistance at a high T , the fraction of the twin boundary in the nano-structured system should be decreased. At a low T , e.g. 300 K, the twin boundary behaves similarly to other GBs in defects accumulation behavior. Yet, we should not overemphasize the value of the V/SIA-GB binding energy. The thermal stability and defect-GB binding strength (binding energy) are two contradictory factors.

On the one hand, at an elevated temperature, as the binding energy is higher than a certain level, the defects accumulation in the grain interior is insensitive to the binding energy. On the other hand, a large binding energy corresponds to small defect formation energy at the GB. As the defect formation energy is too low, the GB exhibits a poor thermal stability. Consequently, as defects accumulate within the GB, the disordered structure is easily formed. Such structure may serve as the nucleation point for the radiation-induced amorphization [1].

Finally, the present study may also touch the controversy over the equivalence between ion and neutron irradiation. As NC Fe is used as structural materials for next-generation fission and fusion reactors, it should be able to survive up to 200 dpa of damage at a high operating T of $\sim 550^\circ\text{C}$ [1]. Yet, the τ is as low as 10^{-6} – 10^{-7} dpa·s $^{-1}$. And thus, the relevant parameter regime may locate within Regime A (points A and B in Fig. 9(a')). However, in many accelerated irradiation testing experiments (e.g. the use of ion irradiation as a surrogate for neutron irradiation) the τ is much higher ($\sim 10^{-2}$ – 10^{-3} dpa·s $^{-1}$) than that in reality. Besides, some experiments are performed at a low T to elucidate the effect of a specific atomic process. And hence, the radiation conditions in ion radiation experiments may locate within Regimes $A1$, $A2$ and $A3$ in Fig. 9(a'). We have shown that different defect accumulation and GB structural relaxation mechanisms apply to these parameter regimes. Therefore, it may be controversial to extrapolate the results about the defect-GB interaction and microstructure evolution from high dose rate to low dose rate.

4.3. The limits in the current predictor-corrector method

Complementary to experiments, theoretical modeling/simulation plays an important role in understanding materials properties degradation and predicting their performance under irradiation. Radiation-induced microstructural evolution is an inherent multiscale process ranging from atomistic to macroscopic time-space level [1]. To model this complex process, a multiscale approach with information passing between different scales is often required. The defect energetics, kinetics, and controlling mechanisms obtained from atomistic modeling are usually used as inputs of the mesoscale methods, e.g.

KMC. However, the present study suggests that the feedback from mesoscale simulations to atomistic calculations is necessary to accurately or precisely predict the microstructure evolution under cumulative irradiation. In other words, the close coupling between the two methods in the neighboring scales is needed. This motivates the development of the *predictor-corrector* method in the current work.

The limits of the present method exist. There is obvious difference in the scale that the two methods of the atomic and coarse-grained simulation methods can access, particularly the space scale. It brings about the difficulty in dealing with the KMC-passed large clusters in atomistic simulations. This is important, since radiation to the material in real fusion/fission or ion radiation conditions produce both point defects and complex defect structures, e.g. V clusters and SIA loops. These clusters may have rather different behaviors near the GB from the point SIA/V, affecting the structural relaxation mechanism for the GB with defects clusters. In addition, the possible coupling between the cascade and the thermally-activated atomistic processes is also hard to deal with in the present simulation framework. Finally, besides for the variation in the basic energetic and kinetic properties of the defects with radiation dose, the other parameters e.g. the sink strength and its evolution with radiation dose relevant to the high level of simulating techniques are also needed.

4.4. The SIA-V transition in the locally pinned GB

Generally, NCs exhibit poor thermal stability of and coarsen significantly when heated to 0.3 to 0.5 of their melting temperature []. To stabilize NCs, nano-precipitates are often introduced at GBs to reduce the GB mobility and hence slow the rate of grain growth []. By pinning several atoms near the GB of $\Sigma 5(3\ 1\ 0)/[0\ 0\ 01]$, we modeled the drag of the GB by the nano-precipitates and explored whether the observed SIA-V transition phenomenon occurs in a stabilized NC. We found that the curves of the GB energy as a function of C_{SIA}^{GB} for a locally pinned GB (supplementary Fig. S15(a)) exhibit similar trend to that for a freely-migrating GB (Fig. 3(a)). The GB energy is only slightly higher as some atoms are pinned due to the inadequate relaxation of these pinned atoms. We further examined the GB structure and atom displacements

fields after relaxation (supplementary Fig. S15(b–f)). As one atom on the GB plane (atom *A* in supplementary Fig. S15(d)) was pinned, the transition occurred with the grain on one side of the GB migrating to the neighboring low energy state. As one atom on one side of the GB (atom *B* in supplementary Fig. S15(e)) was also pinned, the grain on the other GB side migrated during the SIA-V transition. Nevertheless, as more atoms (atoms *A*, *B* and *C* in supplementary Fig. S15(f)) were pinned, the atoms surrounding the pinned atoms also nearly remain immobile, while the GB parts far away from the pinned region migrated during the relaxation. The SIA near the pinned atoms did not transit to the V (supplementary Fig. S15(c)), but the other SIAs transited to the Vs or V-SIA-V complexes (supplementary Fig. S15(c)). Therefore, we conclude that the SIA-V transition would occur within the GB containing the nano-precipitates.

5. Conclusions

In this study, we developed the *predictor-corrector* simulation method and preliminarily realized the close coupling between the atomistic and coarse-grained modeling techniques. Using the method, we investigated the defects accumulation and GB structural relaxation mechanisms in NC Fe under successive irradiation. We revealed the radiation-parameter dependent picture for the defect-GB interactions. Within the parameter regime of a high temperature and or low dose rate, defects are well annihilated within the GB, rendering the GB system exhibit the self-healing property for radiation damage. The performance is explained by the GB-promoted annihilation of the V with SIA via the well-known processes of *IE* and V-hop. Nevertheless, within the parameter regime of a high dose rate and/or a low temperature, the new dynamic defect-GB interaction process were revealed involving the cooperated relaxation of the defects and GB. As radiation proceeds, the SIAs initially accumulate at the GB, and then become structural components of the GB, and finally the GB recovers to its background structure. The recovery involves the transition of a critical concentration of the SIAs to the minority of the Vs accompanied by the local GB motion. We revealed the

enhanced location and migration of the V near the GB with a new phase, containing Vs, making the V-type defects instable near the GB. By calculating the cumulative distribution function of the vacancy formation energy and the grouping of the sites into several regimes with the same physical meaning, we meanwhile revealed the alternating evolution of the GB structure and role of trapping and annihilation of Vs. We also found that some GBs with low thermal stability develop into disordered structure during irradiation. The results reveal the evolution of the distribution of the defects near the GB, the energetics and kinetics of defects, GB energy, structure and mobility with radiation dose.

Acknowledgments

This work was supported by the National Key Research and Development Program of China (Grant Nos.: 2017YFE0302400, 2018YFE0308102, 2017YFA0402800), the National Natural Science Foundation of China (Nos.:11735015, 51871207, 51671185, 51771181, and 51971212, U1832206, 11575229), and by the Center for Computation Science, Hefei Institutes of Physical Sciences.

References

- [1] I.J. Beyerlein, M.J. Demkowicz, A. Misra, B.P. Uberuaga, Defect-interface interactions. *Prog. Mater. Sci.* 74 (2015) 125–210.
- [2] S.J. Zinkle, G.S. Was, Materials challenges in nuclear energy. *Acta Mater.* 61 (2013) 735–758.
- [3] P. Lejcek, Grain boundary segregation in metals, Springer, Verlag, 2010.
- [4] Y. Mishin, M. Asta, J. Li, Atomistic modeling of interfaces and their impact on microstructure and properties. *Acta Mater.* 58 (2010) 1117–51.
- [5] I.J. Beyerlein, A. Caro, M.J. Demkowicz, N.A. Mara, A. Misra, B.P. Uberuaga, Radiation damage tolerant nanomaterials. *Mater. Today* 16 (2013) 443–449.
- [6] X. Zhang, et al., Radiation damage in nanostructured materials. *Prog. Mater. Sci.* 96 (2018) 217–321.
- [7] J. Knaster, A. Moeslang, T. Muroga, Materials research for fusion. *Nat. Phys.* 12 (2016) 424–434.
- [8] G.R. Odette, M.J. Alinger, B.D. Wirth, Recent developments in irradiation-resistant steels. *Annu. Rev. Mater. Res.* 38 (2008) 471–503.
- [9] W. Liu, Y. Ji, P. Tan, H. Zhang, C. He, D. Yun, C. Zhang, Z. Yang, Irradiation induced microstructure evolution in nanostructured materials: A review. *Mater.* 9 (2016) 105.
- [10] S.J. Zinkle, L.L. Snead, Designing radiation resistance in materials for fusion energy. *Annu. Rev. Mater. Res.* 44 (2014) 241–67.
- [10-1] G.S. Was, *Fundamentals of Radiation Materials Science: Metals and Alloys*, Springer, Heidelberg, 2007.
- [10-2] G. Ackland, Controlling radiation damage. *Science* 327 (2010) 1587–1588.
- [11] T. Frolov, M. Asta, Y. Mishin, Phase transformations at interfaces: observations from atomistic modeling. *Curr. Opin. Solid State Mater. Sci.* 20 (2016) 308–315.
- [12] T. Frolov, Q. Zhu, T. Oppelstrup, J. Marian, R.E. Rudd, Structures and transitions in bcc tungsten grain boundaries and their role in the absorption of point defects. *Acta Mater.* 159 (2018) 123–134.
- [13] T. Frolov, D.L. Olmsted, M. Asta, Y. Mishin, Structural phase transformations in metallic grain boundaries. *Nat.*

Commun. 4 (2013) 1899.

[14] J. Hickman, Y. Mishin, Extra variable in grain boundary description. Phys. Rev. Mater. 1 (2017) 010601 (R).

[15] D. Chen, J. Wang, T. Chen, L. Shao, Defect annihilation at grain boundaries in α -Fe. Sci. Rep. 3 (2013) 1450.

[16] X. Li, W. Liu, Y. Xu, C.S. Liu, Q.F. Fang, B.C. Pan, J.-L. Chen, G.-N. Luo, Z. Wang, Principal physical parameters characterizing the interactions between irradiation-induced point defects and several tilt symmetric grain boundaries in Fe, Mo and W. J. Nucl. Mater. 444 (2014) 229–236.

[17] G. Duan, X. Li, J. Sun, C. Hao, Y. Xu, Y. Zhang, W. Liu, C.S. Liu, Surface-structure dependence of healing radiation-damage mechanism in nanoporous tungsten. J. Nucl. Mater. 498 (2018) 362–372.

[18] X. Li, et al., Radiation resistance of nano-crystalline iron: Coupling of the fundamental segregation process and the annihilation of interstitials and vacancies near the grain boundaries. Acta Mater. 109 (2016) 115–127.

[19] X. Li, Y. Xu, G. Duan, J. Sun, C. Hao, Y. Zhang, W. Liu, C.S. Liu, Q.F. Fang, On the possibility of universal interstitial emission induced annihilation in metallic nanostructures. J. Nucl. Mater. 500 (2018) 199–212.

[20] N. Chen, L.-L. Niu, Y. Zhang, X. Shu, H.-B. Zhou, S. Jin, G. Ran, G.-H. Lv, F. Gao, Energetics of vacancy segregation to [100] symmetric tilt grain boundaries in bcc tungsten. Sci. Rep. 6 (2016) 36955.

[21] M. Tschopp, K.N. Solanki, F. Gao, X. Sun, M.A. Khaleel, M.F. Horstemeyer, Probing grain boundary sink strength at the nanoscale: Energetics and length scales of vacancy and interstitial absorption by grain boundaries in α -Fe. Phys. Rev. B 85 (2012) 064108.

[22] X. Li, G. Duan, Y. Xu, Y. Zhang, W. Liu, C.S. Liu, Y. Liang, J.-L. Chen, G.-N. Luo, Annihilating vacancies via dynamics reflection and emission of interstitials in nano-crystal tungsten. Nucl. Fusion 57 (2017) 116055.

[23] X.-M. Bai, A.F. Voter, R.G. Hoagland, M. Nastasi, B.P. Uberuaga, Efficient annealing of radiation damage near grain boundaries via interstitial emission. Science 327 (2010) 1631.

[24] M. Jin, P. Cao, S. Yip, M.P. Short, Radiation damage reduction by grain-boundary biased defect migration in nanocrystalline in nanocrystalline Cu. Acta Mater. 155 (2018) 410–417.

[25] L. Zhang, C. Lu, K. Tieu, Y. Shibuta, Dynamic interaction between grain boundary and stacking fault tetrahedron. Scr.

Mater. 144 (2018) 78–83.

[26] Y. Gu, Y. Xiang, D.J. Srolovitz, J.A. El-Awady, Self-healing of low angle grain boundaries by vacancy diffusion and dislocation climb. *Scr. Mater.* 155 (2018) 155–159.

[27] B.P. Uberuaga, L.J. Vernon, E. Martinez, A.F. Voter, The relationship between grain boundary structure, defect mobility, and grain boundary sink efficiency. *Sci. Rep.* 5 (2015) 9095.

[28] V. Borovikov, X.-Z. Tang, D. Perez, X.-M. Bai, B.P. Uberuaga, A.F. Voter, Coupled motion of grain boundaries in bcc tungsten as a possible radiation-damage healing mechanism under fusion reactor conditions. *Nucl. Fusion* 53 (2013) 063001.

[29] L. Zhang, Y. Shibuta, C. Lu, X. Huang, Atomistic simulation of the interaction between point defects and twin boundary. *Phys. Status Solidi B* 255 (2018) 1800228.

[30] I. Adlakha, K.N. Solanki, Atomic-scale investigation of triple junction role on defects binding energetics and structural stability in α -Fe. *Acta Mater.* 118 (2016) 64–76.

[31] X. Li, W. Liu, Y. Xu, C.S. Liu, Q.F. Fang, B.C. Pan, J.-L. Chen, G.-N. Luo, Z. Wang, An energetic and kinetic perspective of the grain boundary role in healing radiation damage in tungsten. *Nucl. Fusion* 53 (2013) 123014.

[32] M. Jin, P. Cao, M.P. Short, Mechanisms of grain boundary migration and growth in nanocrystalline metals under irradiation. *Scr. Mater.* 163 (2019) 66–70.

[33] B.N. Singh, A.J.E. Foreman, Calculated grain size-dependent vacancy supersaturation and its effect on void formation. *Philos. Mag.* 29 (1974) 847–858.

[34] X.-M. Bai, L.J. Vernon, R.G. Hoagland, A.F. Voter, M. Nastasi, B.P. Uberuaga, Role of atomic structure on grain boundary-defect interactions in Cu. *Phys. Rev. B* 85 (2012) 214103.

[35] F.J. Pérez-Pérez, R. Smith, Preferential damage at symmetrical tilt grain boundaries in bcc iron. *Nucl. Instr. and Meth. B* 180 (2001) 322–328.

[36] L. Zhang, M.J. Demkowicz, Radiation-induced mixing between metals of low solid solubility. *Acta Mater.* 76 (2014) 135–150.

- [37] X.-Z. Tang, Y.-F. Guo, Y. Fan, S. Yip, B. Yildiz, Interstitial emission at grain boundary in nanolayered α -Fe. *Acta Mater.* 105 (2016) 147–154.
- [38] M.A. Tschopp, M.F. Horstemeyer, F. Gao, X. Sun, M. Khaleel, Energetic driving force for preferential binding of self-interstitial atoms to Fe grain boundaries over vacancies. *Scr. Mater.* 64 (2011) 908–911.
- [39] X. Li, W. Liu, Y. Xu, C.S. Liu, Q.F. Fang, B.C. Pan, Z. Wang, Energetic and kinetic behaviors of small vacancy clusters near a symmetric $\Sigma 5(3\ 1\ 0)/[0\ 0\ 1]$ tilt grain boundary in bcc Fe. *J. Nucl. Mater.* 440 (2013) 250–256.
- [40] X. Li, et al., Energetic and kinetic dataset on interaction of the vacancy and self-interstitial atom with the grain boundary in α -iron. *Data Brief* 7 (2016) 798–813.
- [40-1] A. Duan, R. Dingreville, E. Martínez, L. Capolungo, Identification of dominant damage accumulation processes at grain boundaries during irradiation in nanocrystalline α -Fe: A statistical study. *Acta Mater.* 110 (2016) 306–323.
- [40-2] J. Xu, J.-B. Liu, S.-N. Li, B.-X. Liu, Y. Jiang, Self-healing properties of nanocrystalline materials: a first-principles analysis of the role of grain boundaries. *Phys. Chem. Chem. Phys.* 18 (2016) 17930.
- [41] M. Samaras, P.M. Perlet, H. Van Swygenhoven, M. Victoria, Stacking fault tetrahedra formation in the neighbourhood of grain boundaries. *Nucl. Instr. and Meth. B* 202 (2003) 51–55.
- [42] A. Esfandiarpour, S.A.H. Feghhi, A.A. Shokri, Effect of atomic grain boundary structures on primary radiation damage in α -Fe. *Nucl. Instr. and Meth. B* 362 (2015) 1–8.
- [43] F.J. Pérez-Pérez, R. Smith, Modelling radiation effects at grain boundaries in bcc iron. *Nucl. Instr. and Meth. B* 153 (1999) 136–141.
- [44] M. Samaras, P.M. Derlet, H. Van Swygenhoven, M. Victoria, SIA activity during irradiation of nanocrystalline Ni. *J. Nucl. Mater.* 323 (2003) 213–219.
- [45] M. Samaras, P.M. Derlet, H. Van Swygenhoven, M. Victoria, Atomic scale modelling of the primary damage state of irradiated fcc and bcc nanocrystalline metals. *J. Nucl. Mater.* 351 (2006) 47–55.
- [46] H. Li, Y. Qin, Y. Yang, M. Yao, X. Wang, H. Xu, S.R. Phillpot, The evolution of interaction between grain boundary and irradiation-induced point defects: Symmetric tilt GB in tungsten. *J. Nucl. Mater.* 500 (2018) 42–49.

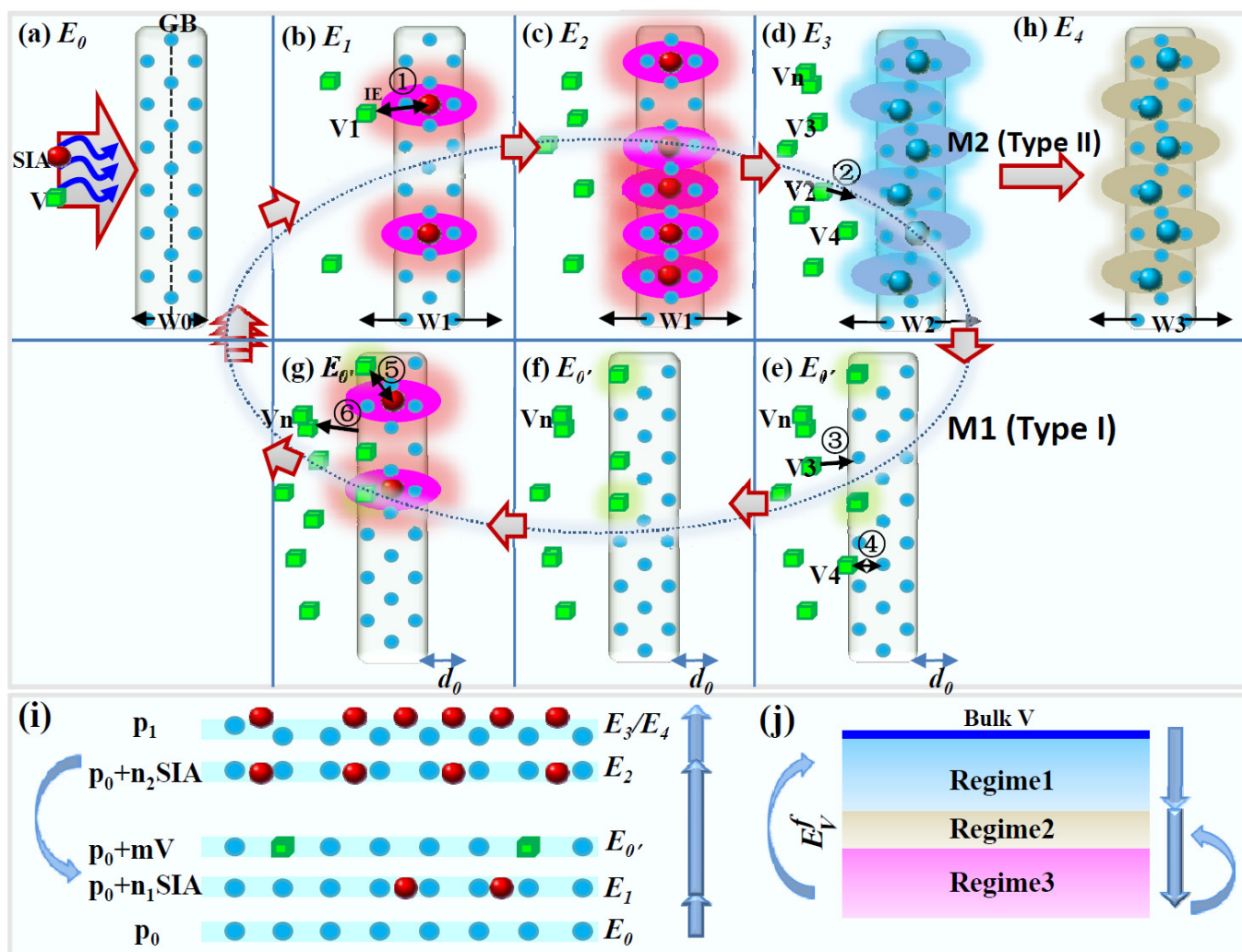
- [47] C.G. Zhang, W.H. Zhou, Y.G. Li, Z. Zeng, X. Ju, Primary radiation damage near grain boundary in bcc tungsten by molecular dynamics simulations. *J. Nucl. Mater.* 458 (2015) 138–145.
- [48] A. Arjhangmehr, S.A.H. Feghhi, A. Esfandiarpour, F. Hatami, An energetic and kinetic investigation of the role of different atomic grain boundaries in healing radiation damage in nickel. *J. Mater. Sci.* 51 (2016) 1017–1031.
- [49] X.-M. Bai, B.P. Uberuaga, The influence of grain boundaries on radiation-induced point defect production in materials: A review of atomistic studies. *JOM.* 65 (2013) 360–373.
- [50] M. Samaras, P.M. Derlet, H. Van Swygenhoven, M. Victoria, Computer simulation of displacement cascades in nanocrystalline Ni. *Phys. Rev. Lett.* 88 (2002) 125505.
- [51] P. Lejček, S. Hofmann, V. Paidar, Solute segregation and classification of [100] tilt grain boundaries in α -iron: consequences for grain boundary engineering. *Acta Mater.* 51 (2003) 3951–3963.
- [52] M.D. Sangid, H.J. Maier, H. Sehitoglu, A physically based fatigue model for prediction of crack initiation from persistent slip bands in polycrystals. *Acta Mater.* 59 (2011) 328–341.
- [53] M.D. Sangid, T. Ezaz, H. Sehitoglu, I.M. Robertson, Energy of slip transmission and nucleation at grain boundaries. *Acta Mater.* 59 (2011) 283–296.
- [54] Z. You, X. Li, L. Gui, Q. Lu, T. Zhu, H. Gao, L. Lu, Plastic anisotropy and associated deformation mechanisms in nanotwinned metals. *Acta Mater.* 61 (2013) 217–227.
- [55] L. Cao, M. Koslowski, Effect of microstructural uncertainty on the yield stress of nanocrystalline nickel. *Acta Mater.* 61 (2013) 1413–1420.
- [56] X. Wu, Y.-W. You, X.-S. Kong, J.-L. Chen, G.-N. Luo, G.-H. Lu, C.S. Liu, Z. Wang, First-principles determination of grain boundary strengthening in tungsten: Dependence on grain boundary structure and metallic radius of solute. *Acta Mater.* 120 (2016) 315–326.
- [57] J.J. Möller, E. Bitzek, Fracture toughness and bond trapping of grain boundary cracks. *Acta Mater.* 73 (2014) 1–11.
- [58] M.A. Gibson, C.A. Schuh, Segregation-induced changes in grain boundary cohesion and embrittlement in binary alloys. *Acta Mater.* 95 (2015) 145–155.

- [58-1] T. Meiners, Z. Peng, B. Gault, C.H. Liebscher, G. Dehm, Sulfur-induced embrittlement in high-purity, polycrystalline copper. *Acta Mater.* 156 (2018) 64–75.
- [58-2] P. Lejček, S. Hofmann, Modeling grain boundary segregation by prediction of all the necessary parameters. *Acta Mater.* 170 (2019) 253–267.
- [59] X.Y. Wang, N. Gao, B. Xu, Y.N. Wang, G.G. Shu, C.L. Li, W. Liu, Effect of irradiation and irradiation defects on the mobility of $\Sigma 5$ symmetric tilt grain boundaries in iron: An atomistic study. *J. Nucl. Mater.* 510 (2018) 568–574.
- [60] X.Y. Wang, N. Gao, W. Setyawan, B. Xu, W. Liu, Z.G. Wang, Effect of irradiation on mechanical properties of symmetrical grain boundaries investigated by atomic simulations. *J. Nucl. Mater.* 491 (2017) 154–161.
- [61] L. Li, P.M. Anderson, M.-G. Lee, E. Bitzek, P. Derlet, H. Van Swygenhoven, The stress-strain response of nanocrystalline metals: A quantized crystal plasticity approach. *Acta Mater.* 57 (2009) 812–822.
- [62] N. Gao, D. Perez, G.H. Lu, Z.G. Wang, Molecular dynamics study of the interaction between nanoscale interstitial dislocation loops and grain boundaries in BCC iron. *J. Nucl. Mater.* 498 (2018) 378–386.
- [63] J. Li, K.Y. Yu, Y. Chen, M. Song, H. Wang, M.A. Kirk, M. Li, X. Zhang, In situ study of defect migration kinetics and self-healing of twin boundaries in heavy ion irradiated nanotwinned metals. *Nano Lett.* 15 (2015) 2922–2927.
- [64] C. Sun, M. Song, K.Y. Yu, Y. Chen, M. Kirk, M. Li, H. Wang, X. Zhang, In situ evidence of defect cluster absorption by grain boundaries in Kr ion irradiated nanocrystalline Ni. *Metall. Mater. Trans. A* 44A (2013) 1966–1974.
- [65] M. Rose, A.G. Balogh, H. Hahn, Instability of irradiation induced defects in nanostructured materials. *Nucl. Instr. and Meth. B* 127-128 (1997) 119–112.
- [66] C.M. Barr, N. Li, B.L. Boyce, K. Hattar, Examining the influence of grain size on radiation tolerance in the nanocrystalline regime. *Appl. Phys. Lett.* 112 (2018) 181903.
- [67] Y. Chimi, A. Iwase, N. Ishikawa, M. Kobiyama, T. Inami, S. Okuda, Accumulation and recovery of defects in ion-irradiated nanocrystalline gold. *J. Nucl. Mater.* 297 (2001) 355–357.
- [68] G.M. Cheng, W.Z. Xu, Y.Q. Wang, A. Misra, Y.T. Zhu, Grain size effect on radiation tolerance of nanocrystalline Mo. *Scr. Mater.* 123 (2016) 90–94.

- [69] K.Y. Yu, Y. Liu, C.Sun, H. Wang, L. Shao, E.G. Fu, X. Zhang, Radiation damage in helium ion irradiated nanocrystalline Fe. *J. Nucl. Mater.* 425 (2012) 140–146.
- [70] O. El-Atwani, J.E.N. II, A.C. Leff, B.R. Muntiferi, J.K. Baldwin, K. Hattar, M.L. Taheri, The role of grain size in He bubble formation: Implications for swelling resistance. *J. Nucl. Mater.* 484 (2017) 236–244.
- [71] T.S. Byun, D.T. Hoelzer, J.H. Kim, S.A. Maloy, A comparative assessment of the fracture toughness behavior of ferritic-martensitic steels and nanostructured ferritic alloys. *J. Nucl. Mater.* 484 (2017) 157–167.
- [72] B. Muntiferi, Y. Fang, A.C. Leff, A. Dunn, J. Qu, M.L. Taheri, R. Dingreville, K. Hattar, In situ transmission electron microscopy He⁺ implantation and thermal aging of nanocrystalline iron. *J. Nucl. Mater.* 482 (2016) 139–146.
- [73] W.B. Liu, J.H. Zhang, Y.Z. Ji, L.D. Xia, H.P. Liu, D. Yun, C.H. He, C. Zhang, Z.G. Yang, Comparative study of He bubble formation in nanostructured reduced activation steel and its coarsen-grained counterpart. *J. Nucl. Mater.* 500 (2018) 213–219.
- [74] M. Song, et al., Response of equal channel angular extrusion processed ultrafine-grained T91 steel subjected to high temperature heavy ion irradiation. *Acta Mater.* 74 (2014) 285–295.
- [75] C. Du, et al., Ultrastrong nanocrystalline steel with exceptional thermal stability and radiation tolerance. *Nat. Commun.* 9 (2018) 5389.
- [76] C. Sun, et al., Superior radiation-resistant nanoengineered austenitic 304L stainless steel for applications in extreme radiation environments. *Sci. Rep.* 5 (7801) 2015.
- [77] N. Li, J. Wang, Y.Q. Wang, Y. Serruys, M. Nastasi, A. Misra, Incoherent twin boundary migration induced by ion irradiation in Cu. *J. Appl. Phys.* 113 (2013) 023508.
- [78] W.Z. Han, M.J. Demkowicz, E.G. Fu, Y.Q. Wang, A. Misra, Effect of grain boundary character on sink efficiency. *Acta Mater.* 60 (2012) 6341–6351.
- [79] Y. Chen, J. Li, K.Y. Yu, H. Wang, M.A. Kirk, M. Li, X. Zhang, In situ studies on radiation tolerance of nanotwinned Cu. *Acta Mater.* 111 (2016) 148–156.

- [80] W. Han, E.G. Fu, M.J. Demkowicz, Y. Wang, A. Misra, Irradiation damage of single crystal, coarse-grained, and nanograined copper under helium bombardment at 450 °C. *J. Mater. Res.* 28 (2013) 2763–2770.
- [81] O. El-Atwani, K. Hattar, J.A. Hinks, G. Greaves, S.S. Harilal, A. Hassanein, Helium bubble formation in ultrafine and nanocrystalline tungsten under different extreme conditions. *J. Nucl. Mater.* 458 (2015) 216–223.
- [82] O. El-Atwani, A. Suslova, T.J. Novakowski, K. Hattar, M. Efe, S.S. Harilal, A. Hassanein, In-situ TEM/heavy ion irradiation on ultrafine-and nanocrystalline-grained tungsten: Effect of 3 MeV Si, Cu and W ions. *Mater. Char.* 99 (2015) 68–76.
- [83] Z. Chen, L.-L. Niu, Z. Wang, L. Tian, L. Kecskes, K. Zhu, Q. Wei, A comparative study on the in situ helium irradiation behavior of tungsten: Coarse grain vs. nanocrystalline grain. *Acta Mater.* 147 (2018) 100–112.
- [84] O. El-Atwani, E. Esquivel, M. Efe, E. Aydogan, Y.Q. Wang, E. Martinez, S.A. Maloy, Loop and void damage during heavy ion irradiation on nanocrystalline and coarse grained tungsten: Microstructure, effect of dpa rate, temperature, and grain size. *Acta Mater.* 149 (2018) 206–219.
- [85] O. El-Atwani, J.A. Hinks, G. Greaves, S. Gondeman, T. Qiu, M. Efe, J.P. Allain, In-situ TEM observation of the response of ultrafine- and nanocrystalline-grained tungsten to extreme irradiation environments. *Sci. Rep.* 4 (2014) 4716.
- [86] O. El-Atwani, E. Esquivel, E. Aydogan, E. Martinez, J.K. Baldwin, M. Li, B.P. Uberuaga, S.A. Maloy, Unprecedented irradiation resistance of nanocrystalline tungsten with equiaxed nanocrystalline grains to dislocation loop accumulation. *Acta Mater.* 165 (2019) 118–128.
- [87] T. Chookajorn, H.A. Murdoch, C.A. Schuh, Design of stable nanocrystalline alloys. *Science* 337 (2012) 951.
- [88] K.A. Darling, M. Rajagopalan, M. Komarasamy, M.A. Bhatia, B.C. Hornbuckle, R.S. Mishra, K.N. Solanki, Extreme creep resistance in a microstructurally stable nanocrystalline alloy. *Nature* 537 (2016) 378–381.
- [89] M.I. Mendelev, S. Han, D.J. Srolovitz, G.J. Ackland, D.Y. Sun, M. Asta, Development of new interatomic potentials appropriate for crystalline and liquid iron. *Philos. Mag.* 83 (2003) 3977–3994.
- [90] G. Henkelman, H. Jónsson, Improved tangent estimate in the nudged elastic band method for finding minimum energy paths and saddle points. *J. Chem. Phys.* 113 (2000) 9978–9985.

- [91] K. Cheng, L. Zhang, C. Lu, K. Tieu, Coupled grain boundary motion in aluminium: the effect of structural multiplicity. Sci. Rep. 6 (2016) 25427.
- [92] L. Zhang, C. Lu, K. Tieu, A review on atomistic simulation of grain boundary behaviors in face-centered cubic metals. Comput. Mater. Sci. 118 (2016) 180–191.
- [93] W. Xing, A.R. Kalidindi, D. Amram, C.A. Schuh, Solute interaction effects on grain boundary segregation in ternary alloys. Acta Mater. 161 (2018) 285–294.



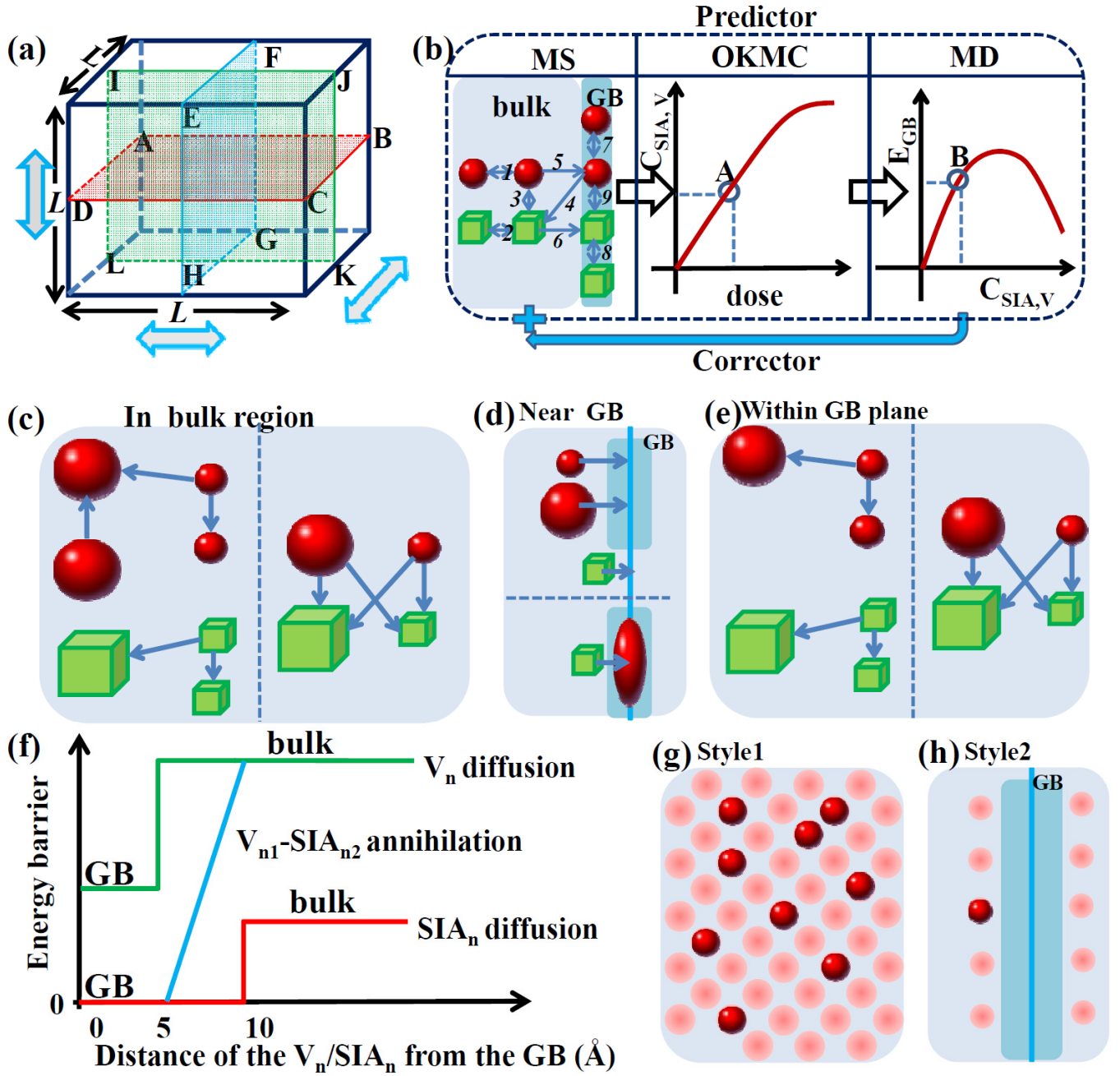


Fig. 1. (a) Geometric model for OKMC modeling radiation damage accumulation in NC Fe. The grain size is L . The GB locates at the center of the cubic; planes ABCD, EFGH, IJKL are GBs. (b) Schematic illustration of the combination of the MS, MD and OKMC methods simulating defects structure evolution under accumulative radiation. The red sphere represents a SIA and the green cubic is for a V. Here, 1–9 represent the fundamental atomic processes incorporated into the OKMC model, including SIA/V diffusion and clustering in the bulk (1/2), SIA-V annihilation in the bulk (3), IE-induced annihilation of the SIA-V near the GB (4), SIA/V segregation from the bulk to the GB (5/6), SIA/V migration and clustering at the GB (7/8), and SIA-V annihilation within the GB (9). $C_{SIA,V}$ denotes the SIA/V concentration in the simulation

model. E_{GB} means the GB energy. Actually, the curve of $C_{SIA,V} \sim dose$ illustrates the variation of the SIA/V distribution and concentration with the radiation dose. Similarly, the curve of $E_{GB} \sim C_{SIA,V}$ denotes the $C_{SIA,V}$ dependent GBA energy and SIA/V-GB interactions. (c) Illustration of the interaction between two defects in the bulk region. Here, the large red sphere represents a SIA-cluster, and the large cubic is for a V-cluster. (d) Illusion of the SIA_n/V_n segregation near the GB. (e) Illustration of the SIA_n/V_n behavior within the GB. (f) shows the energy barrier profiles for the SIA_n/V_n diffusion and their annihilation near the GB. (g) and (h) Illustration of the two styles of producing a certain concentration of the SIA_n/V_n within the GB.

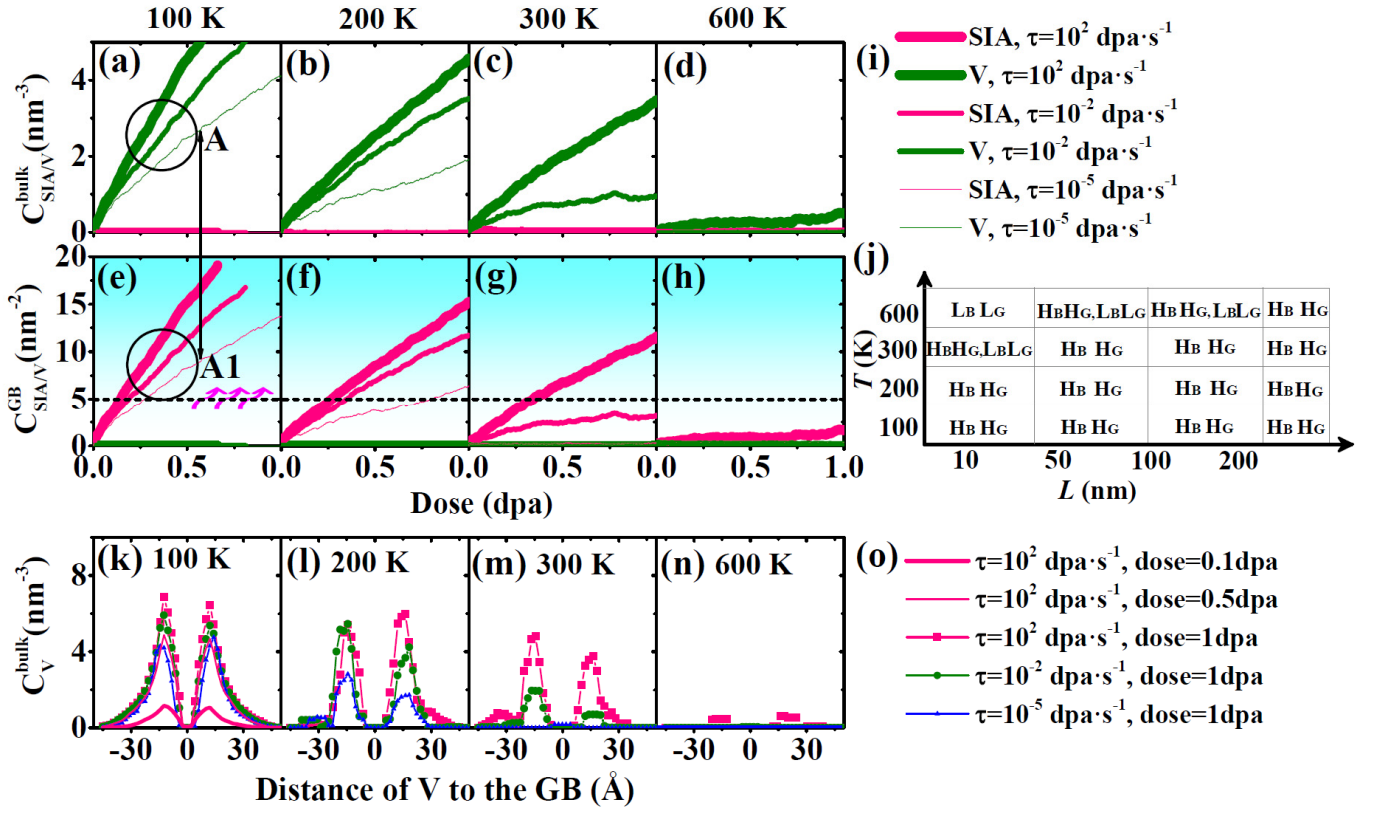


Fig. 2. (a–d) The bulk SIA/V concentration ($C_{SIA/V}^{bulk}$) as a function of the radiation dose at different temperatures of 100, 200, 300 and 600 K. (e–h) The SIA/V concentration at the GB ($C_{SIA/V}^{GB}$) as a function of the radiation dose at the above four temperatures. The legend for (a–h) is given in (i). In (e–h), the horizontal dash line separates the two possible regimes where the GB responses to irradiation via different mechanisms. Symbol A in (a) and $A1$ in (e) respectively mark defects accumulation in the bulk and at the GB under a certain radiation dose. (j) Illustration of the SIA/V concentration level in the bulk and at the GB after about 1 dpa in the regime of temperature (T) and grain size (L). Here, H_B and L_B respectively represent the high and low C_V^{bulk} , while H_G and L_G represent the corresponding high and low C_{SIA}^{GB} (here, the high level of defects concentration means the concentration increases with radiation dose). (k–n) The bulk V concentration as a function of the distance of the V to the GB at different temperatures of 100, 200, 300 and 600 K. The legend for (k–n) is given in (o). Note that, in (a–h) and (k–n) L is 10 nm. As calculating C_V^{bulk} , the Vs near the GB were also considered as bulk defects. In (k–n), the curves were smoothed by using a moving average filter with a span of 5.

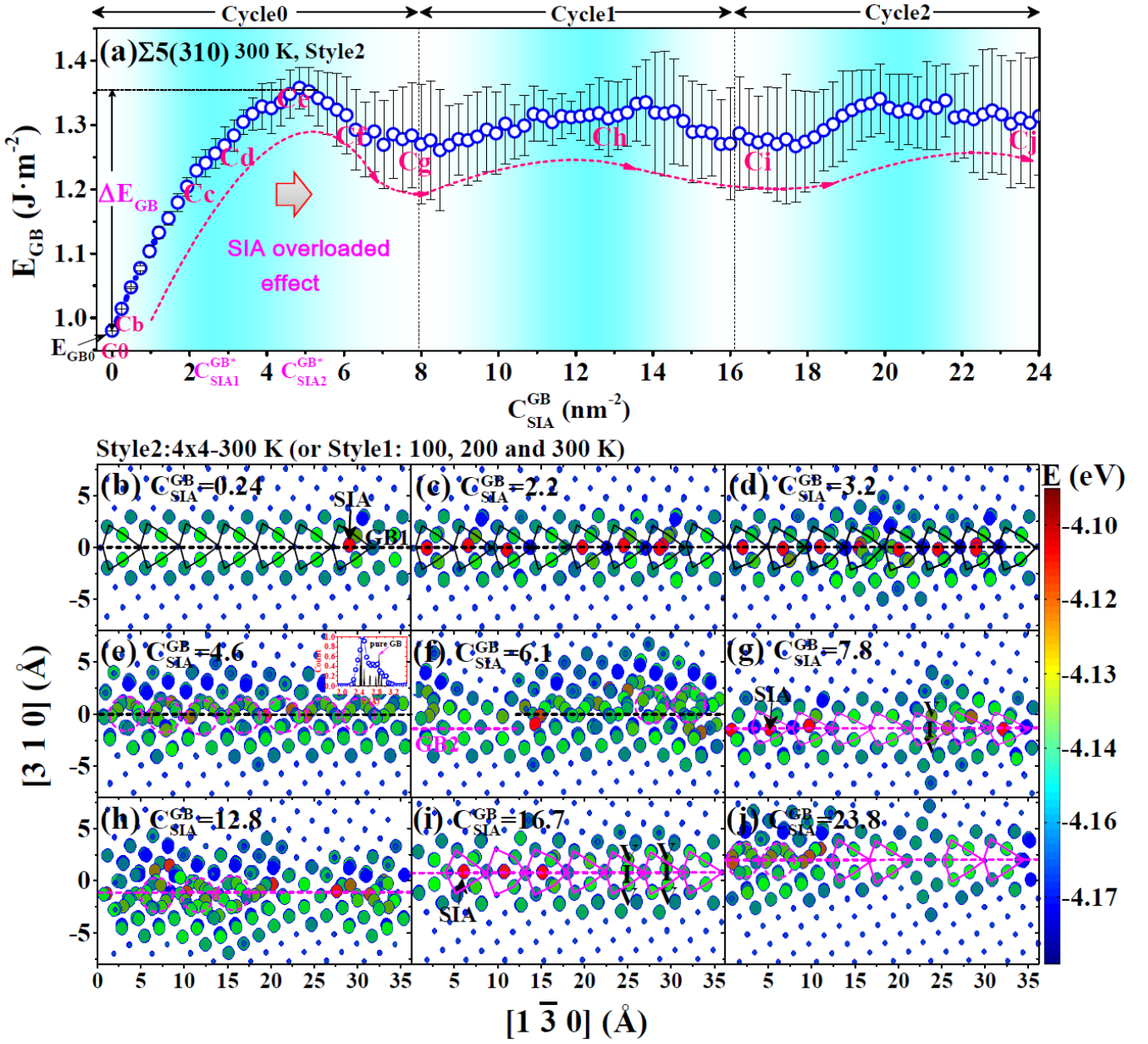


Fig. 3. (a) GB energy (E_{GB}) profile as a function of the loaded SIA concentration at the GB of $\Sigma 5(3\ 1\ 0)/[0\ 0\ 1]$ (C_{SIA}^{GB}) in the manner of *Style2* (Fig. 1(h)). Error bars here indicate the variation range of the calculated E_{GB} from multiple independent MD simulations, while the pink dash line indicates the variation trend of the profile. E_{GB0} is for the energy of a pure GB without SIAs loaded, while ΔE_{GB} is the variation in E_{GB} relative to E_{GB0} . (b–j) The relaxed structures of the GB loaded with several different concentrations of SIAs. The horizontal dash black line indicates the initial GB position prior to the structural relaxation of the GB with SIAs. In (f–j), the horizontal pink line indicates the GB position after relaxation. In (b–j), the atoms are colored with their potential energies (E), as shown by the colorbar on the right hand. In (a), C_0 is zero, while symbols C_b , C_c , C_d , C_e , C_f , C_g , C_h , C_i , C_j respectively denote the C_{SIA}^{GB} in (b–j). In (e), the inset figure shows

the distribution of the atom separation distance in the two GB systems with SIA concentrations of 0.0 and about 4.6 nm^{-2} . The calculated regions are limited to the atom layers near the GB with the width of 6 Å. For the pure GB, such region consists of three atom layers on each side of the GB.

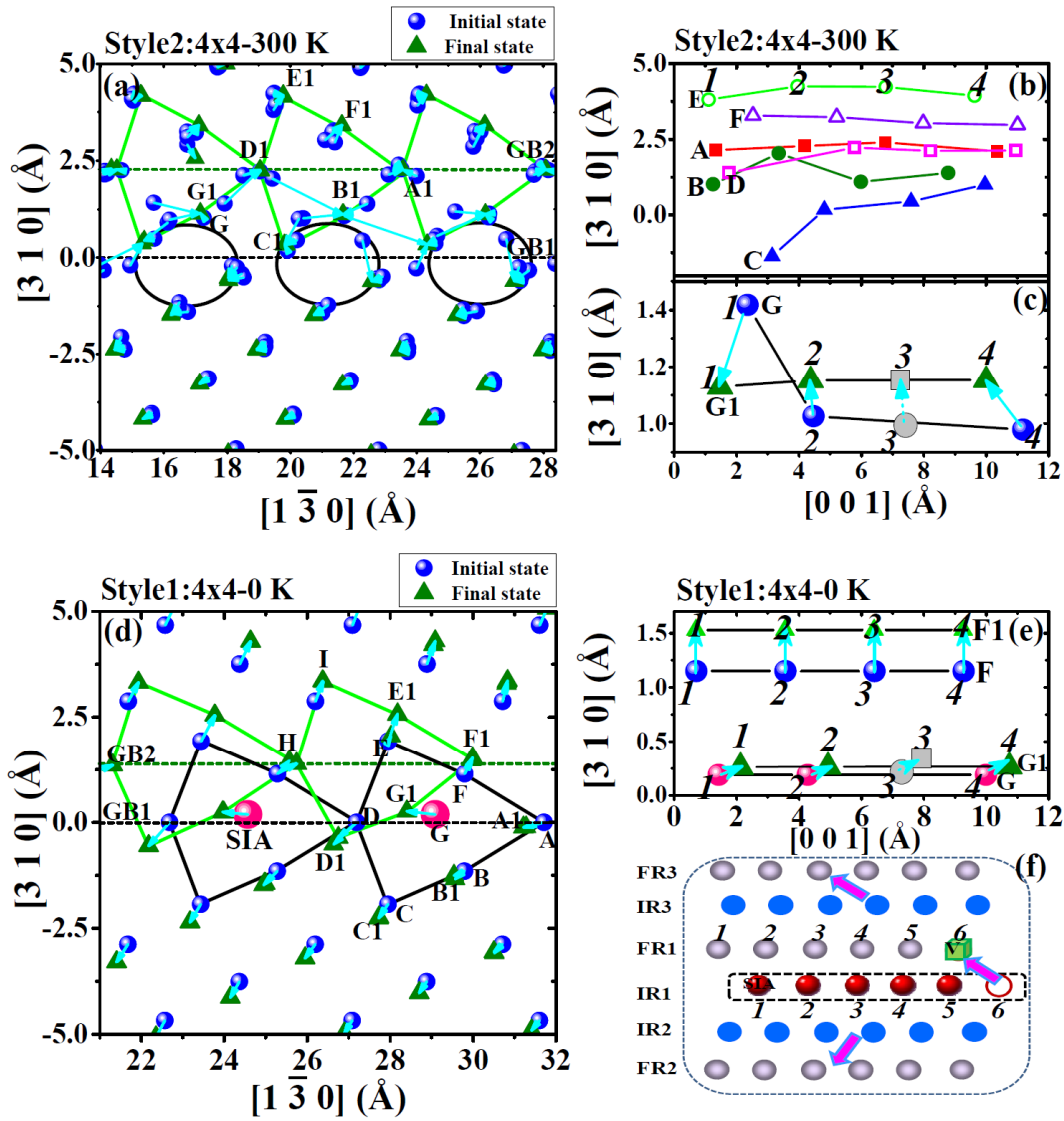


Fig. 4. (a–c) Relaxation process of the GB of $\Sigma 5(3\ 1\ 0)/[0\ 0\ 1]$ loaded with a certain concentration of SIAs in the manner of *Style2*. (a) shows the atom motion process during the transition of the GB system by connecting the initial atom position to the final position in the two GB systems. The horizontal dash black and green lines respectively indicate the initial and final GB positions. The black circle and green polygon indicate the GB structural unit before and after transition, respectively. (b) shows the corresponding atoms in initial state GBs1(A, B, C, D, E, F) to that in final state GBs2 (A1, B1, C1, D1, E1, F1). Note that A1/B1/C1/D1/E1/F1 mark a specific column of atoms aligned along $[0\ 0\ 1]$ in GBs2. The atoms in one column are further indicated by 1, 2, 3, 4. In GBs1, the corresponding column of atoms A/B/C/D/E/F in GBs1 are not well along $[0\ 0\ 1]$ due to the distortion induced by the loaded SIAs. (c) shows the transition of the atoms G in GBs1 to G1 in GBs2. Note that the gray sphere denotes the atom that actually does not exist, and hence the gray square represents the vacancy formed in atom column G1. (d) and (e) present the similar

transition of the GB as the SIA is put in to the GB in the manner of *Style1* at 0 K. (f) Illustration of the SIA-V transition process during the GB relaxation loaded with excess SIAs. *IR1*, *IR2* and *IR3* denote the atom columns in the initial state, while *FR1*, *FR2* and *FR3* represent the atom columns in the final state after relaxation. The red spheres denote the interstitials trapped at the initial GB state, while the light green cubic represents the vacancy formed in the final GB state after relaxation.

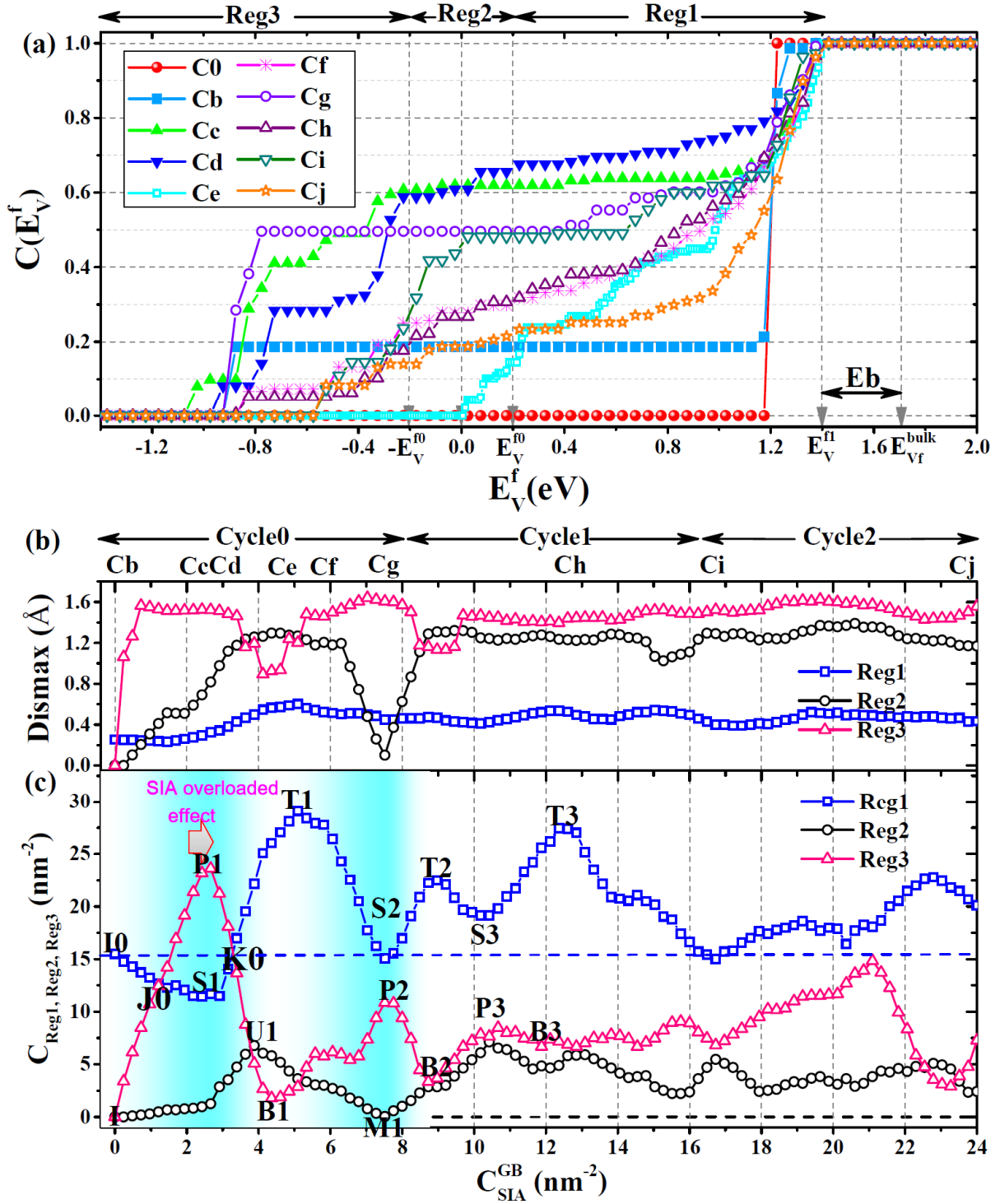


Fig. 5. (a) Cumulative distribution function $C(E_V^f)$ in several GB systems loaded with different concentration levels of the SIAs. Symbols *Reg1*, *Reg2* and *Reg3* represent three regimes with different site stabilities; in *Reg1*, $E_V^{f1} < E_V^f < E_{Vf}^{bulk} - E_b$, in *Reg2*, $-E_V^{f1} < E_V^f < E_V^{f1}$, and in *Reg3*, $E_V^f < -E_V^{f1}$. Here, E_b and E_V^{f1} were assigned to be 0.3 and 0.2 eV, respectively. (i) shows the average maximal displacement of the atoms after the structural relaxation at 0 K of the GB with a vacancy at a specific site in the three regime as a function of C_{SIA}^{GB} , represented by $dismax_{Reg1,Reg2,Reg3}$. (j) shows the site density of the three regimes as a function of C_{SIA}^{GB} .

($C_{\text{Reg1,Reg2,Reg3}}$), defined as the number of sites in a specific E_{ν}^f regime divided by the GB area. Note that, the curves in (j) were smoothed by using a moving average filter with the span for the moving average of 5. C_0 is zero, while symbols $C_b, C_c, C_d, C_e, C_f, C_g, C_h, C_i, C_j$ respectively denote the C_{SA}^{GB} in Fig. 3(b–j).

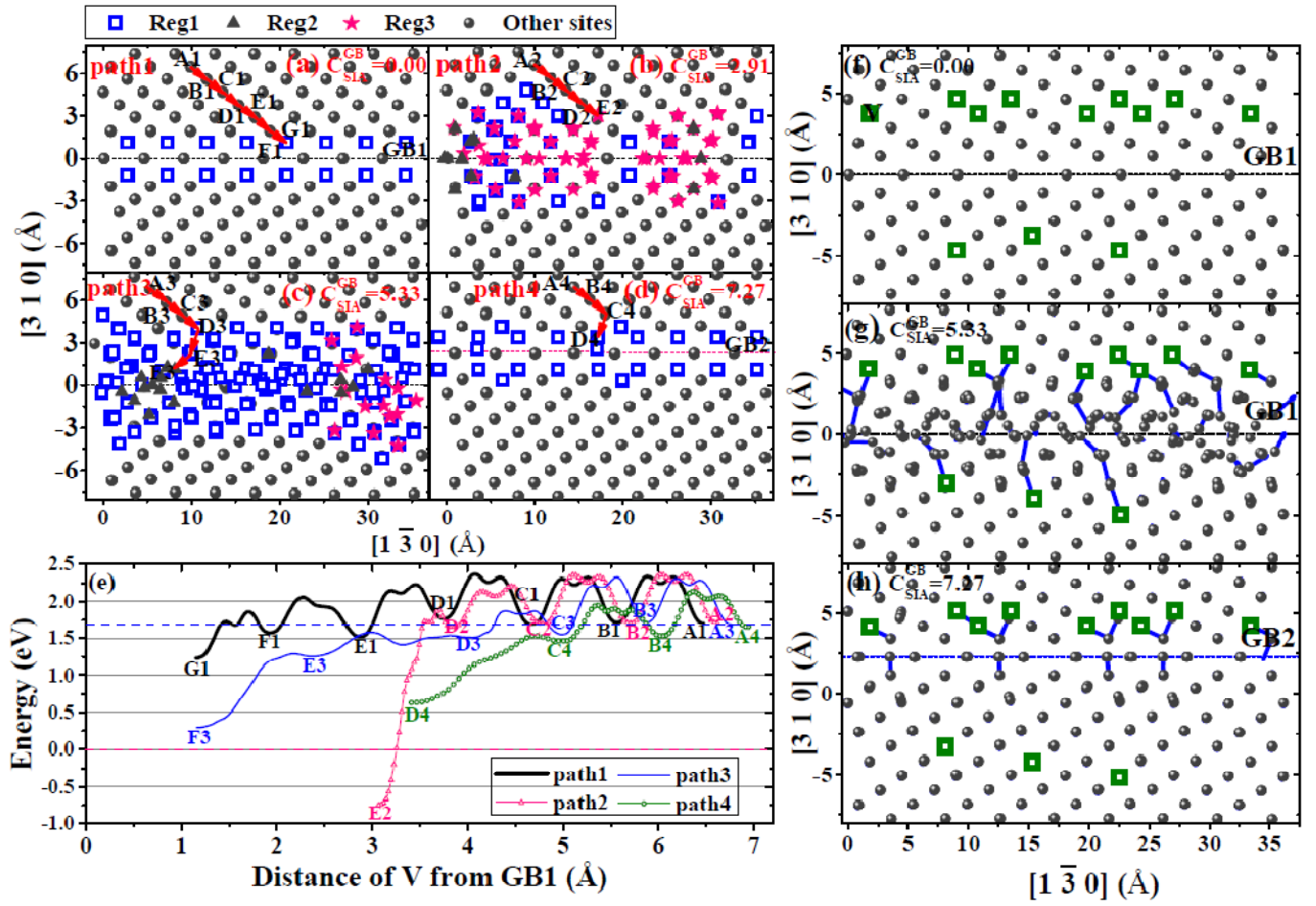


Fig. 6. (a–e) show the energetic and kinetic properties of the V near several typical GB systems with different concentrations of SIAs. In (a–d), the sites with different stability are shown by different colored symbols. The horizontal dash line indicates the GB position. (e) The energy profiles for the V diffusion along several typical paths near the GB. The two horizontal red and blue dash lines mark zero point and bulk E_V^f , respectively. The corresponding paths are illustrated in (a–d). (f–h) Interaction of the V with GB $\Sigma 5(310)/[001]$ that has distinct structures revealed by MD simulations at 300 K. (f) The GB is pure without SIA loading, (g) the GB has a meta-stable phase, and (h) the GB consists of Vs. A vacancy is denoted by a green square. The horizontal dash blue line indicates the GB position. The atoms positions before and after 50 ps at 300 K were connected to show the dynamic behavior of the V. In the three systems, the Vs were created initially at the same sites. The minimal distance of the V from the pure GB is about 5 Å. The V concentration near the GB is about 7.6 nm^{-3} .

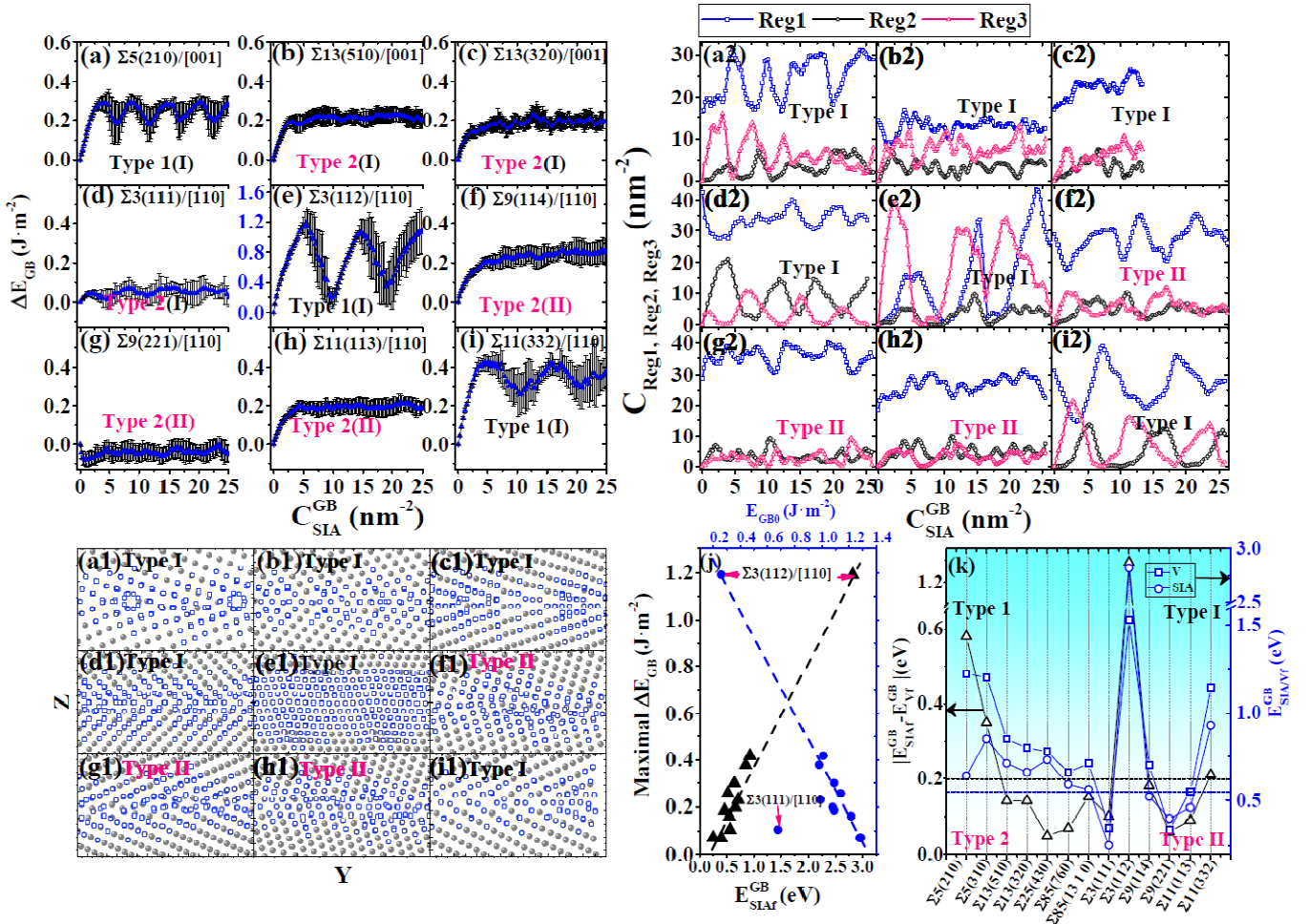


Fig. 7. (a–i) GB energy profile as a function of the loaded C_{SIA}^{GB} in the manner of *Style2* (Fig. 1(h)). Error bars here indicate the variation range of the calculated E_{GB} from multiple independent MD simulations. Here, ΔE_{GB} is E_{GB} referred to the GB energy of a pure GB (E_{GB0}). (a1–i1) The GB structures loaded with a concentration of about 25.0 nm⁻² SIAs. The atoms are colored with their potential energies by using the identical scheme to that in Fig. 3. In (a–i), axis *Z* is along $[2\ 1\ 0]$, $[5\ 1\ 0]$, $[3\ 2\ 0]$, $[1\ 1\ 1]$, $[1\ 1\ 2]$, $[1\ 1\ 4]$, $[2\ 2\ 1]$, $[1\ 1\ 3]$, and $[3\ 3\ 2]$, respectively. In (a–c), axis *Y* is along $[1\ \bar{2}\ 0]$, $[1\ \bar{5}\ 0]$, $[2\ \bar{3}\ 0]$, respectively. In (d–i), *Y* is along $[1\ \bar{1}\ 0]$. (a2–i2) The site density of the three regimes *Reg1*, *Reg2* and *Reg3* as a function of C_{SIA}^{GB} . Symbols *Reg1*, *Reg2* and *Reg3* have the same meaning as that in Fig. 5. Here, E_b and E_V^{f1} were also assigned to be 0.3 and 0.2 eV, respectively. (j) shows the relation of the maximal ΔE_{GB} to the formation energy of a single SIA at a pure GB (E_{SIA}^{GB} , bottom axis) and E_{GB0} (top axis). (k) shows the absolute difference between the SIA and V formation energy at the GB ($|E_{SIA}^{GB} - E_V^{GB}|$) (left axis) and the minimal SIA/V formation energy at the GB (right axis) as a function of the GB type.

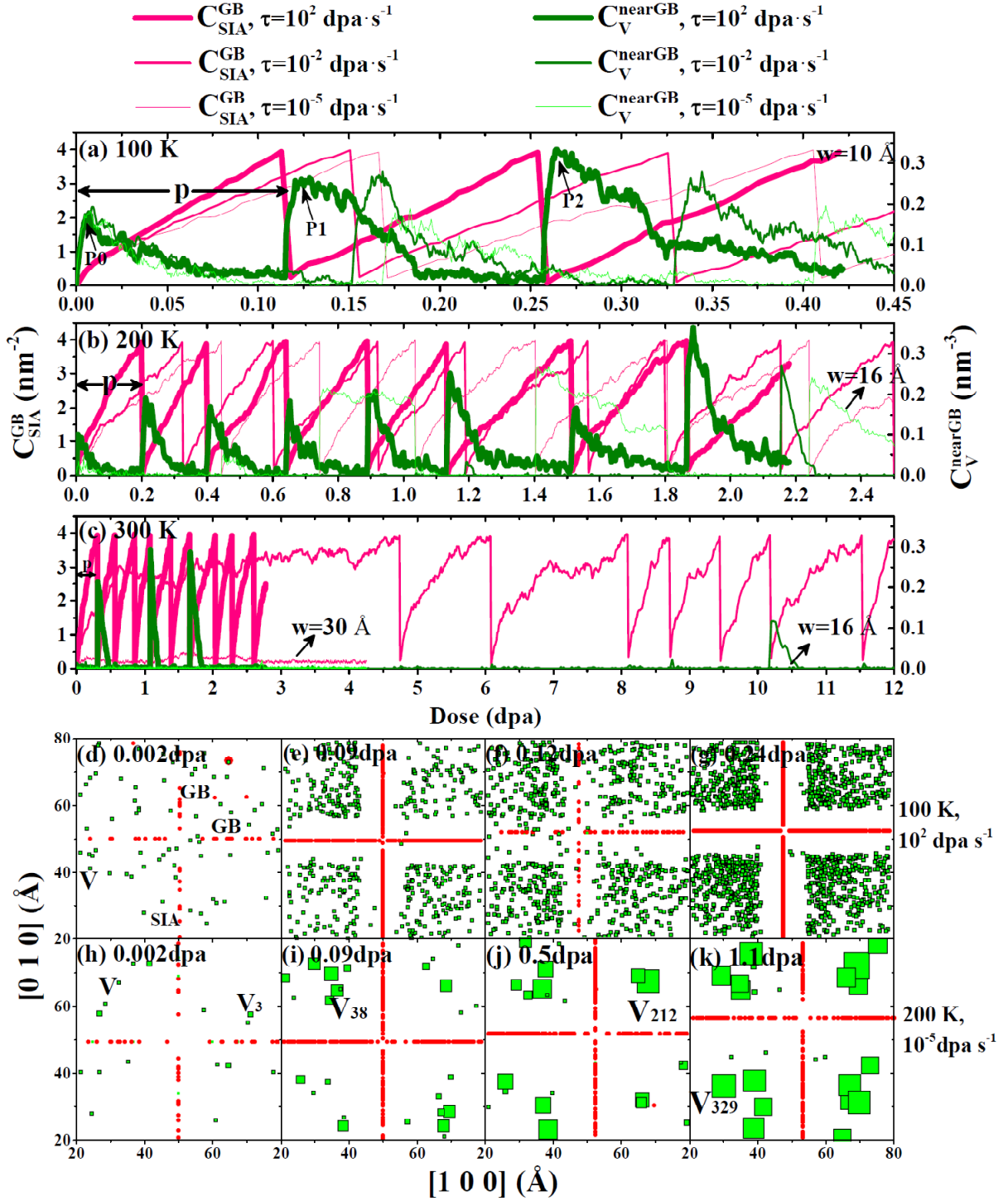


Fig. 8. (a–c) Variation in C_{SIA}^{GB} (the left axis) and the corresponding V concentration near the GB (C_V^{nearGB}) (the right axis) with radiation dose at several values of T and τ . According to Fig. 3(a), the critical SIA concentration at the GB was set 4.0 nm^{-2} for inducing the GB motion. Each time, the GB migrates along a random direction jumping over a distance of 2.5 \AA . The grain size is 10 nm . The region near the GB was defined as the atom layers across the GB with a width of W . W was assigned to be 10 \AA in most cases. At T of 200 K and τ of $10^{-5} \text{ dpa} \cdot \text{s}^{-1}$, W was given of 16 \AA . At T of 300 K and τ of $10^{-5} \text{ dpa} \cdot \text{s}^{-1}$, W was given of 30 \AA .

Å. At a T of 300 K and τ of 10^{-2} dpa \cdot s $^{-1}$, W was given of 16 Å. At such relatively high T and /or low τ , there is no defects survived near the region with a certain distance from the GB. Here, C_V^{nearGB} was defined as the number of Vs in the region near the GB divided by the volume of the region. The volume was calculated as W times the GB area. (d–k) shows typical snapshots for the microstructure evolution at an elevated T and τ . In this visualization scheme, a V-cluster is displayed by a red square, while a SIA-cluster is shown by a red filled circle. The radius of the square/circle is proportional to the real size of the V/SIA-cluster.

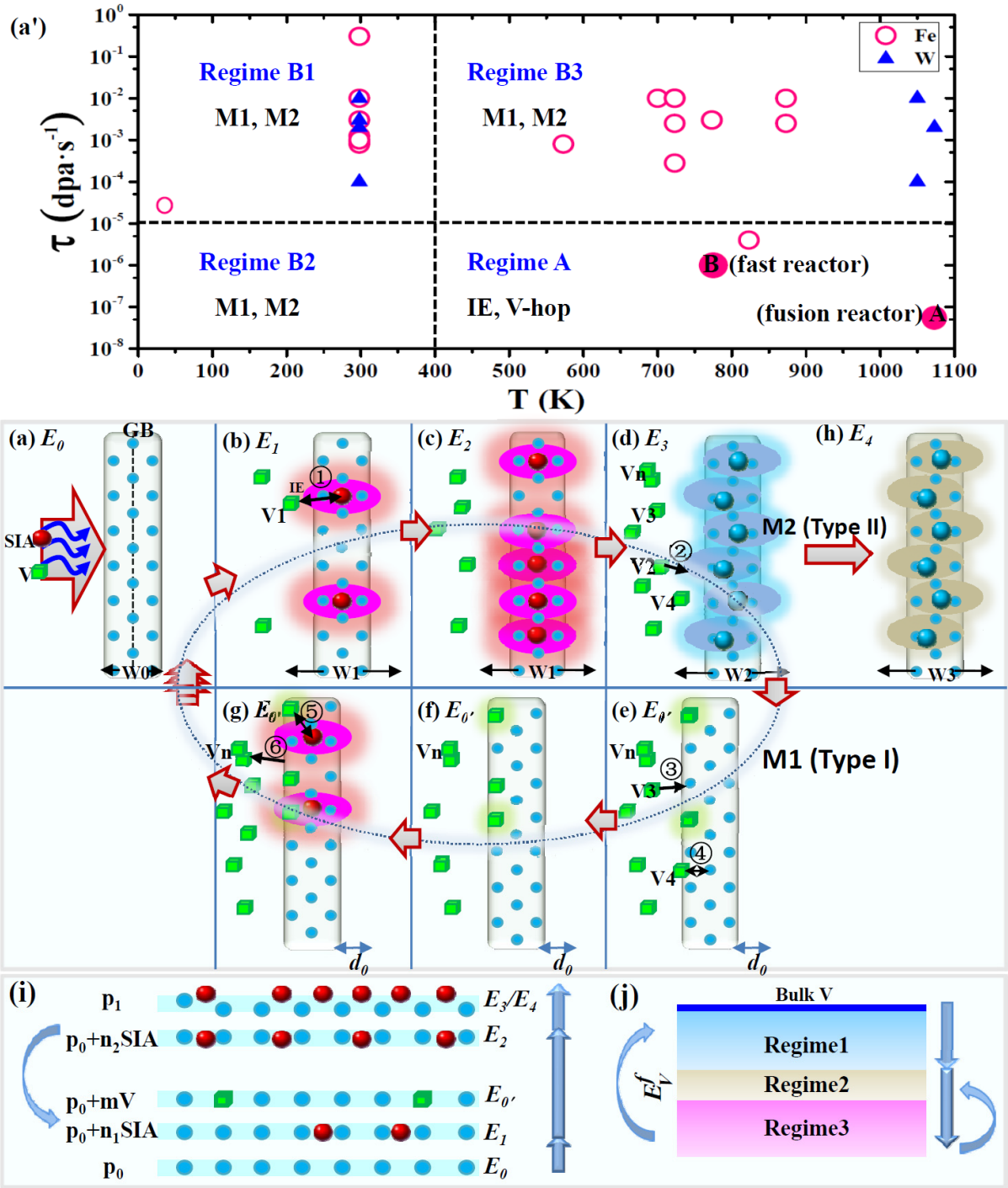


Fig. 9. (a') Illustration of the T - τ parameter regime where the data points are obtained from references [1]. (a-j) Schematic illustration of two kinds of the GB response patterns to cumulative irradiation. A SIA is denoted by a red sphere and a V is represented by a green cubic. The light blue sphere indicates the atoms at the GB, illustrating the GB structure and acting reference atoms for the SIA/V site within the GB. The vertical dash line in (a) indicates the GB position. The pink filled ellipse in (b), (c) and (g) represents the annihilation region formed around a SIA trapped at the GB. The deep blue filled ellipse in (d) represents the extended enhanced diffusion region for V near the meta-stable GB phase, while the large blue sphere represents the

SIA that loses its identity at the GB. Symbols W_0 , W_1 and W_2 respectively represents the width of the pure GB, the GB with SIAs, and the meta-stable GB for trapping/annihilating the V. Symbols E_0 , E_1 , E_2 , E_3 and E_0' respectively denotes the energy for the pristine GB, the GB with small concentration of SIAs, the GB with high concentration of SIAs, the meta-stable GB and the GB containing a certain concentration of Vs. symbol d_0 in (e–g) denotes the distance for the GB migration after the transition from (d) to (e). (i) illustrates the energy and structural variation during a response period of the GB to cumulative irradiation. Symbol ① marks the IE -induced annihilation of the SIA with the V near the GB, ② marks the trapping of the V by the meta-stable GB, ③ marks the trapping of the V by the GB containing Vs, ④ marks the trapping of the V by a migrating GB, ⑤ marks the annihilation of the V at the GB with the SIA nearby, and ⑥ denotes the clustering of the V near the GB.

Supplementary materials for

A general self-consistent framework for studying cumulative displacement damage in nanostructured metals based on parameter passing and structural feedback between atomic and coarse-grained techniques

Xiangyan Li^{a, 1}, Yange Zhang^{a, 1}, Yichun Xu^{a, 1}, Xuebang Wu^{a, *}, Xianping Wang^a, C.S. Liu^{a, **}, Q.F. Fang^a, Jun-Ling Chen^b, G.-N. Luo^b, Zhiguang Wang^c, X. Liu^d

^a Key Laboratory of Materials Physics, Institute of Solid State Physics, Chinese Academy of Sciences, P.O. Box 1129, Hefei 230031, PR China

^b Institute of Plasma Physics, Chinese Academy of Sciences, Hefei 230031, PR China

^c Institute of Modern Physics, Chinese Academy of Sciences, Lanzhou 730000, PR China

^d Southwestern Institute of Physics, Chengdu, Sichuan 610041, China

E-mail: xbwu@issp.ac.cn and cslu@issp.ac.cn (C.S. Liu)

¹ These authors contributed equally to this work.

This file includes:

Fig. S1–S15

Tables S1–S8

Text S1

References S1–S24

1. Supplementary figures

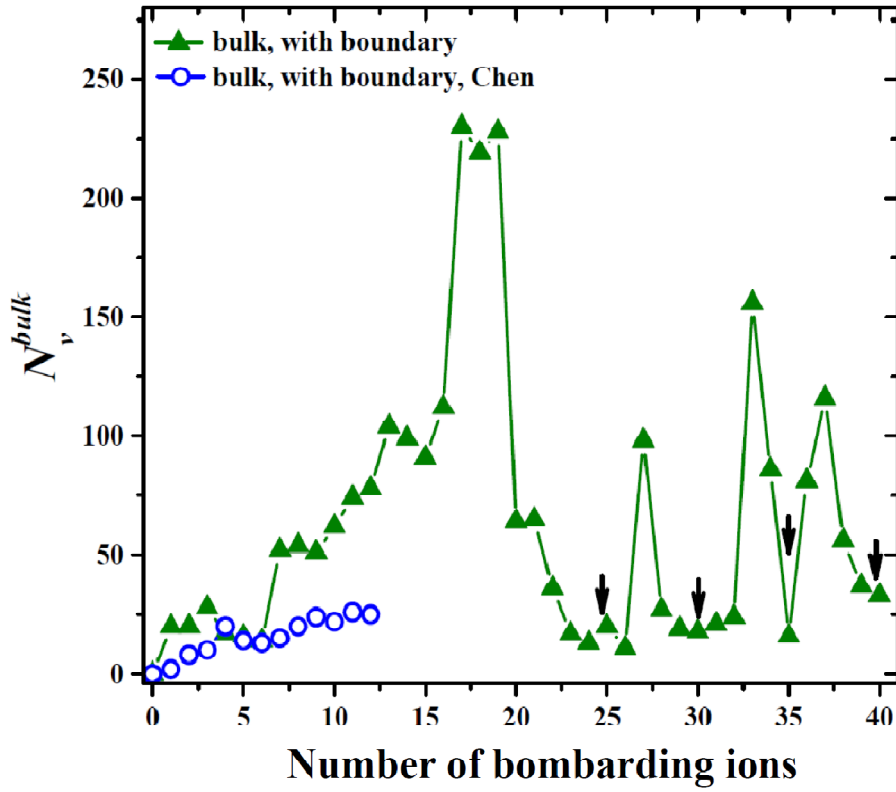


Fig. S1. The number of bulk vacancies (N_v^{bulk}) after the irradiation to the symmetric tilt grain boundary (GB) $\Sigma 5(3\ 1\ 0)/[0\ 0\ 1]$ by many consecutive 3 keV-PKAs (primary knock-on atom, PKA) at a time interval of 50 ps in α -iron (Fe). Results from Ref. [S1] are also shown for comparison. Molecular dynamics (MD) was performed to study cascade-induced damage near the GB at 1000 K using the velocity-Verlet method for the numerical integration, and the simulations ran for about 5000 ps. An atom at one side of the GB was selected as the PKA. The atom was given 3 keV of kinetic energy with its velocity directed perpendicularly toward the GB. The atoms in the outermost layers of the moving region, with a thickness of two times the lattice constant, were coupled with a velocity-rescaling thermostat to absorb the cascade energy and maintain the system temperature at 1000 K. The embedded-atom-method (EAM) interatomic potential developed by Mendelev et al was used to model the interatomic interaction [S2], and the short-range form of the potential was splined to reproduce the high-energy empirical potential of Ziegler et al [S3].

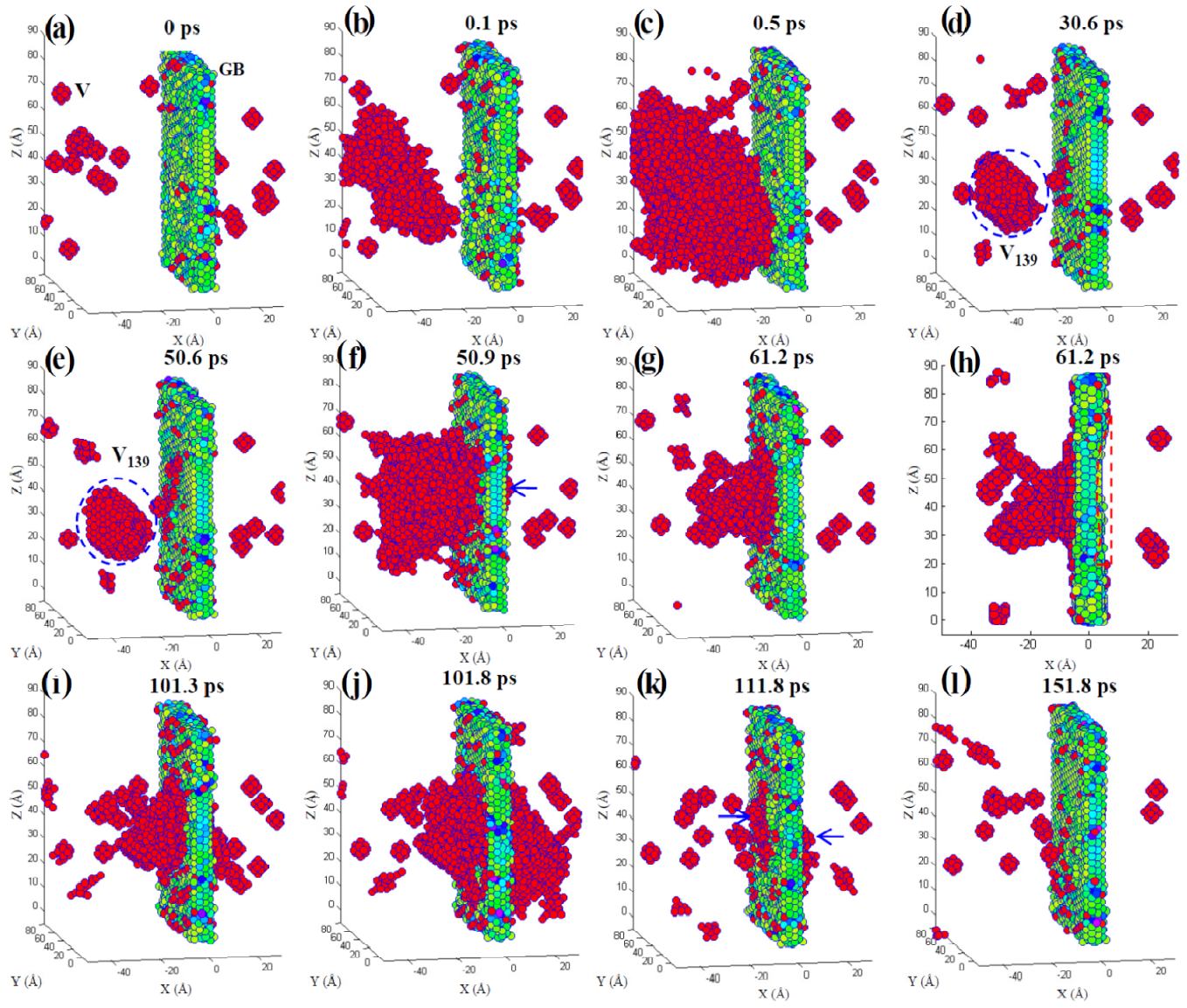
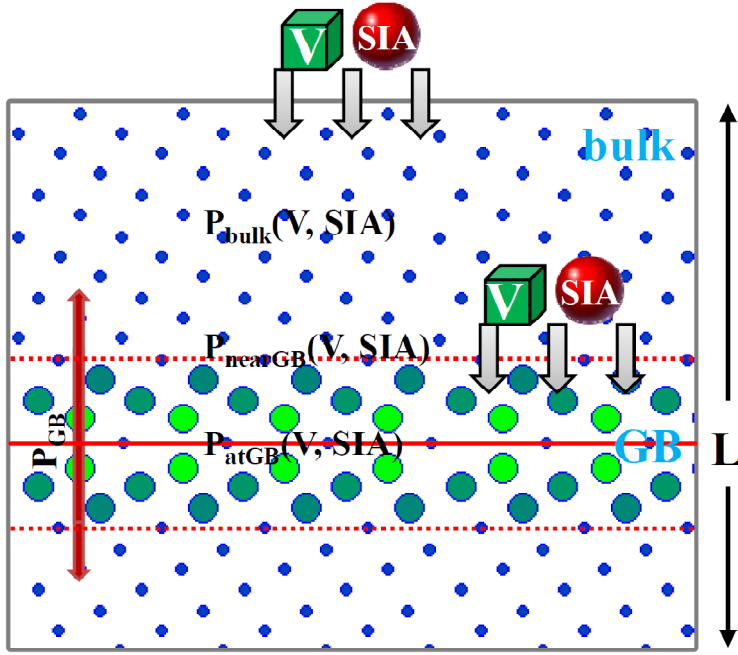


Fig. S2. Snapshots for the accumulation of vacancies nearby the GB and their absorption by the migrating GB. (a–g) The growth of accumulated vacancies in the bulk region during the successive radiation to the GB with the PKA randomly selected near the GB. (h–l) The dissolution of accumulated clusters and absorption by the migrating GB. The arrow indicates the vacancy position. V denotes the mono-vacancy. The dashed circle sketches out the vacancy clusters. The axes X , Y and Z are along $[310]$, $[\bar{1}30]$ and $[001]$, respectively. The atoms within the GB are colored with their potential energies, while the defects near the GB are red.



Defects accumulation (bulk, GB):

$F[\text{Radiation condition}(T, \text{dose}, \text{dose rate}),$

$P_{\text{bulk}}(V, \text{SIA}), P_{\text{nearGB}}(V, \text{SIA}, \text{GB structure}),$

$P_{\text{atGB}}(V, \text{SIA}, \text{GB structure}), P_{\text{GB}}(\text{GB structure}), L]$

Fig. S3. Schematic illustration of the factors determining the radiation damage accumulation in the bulk/GB region of a nano-crystal. These factors include radiation conditions of temperature (T), radiation dose (rd), radiation dose rate (τ), and the grain size (L). The atomic processes in the NC system include the processes in the bulk represented by $P_{\text{bulk}}(V, \text{SIA})$, the processes near the GB denoted by $P_{\text{nearGB}}(V, \text{SIA})$, the processes within the GB represented by $P_{\text{atGB}}(V, \text{SIA})$, the process associated with GB structural relaxation denoted by $P_{\text{GB}}(\text{GB structure})$. The GB region is separated from the bulk region by two horizontal dash red lines. The GB plane is indicated by a horizontal red line.

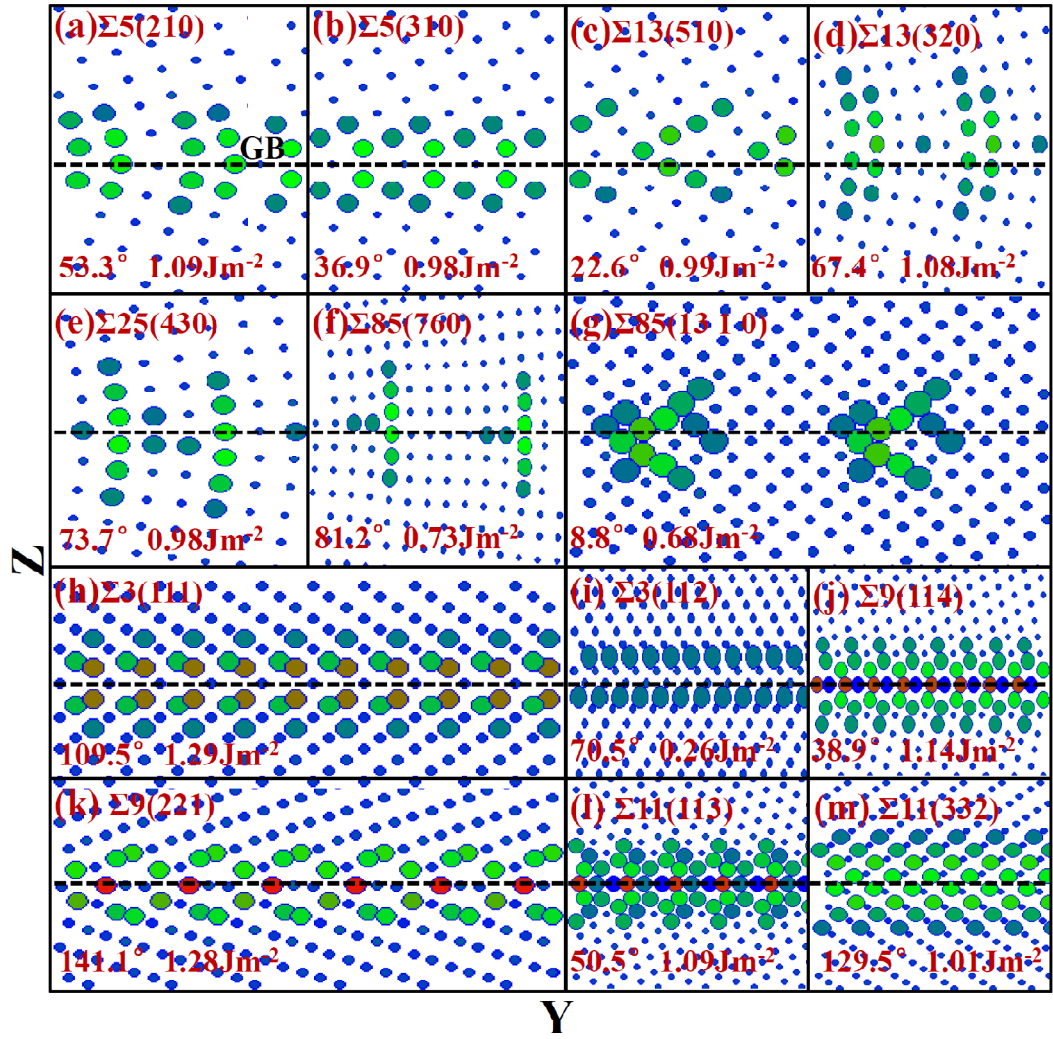


Fig. S4. The relaxed structures for the investigated thirteen tilt symmetric GBs. The atoms are colored with their potential energies. (a–g) are for the GBs with tilt axis of $[0\ 0\ 1]$, while (h–m) show the GBs with the tilt axis of $[1\ 1\ 0]$. In (a–m), axis Z is along $[2\ 1\ 0]$, $[3\ 1\ 0]$, $[5\ 1\ 0]$, $[3\ 2\ 0]$, $[4\ 3\ 0]$, $[7\ 6\ 0]$, $[13\ 1\ 0]$, $[1\ 1\ 1]$, $[1\ 1\ 2]$, $[1\ 1\ 4]$, $[2\ 2\ 1]$, $[1\ 1\ 3]$, and $[3\ 3\ 2]$, respectively. And axis Y is along $[1\ \bar{2}\ 0]$, $[1\ \bar{3}\ 0]$, $[1\ \bar{5}\ 0]$, $[2\ \bar{3}\ 0]$, $[3\ \bar{4}\ 0]$, $[6\ \bar{7}\ 0]$, $[1\ \bar{13}\ 0]$, respectively in (a–g). In (h–m), Y is along $[1\ \bar{1}\ 0]$. In each figure, the tilt angle and the GB energy are marked. The horizontal dash line indicates the GB position.

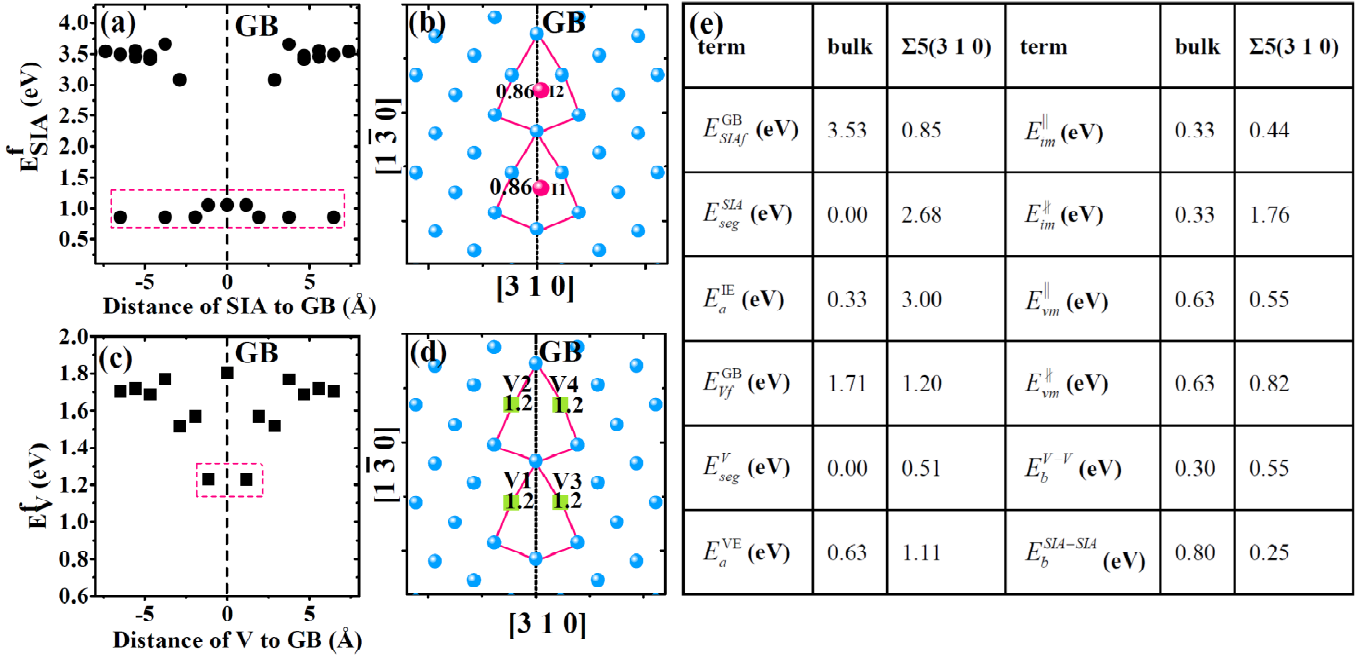


Fig. S5. (a) SIA formation energy (E_{SIA}^f) profile near the GB of $\Sigma 5(3\ 1\ 0)/[0\ 0\ 1]$ as a function of the distance of the initial SIA center to the GB. (b) SIA configuration within a GB structural unit, as labeled by symbols *I1* and *I2*. A SIA is denoted by a red sphere. The E_{SIA}^f is marked near the SIA. (c) V formation energy (E_V^f) profile near the GB as a function of the V distance to the GB. (d) V configuration within a GB structural unit. A V is represented by a green square. V1, V2, V3 and V4 denote the four V occupation sites. E_V^f is marked near the V. In (a–d), the dash black line indicates the GB position. In (b) and (d), the polygon indicates the GB structural unit. (e) Fundamental parameters characterizing the SIA/V behavior near the GB, including SIA formation energy at the GB (E_{SIAf}^{GB}), SIA segregation energy (E_{seg}^{SIA}), SIA emission energy barrier from a pure GB (E_a^{IE}), V formation energy at the GB (E_{vf}^{GB}), V segregation energy (E_{seg}^V), V emission energy barrier from a pure GB (E_a^{VE}), the migration energy barrier for the SIA along the tilt axis (E_{im}^{\parallel}), the SIA migration energy barrier in the direction nonparallel to the tilt axis ($E_{im}^{\#}$), the migration energy barrier for the V along the tilt axis (E_{vm}^{\parallel}), the V migration energy barrier in the direction nonparallel to the tilt axis ($E_{vm}^{\#}$), binding energy of the V-V (E_b^{V-V}) and SIA-SIA ($E_b^{SIA-SIA}$) at the GB. The values for the corresponding parameter in the bulk are also given for comparison.

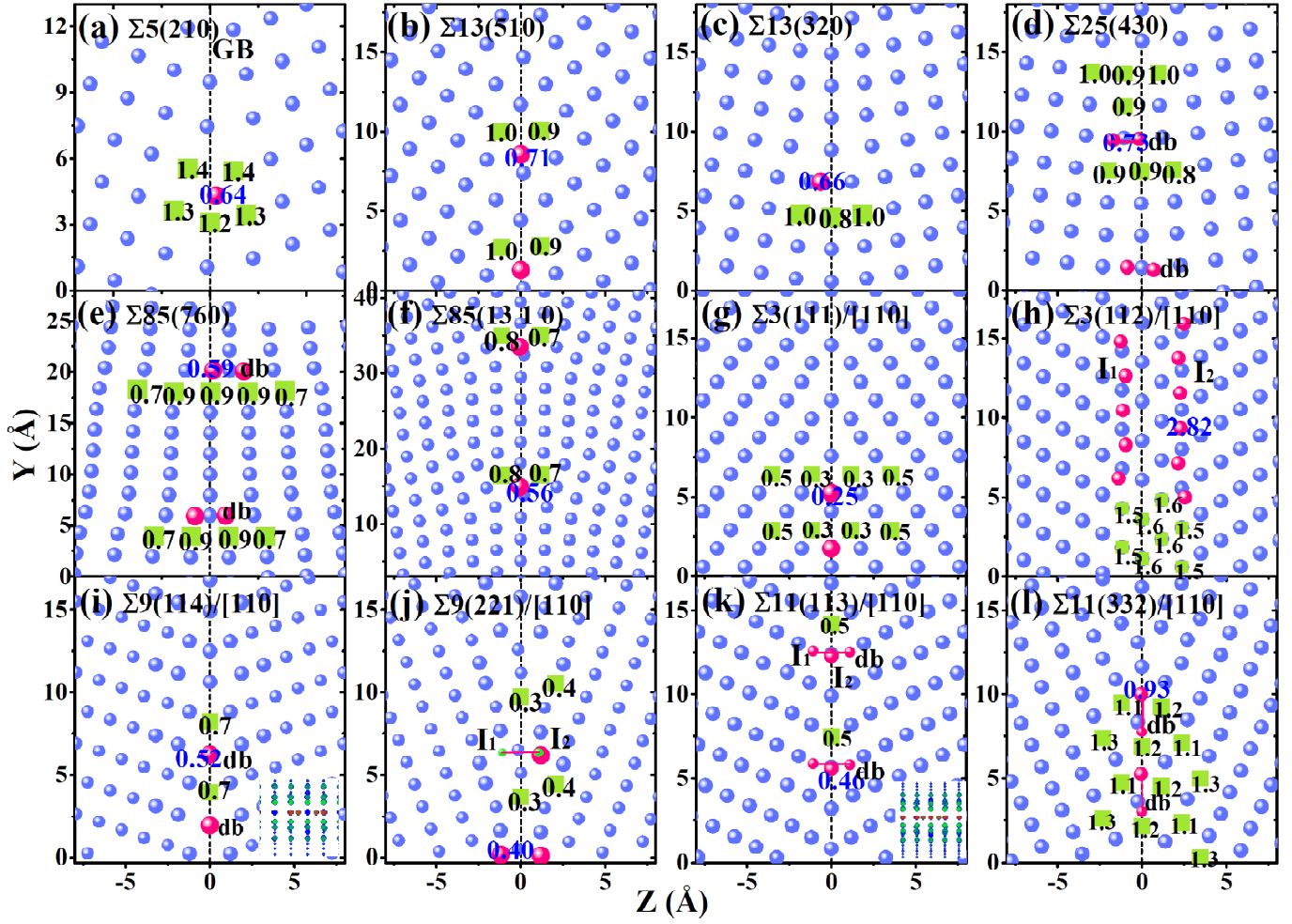


Fig. S6. (a–j) The V/SIA configurations at several GBs. A V is shown by a green square; a SIA is represented by red spheres, the number of which depends on the SIA configuration at the GB. For the V, the metastable site is also shown with V formation energy above the minimal E_V^f less than 0.2 eV. The E_V^f is marked on a site. E_{SIA}^f is marked near the SIA configuration. The vertical blue line indicates the GB position.

In (i) and (k), the inset shows the SIA configuration along another view. Axis Z is normal to the GB plane, while axis Y is parallel to the GB plane. Axes Y and Z are identical to that in Fig. S4.

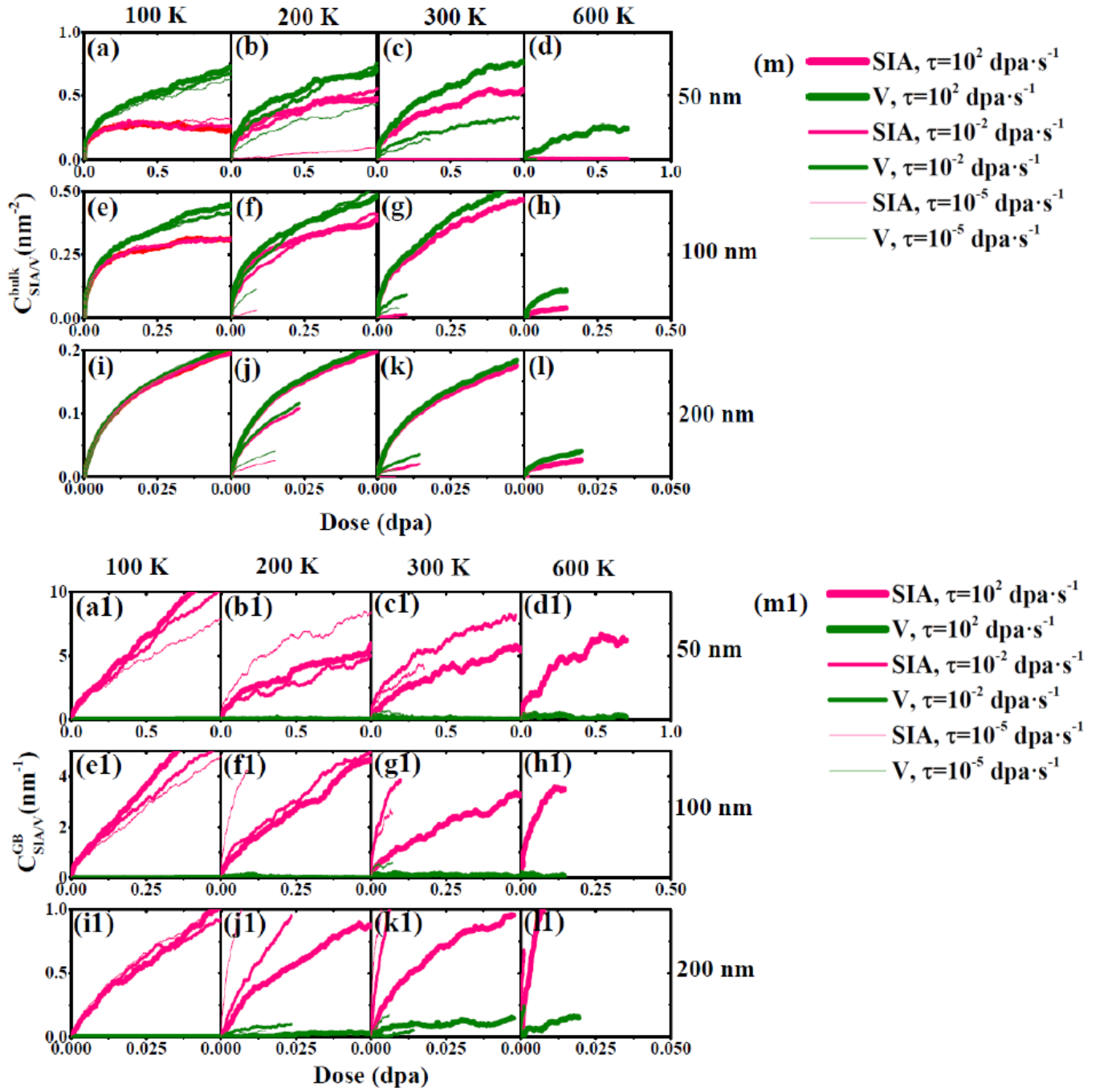


Fig. S7. (a–l) The bulk SIA/V concentration ($C_{SIA/V}^{bulk}$) as a function of the radiation dose at different temperatures of 100, 200, 300 and 600 K and grain sizes of 50, 100 and 200 nm. (a1–l1) The SIA/V concentration at the GB ($C_{SIA/V}^{GB}$) as a function of the radiation dose at the above four temperatures and grain sizes. The legend for (a–l) is given in (m). The legend for (a1–l1) is given in (m1).

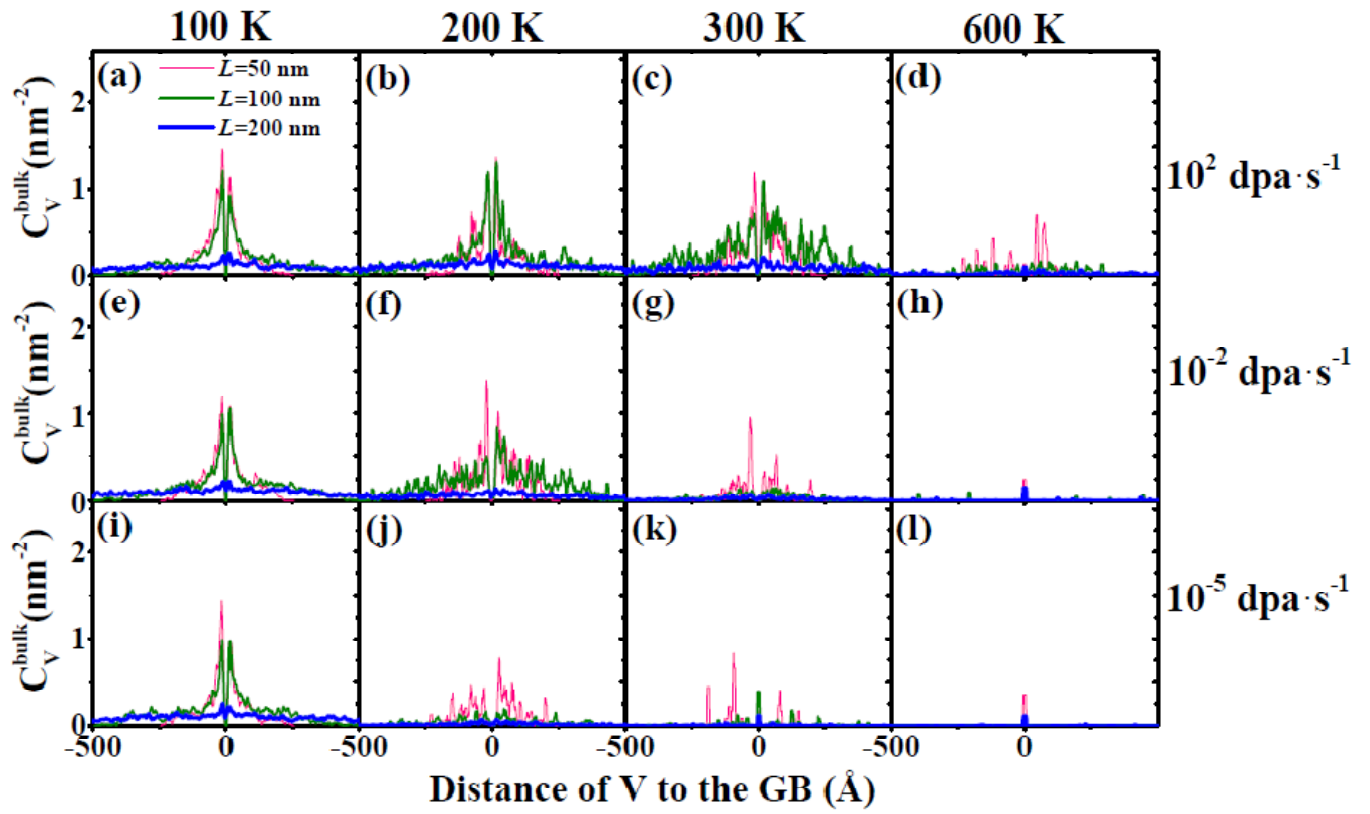


Fig. S8. (a–l) The bulk V concentration as a function of the distance of the V to the GB at different temperatures of 100, 200, 300 and 600 K and dose rates of 10^2 , 10^{-2} and 10^{-5} dpa·s $^{-1}$. The legend for (a–l) is given in (a).

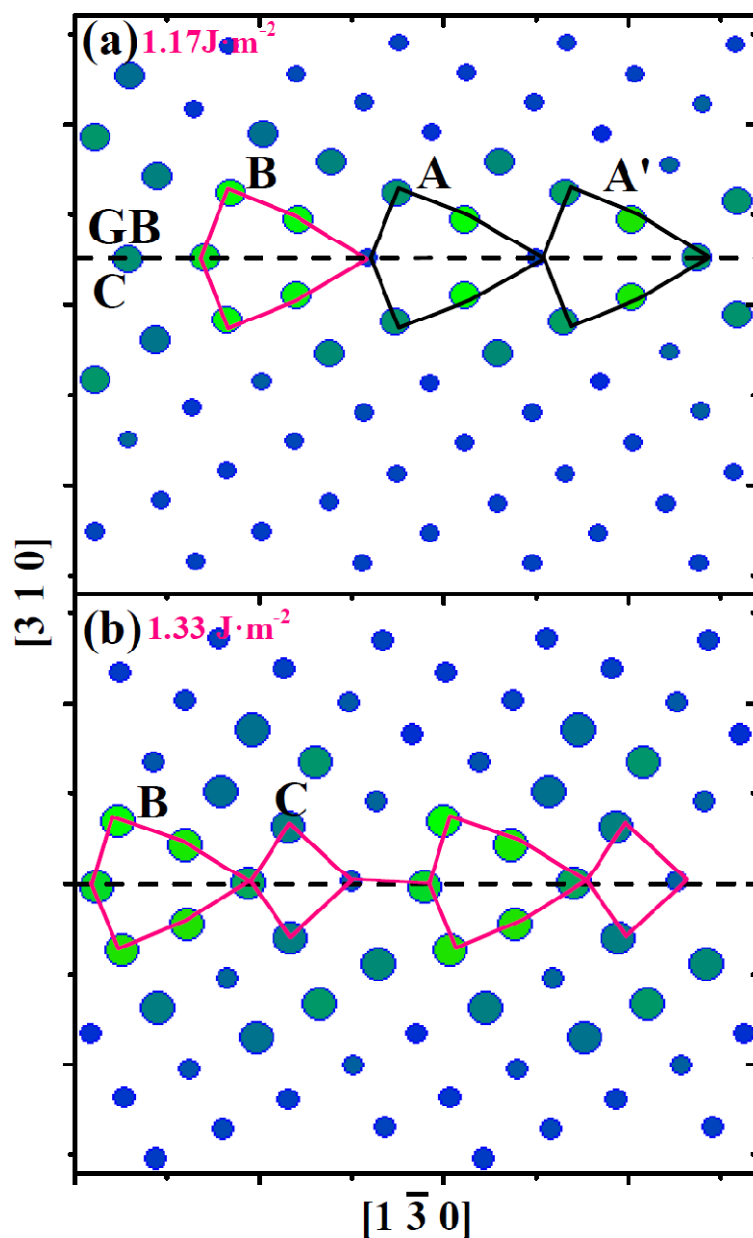


Fig. S9. The relaxed GB structures of $\Sigma 5(3\ 1\ 0)/[0\ 0\ 1]$ with a certain concentration of SIA at 300 K for 50 ps. In (a) and (b), the horizontal black line indicates the GB position. The polygon indicates the GB structural unit. The atom is represented by a sphere colored by the potential energy of the atom.

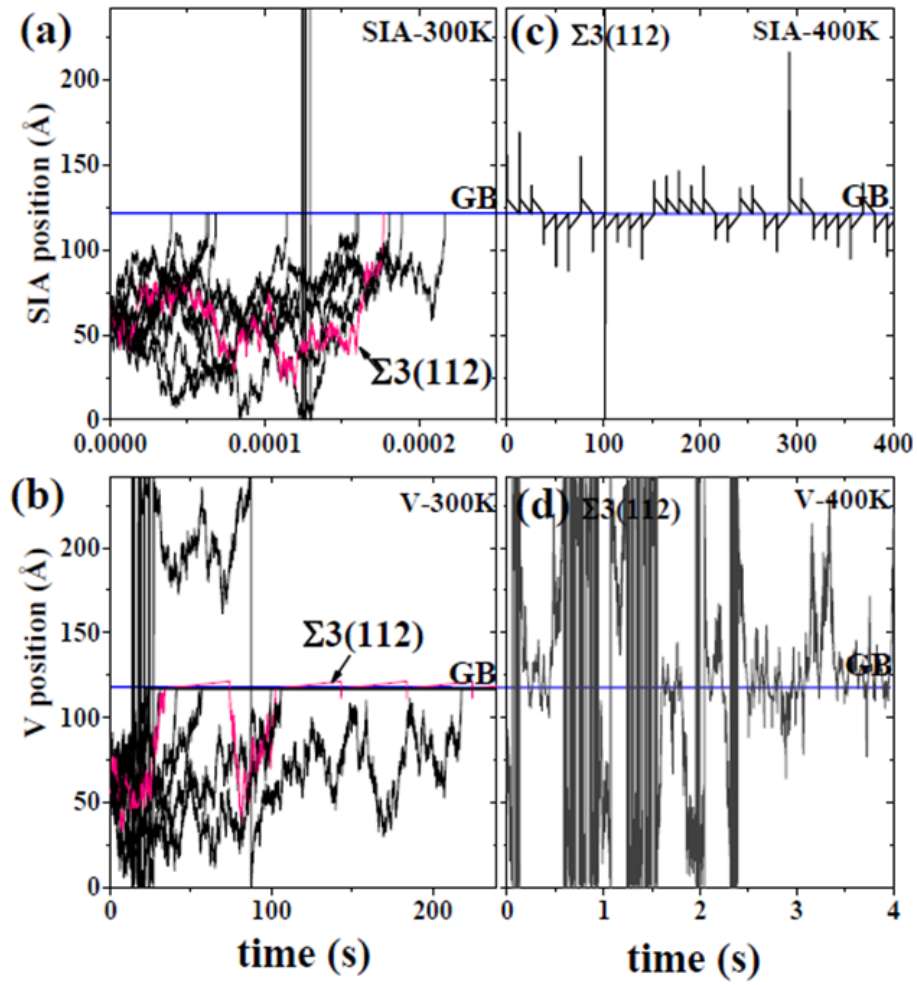


Fig. S10. (a) The trajectories of a SIA near all the eleven GBs at 300 K drawn from object kinetic Monte Carlo (OKMC) simulations of the SIA behavior near the GB. Initially, the SIA is about 6 nm away from the GBs. The red curve is for $\Sigma 3(112)/[110]$. The horizontal blue line indicates the GB position. (b) The trajectories of a V near all the GBs at 300 K. (c) and (d) shows the trajectories at 400 K for a SIA and V, respectively.

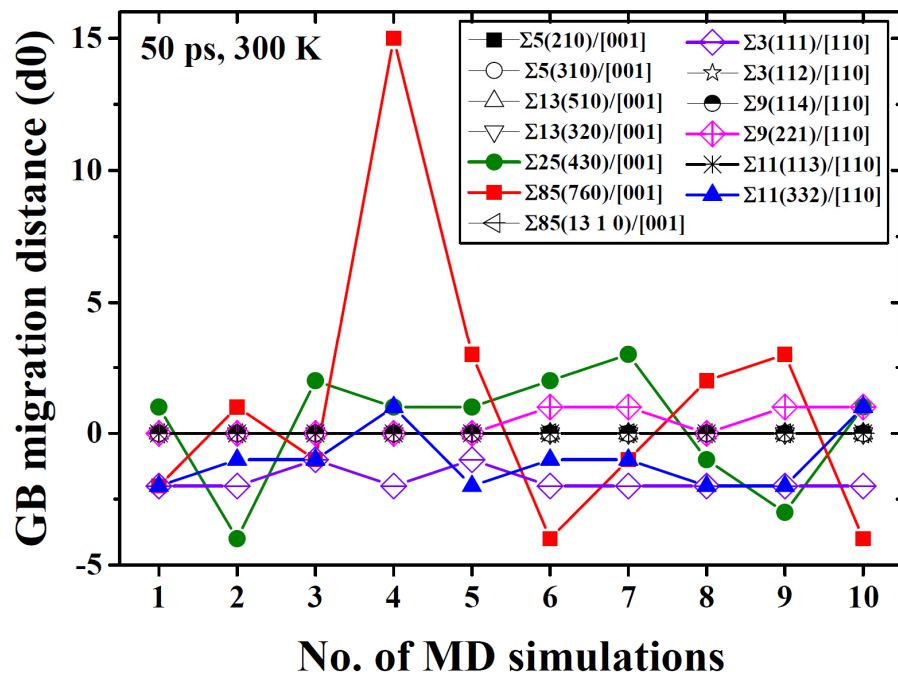


Fig. S11. The GB migration distance within 50 ps at 300 K in several distinct MD simulations, which is in unit of the distance that the GB moves from one stable state to another nearest one (d0).

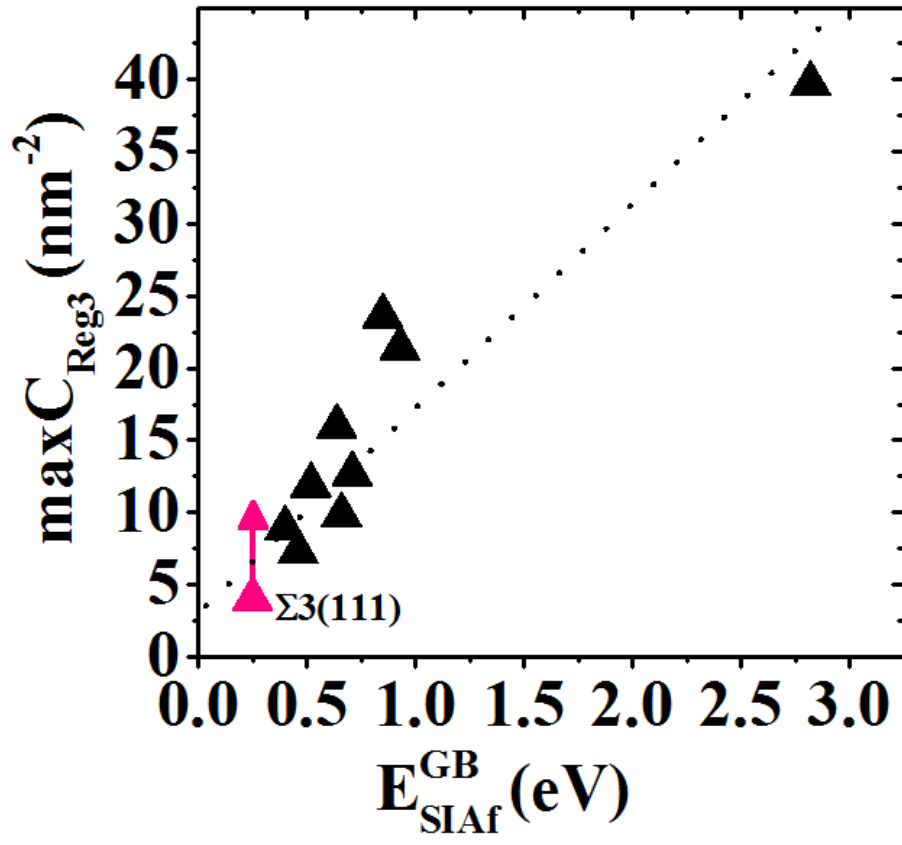


Fig. S12. The relation of the $C_{\text{Reg}3}$ to the formation energy of a single SIA at a pure GB ($E_{\text{SIAf}}^{\text{GB}}$).

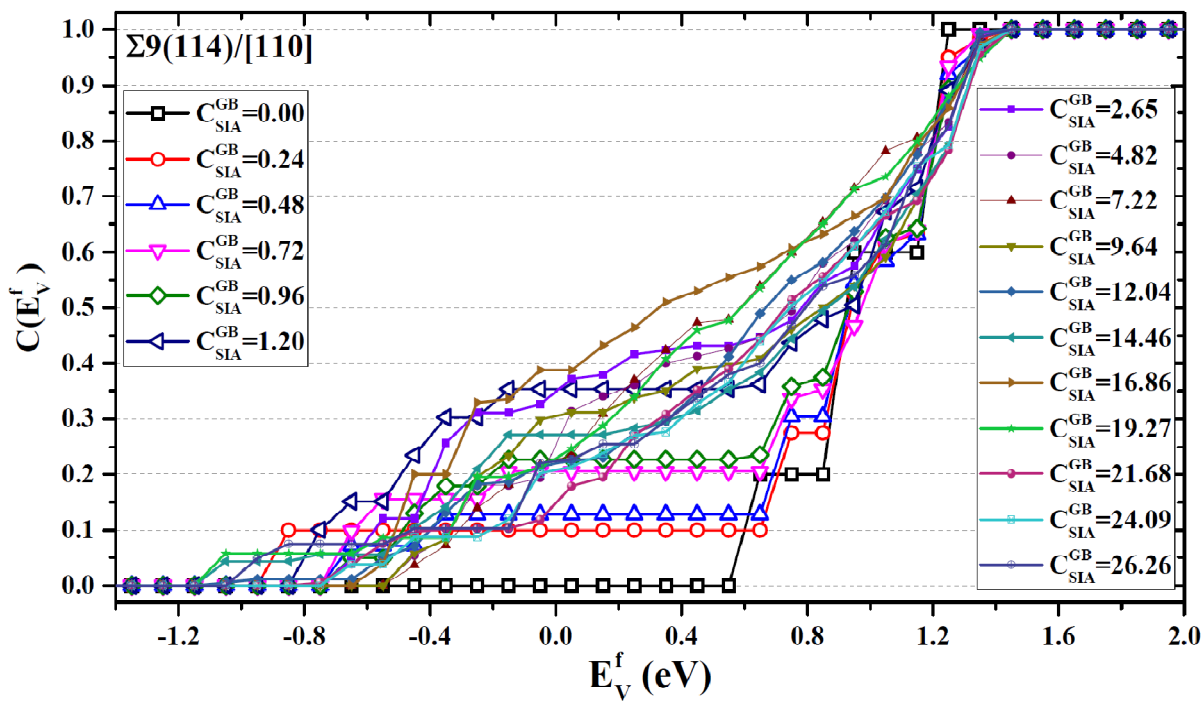


Fig. S13. Cumulative distribution function $C(E_V^f)$ in the GB $\Sigma 9(114)/[110]$ loaded with different concentration levels of the SIAs.

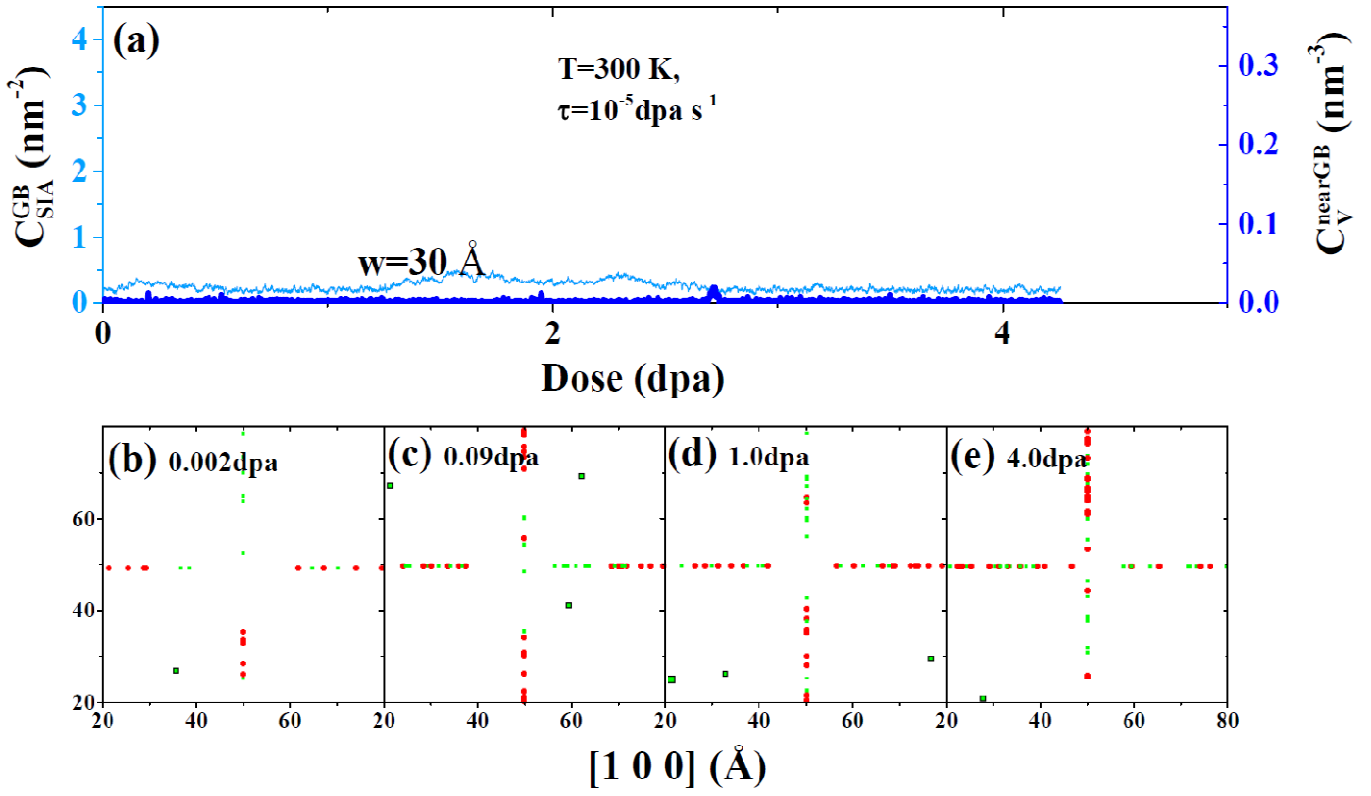


Fig. S14. (a) Variation in C_{SIA}^{GB} (the left axis) and the corresponding V concentration near the GB (C_V^{nearGB}) (the right axis) with radiation dose at a temperature (T) of 300 K and dose rate (τ) of $10^{-5}\text{ dpa}\cdot\text{s}^{-1}$. (b–e) Snapshots for microstructure evolution at above T , τ condition. In this visualization scheme, a V-cluster is displayed by a red square, while a SIA-clusters is shown by a red filled circle. The radius of the square/circle is proportional to the real size of the V/SIA-cluster.

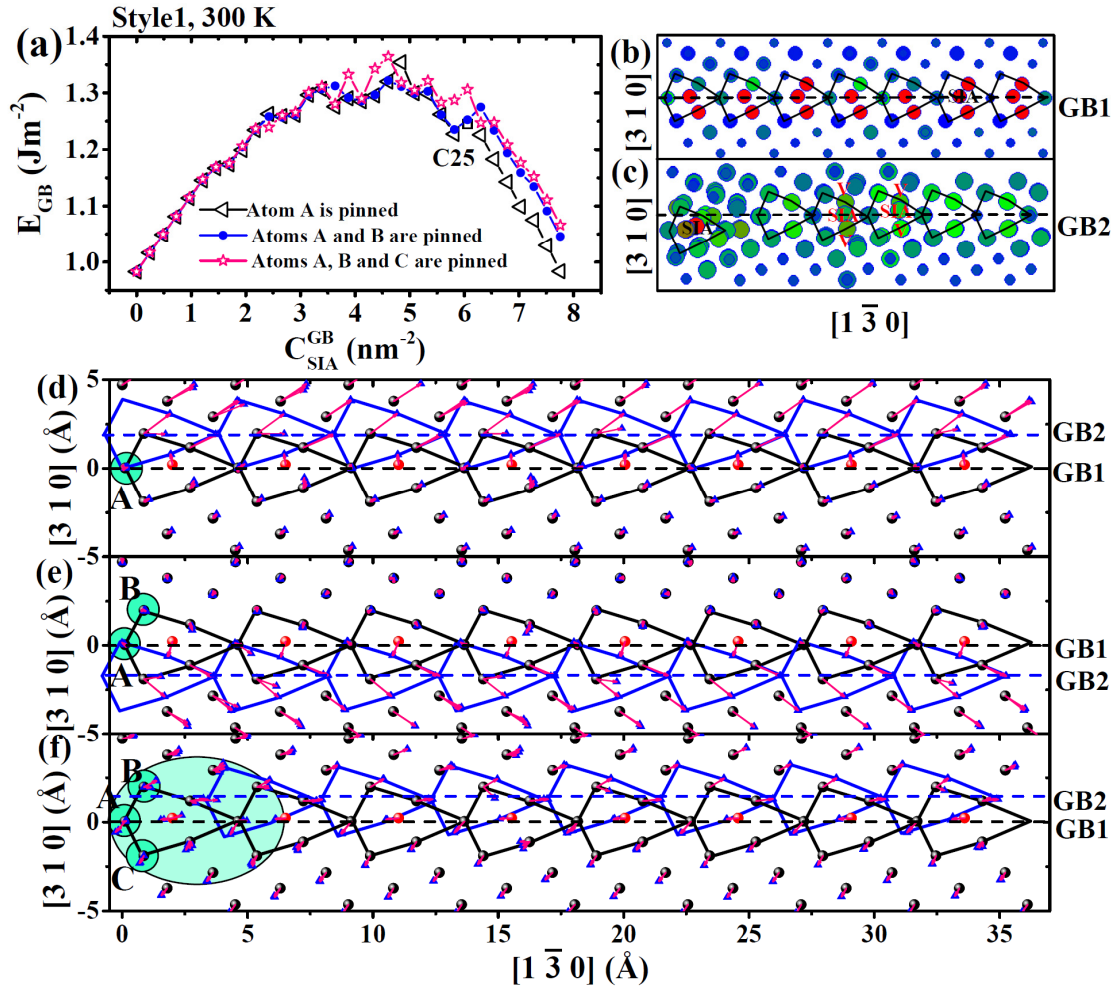


Fig. S15. (a) GB energy (E_{GB}) as a function of the SIA concentration at the GB of $\Sigma 5(3\ 1\ 0)/[0\ 0\ 1]$ (C_{SIA}^{GB}). (b) and (c) The initial structure of the GB with a certain concentration of SIAs and the GB structure after relaxation at 300 K, respectively. Three atoms near the GB were pinned during the relaxation. The atoms are colored with their potential energies, using the same visualization scheme as that in Fig. 4(c–h). (d–f) The GB relaxation process. A, B and C mark the pinned atoms during the structural relaxation. In (f), the atoms that nearly remain immobile are covered by the light green circle. In (d–f), the black and blue horizontal line indicates the GB position before and after relaxation, respectively.

2. Supplementary tables

Table S1. Irradiation conditions in several systems.

Reference	System	Radiation-particle	T (K)	rd (dpa)	τ (dpa·s ⁻¹)	L (nm)
[S4]	Pd	4MeV-Kr ²⁺	298	170-210	3×10^{-1}	10-300
[S4]	ZrO ₂	4MeV-Kr ²⁺	298	3-8	9×10^{-4}	10-300
[S5]	Pt	2.8MeV-Au ⁴⁺	573	3	8×10^{-4}	20-100
[S6]	Ag	1MeV-Kr ²⁺	298	1	1.25×10^{-3}	100
[S7]	Ni	1MeV-Kr ²⁺	298	1-5	3×10^{-3}	200
[S8]	Au	60MeV- ¹² C	15	unknown	unknown	23
[S8]	Au	60MeV- ¹² C	300	unknown	unknown	23
[S9]	bcc-Fe	100keV-He ²⁺	298	6	8×10^{-4}	49-96
[S10]	bcc-Fe	10keV-He ²⁺	700	12.5	1×10^{-2}	100
[S11]	bcc-Fe	10keV-He ²⁺	298	2	1×10^{-2}	50
[S11]	bcc-Fe	10keV-He ²⁺	873	2	1×10^{-2}	50
[S12]	bcc-Fe	440keV-He ²⁺	823	2	4×10^{-6}	12.6
[S13]	bcc-Fe	3.5MeV-Fe ⁺	723	150	1×10^{-2}	320
[S13]	bcc-Fe	3.5MeV-Fe ⁺	723	150	1×10^{-2}	2000
[S14]	fcc-Fe	1MeV-Kr ²⁺	723	40	2.5×10^{-3}	45
[S14]	fcc-Fe	1MeV-Kr ²⁺	873	108	2.5×10^{-3}	45
[S15]	fcc-Fe	3.5MeV-Fe ⁺	773	80	3×10^{-3}	100
[S15]	fcc-Fe	3.5MeV-Fe ⁺	773	80	3×10^{-3}	35000
[S16]	Cu	4.5MeV-Cu ³⁺	298	1.7/8.5	unknown	280
[S17]	Cu	1MeV-Kr ²⁺	298	1.56	$0.43-1.98\times 10^{-3}$	unknown
[S18]	Cu	200keV-He ²⁺	723	3	2.8×10^{-4}	15
[S19]	Mo	200keV-He ²⁺	298	4	unknown	25-3900
[S20]	W	8keV-He ²⁺	298	unknown	unknown	40-300
[S21]	W	3MeV-Si ²⁺ /Cu ³⁺ /W ⁴⁺	298	1.03-5.72	$6\times 10^{-4}/9\times 10^{-4}/3\times 10^{-3}$	60-400
[S22]	W	3MeV-Cu ³⁺	298/1050	0.2-4	1×10^{-4}	50.6-800
[S22]	W	3MeV-Cu ³⁺	298/1050	0.2-4	1×10^{-2}	50.6-800
[S23]	W	2keV-He ²⁺	1223	unknown	unknown	60-100,100-500
[S24]	W	1MeV-Kr ²⁺	298/1073	2	2×10^{-3}	35,85,80-400,1-3000

Table S2. The migration energy barriers for small V_n/SIA_n in the bulk and near the GB.

Value	Term	Comments
0.67 eV	Em_V_bulk	Migration energy barrier for a single V in Fe bulk
0.62 eV	Em_V2_bulk	Migration energy barrier for V_2 in Fe bulk
0.35 eV	Em_V3_bulk	Migration energy barrier for V_3 in Fe bulk
0.48 eV	Em_V4_bulk	Migration energy barrier for V_4 in Fe bulk
2.8 eV	Em_Vn_bulk	Migration energy barrier for V_n ($n>4$) in Fe bulk
0.34 eV	Em_SIA_bulk	Migration energy barrier for a single SIA in Fe bulk
0.43 eV	Em_SIA2_bulk	Migration energy barrier for SIA_2 in Fe bulk
0.43 eV	Em_SIA3_bulk	Migration energy barrier for SIA_3 in Fe bulk
0.43 eV	Em_SIA _{n1} _bulk	Migration energy barrier for SIA_{n1} ($n1>3$, $n1\leq 10$) in Fe bulk
2.8 eV	Em_SIA _{n2} _bulk	Migration energy barrier for SIA_{n2} ($n2>10$) in Fe bulk
0.0 eV	Em_SIA _n _nearGB	Migration energy barrier for SIA_n ($n\leq 500$) near Fe GB
0.34 eV	Em_V_nearGB	Migration energy barrier for a single V near Fe GB
0.31 eV	Em_V2_nearGB	Migration energy barrier for V_2 near Fe GB
0.18 eV	Em_V3_nearGB	Migration energy barrier for V_3 near Fe GB
0.24 eV	Em_V4_nearGB	Migration energy barrier for V_4 near Fe GB
1.4 eV	Em_Vn_nearGB	Migration energy barrier for V_n ($n>4$) near Fe GB

Table S3. Some parameters describing the SIA migration along the GB, including migration energy barrier for the SIA along the tilt axis (E_{im}^{\parallel}), the time for SIA migration along the tilt axis at 300 K (t_{im}^{\parallel}), the SIA migration energy barrier in the direction nonparallel to the tilt axis ($E_{im}^{\#}$), the time for the SIA migration in the corresponding direction at 300 K ($t_{im}^{\#}$).

GB	E_{im}^{\parallel} (eV)	t_{im}^{\parallel} (s)	$E_{im}^{\#}$ (eV)	$t_{im}^{\#}$ (s)
bulk	0.33	3.5×10^{-7}	0.33	3.5×10^{-7}
$\Sigma 5(2\ 1\ 0)/[0\ 0\ 1]$	0.12	1.0×10^{-10}	1.52	3.4×10^{13}
$\Sigma 5(3\ 1\ 0)/[0\ 0\ 1]$	0.44	2.5×10^{-5}	1.176	5.7×10^7
$\Sigma 13(5\ 1\ 0)/[0\ 0\ 1]$	0.49	1.7×10^{-4}	3.06	2.6×10^{39}
$\Sigma 13(3\ 2\ 0)/[0\ 0\ 1]$	0.04	4.7×10^{-12}	3.05	1.7×10^{39}
$\Sigma 25(4\ 3\ 0)/[0\ 0\ 1]$	0.52	5.4×10^{-4}	1.80	1.7×10^{18}
$\Sigma 85(7\ 6\ 0)/[0\ 0\ 1]$	0.77	8.6	1.7	3.6×10^{16}
$\Sigma 85(13\ 1\ 0)/[0\ 0\ 1]$	0.34	5.2×10^{-7}	2.0	4.0×10^{21}
$\Sigma 3(1\ 1\ 1)/[1\ 1\ 0]$	0.69	3.9×10^{-1}	0.50	2.5×10^{-4}
$\Sigma 3(1\ 1\ 2)/[1\ 1\ 0]$	0.55	1.7×10^{-3}	0.07	1.5×10^{-11}
$\Sigma 9(1\ 1\ 4)/[1\ 1\ 0]$	0.45	3.6×10^{-5}	1.04	3.0×10^5
$\Sigma 9(2\ 2\ 1)/[1\ 1\ 0]$	0.53	8.0×10^{-4}	0.82	6.0×10^1
$\Sigma 11(1\ 1\ 3)/[1\ 1\ 0]$	0.66	1.2×10^{-1}	1.22	3.1×10^8
$\Sigma 11(3\ 3\ 2)/[1\ 1\ 0]$	0.87	4.1×10^2	0.99	4.3×10^4

Table S4. Some parameters describing the V migration along the GB, including migration energy barrier for the V along the tilt axis (E_{vm}^{\parallel}), the time for V migration along the tilt axis at 300 K (t_{vm}^{\parallel}), the V migration energy barrier in the direction nonparallel to the tilt axis ($E_{vm}^{\#}$), the time for the V migration in the corresponding direction at 300 K ($t_{vm}^{\#}$).

GB	E_{vm}^{\parallel} (eV)	t_{vm}^{\parallel} (s)	$E_{vm}^{\#}$ (eV)	$t_{vm}^{\#}$ (s)
bulk	0.63	3.8×10^{-2}	0.63	3.8×10^{-2}
$\Sigma 5(2\ 1\ 0)/[0\ 0\ 1]$	0.36	1.1×10^{-6}	1.07	9.5×10^5
$\Sigma 5(3\ 1\ 0)/[0\ 0\ 1]$	0.55	1.7×10^{-3}	0.82	6.0×10^1
$\Sigma 13(5\ 1\ 0)/[0\ 0\ 1]$	0.68	2.7×10^{-1}	1.46	3.4×10^{12}
$\Sigma 13(3\ 2\ 0)/[0\ 0\ 1]$	0.37	1.6×10^{-6}	1.61	1.1×10^{15}
$\Sigma 25(4\ 3\ 0)/[0\ 0\ 1]$	0.72	1.2×10^1	1.28	3.2×10^9
$\Sigma 85(7\ 6\ 0)/[0\ 0\ 1]$	0.78	1.3×10^1	1.4	3.3×10^{11}
$\Sigma 85(13\ 1\ 0)/[0\ 0\ 1]$	0.89	9.0×10^2	1.73	1.2×10^{17}
$\Sigma 3(1\ 1\ 1)/[1\ 1\ 0]$	0.95	9.1×10^3	0.95	9.1×10^3
$\Sigma 3(1\ 1\ 2)/[1\ 1\ 0]$	0.60	1.2×10^{-2}	0.38	2.4×10^{-6}
$\Sigma 9(1\ 1\ 4)/[1\ 1\ 0]$	0.68	2.7×10^{-1}	1.75	2.5×10^{17}
$\Sigma 9(2\ 2\ 1)/[1\ 1\ 0]$	1.25	1.0×10^9	1.73	1.2×10^{17}
$\Sigma 11(1\ 1\ 3)/[1\ 1\ 0]$	0.79	1.9×10^1	2.18	4.2×10^{24}
$\Sigma 11(3\ 3\ 2)/[1\ 1\ 0]$	0.66	1.2×10^{-1}	0.56	2.6×10^{-3}

Table S5. The binding energy for the V/SIA with small V_n/SIA_n in Fe bulk.

Value	Term	Comments
0.30 eV	Eb_V_V_bulk	Binding energy for the V with a V in Fe bulk
0.37 eV	Eb_V_V2_bulk	Binding energy for the V with a V2 in Fe bulk
0.62 eV	Eb_V_V3_bulk	Binding energy for the V with a V3 in Fe bulk
0.62 eV	Eb_V_Vn_bulk	Binding energy for the V with a Vn (n>3) in Fe bulk
0.80 eV	Eb_SIA_SIA_bulk	Binding energy for the SIA with a SIA in Fe bulk
0.92 eV	Eb_SIA_SIA2_bulk	Binding energy for the SIA with a SIA2 in Fe bulk
1.64 eV	Eb_SIA_SIA3_bulk	Binding energy for the SIA with a SIA3 in Fe bulk
1.64 eV	Eb_SIA_SIA _n _bulk	Binding energy for the SIA with a SIA _n (n>3) in Fe bulk

Table S6. Binding energy of the V-V (E_b^{V-V}) and SIA-SIA ($E_b^{SIA-SIA}$) at the GB. Note that, before calculating the binding energy, the stable sites for V/V₂ and SIA/SIA₂ at the GB were found by relaxing the corresponding GB system at 300 K.

GB	E_b^{V-V} (eV)	$E_b^{SIA-SIA}$ (eV)
bulk	0.30	0.80
$\Sigma 5(2\ 1\ 0)/[0\ 0\ 1]$	0.44	-0.27
$\Sigma 5(3\ 1\ 0)/[0\ 0\ 1]$	0.55	0.25
$\Sigma 13(5\ 1\ 0)/[0\ 0\ 1]$	0.42	0.38
$\Sigma 13(3\ 2\ 0)/[0\ 0\ 1]$	0.52	-0.06
$\Sigma 25(4\ 3\ 0)/[0\ 0\ 1]$	0.63	0.42
$\Sigma 85(7\ 6\ 0)/[0\ 0\ 1]$	0.57	0.40
$\Sigma 85(13\ 1\ 0)/[0\ 0\ 1]$	0.53	0.19
$\Sigma 3(1\ 1\ 1)/[1\ 1\ 0]$	-1.09	0.02
$\Sigma 3(1\ 1\ 2)/[1\ 1\ 0]$	0.1	0.48
$\Sigma 9(1\ 1\ 4)/[1\ 1\ 0]$	0.15	-0.23
$\Sigma 9(2\ 2\ 1)/[1\ 1\ 0]$	-0.25	0.09
$\Sigma 11(1\ 1\ 3)/[1\ 1\ 0]$	-0.08	-0.04
$\Sigma 11(3\ 3\ 2)/[1\ 1\ 0]$	0.44	0.07

Table S7. Some parameters describing the interaction of a SIA with a GB, including the minimal SIA formation energy (E_{SIAf}^{GB}) near the GB, the maximal SIA segregation energy (E_{seg}^{SIA}), the maximal SIA emission energy barrier from the GB (E_a^{IE}), the time for SIA emission from the GB at 300 K (t_{IE}), the minimal di-SIA formation energy near the GB ($E_{SIA_2f}^{GB}$). Note that, the GB with a SIA or di-SIA was relaxed at 300 K to find the stable site for the SIA/SIA₂ location at the GB.

GB	E_{SIAf}^{GB} (eV)	E_{seg}^{SIA} (eV)	E_a^{IE} (eV)	t_{IE} (s)	$E_{SIA_2f}^{GB}$ (eV)
bulk	3.53	0.00	0.33	3.5×10^{-7}	
$\Sigma 5(2\ 1\ 0)/[0\ 0\ 1]$	0.64	2.89	3.22	1.3×10^{42}	1.55
$\Sigma 5(3\ 1\ 0)/[0\ 0\ 1]$	0.85	2.68	3.00	2.9×10^{38}	1.45
$\Sigma 13(5\ 1\ 0)/[0\ 0\ 1]$	0.71	2.82	3.15	8.8×10^{40}	1.04
$\Sigma 13(3\ 2\ 0)/[0\ 0\ 1]$	0.66	2.87	3.20	6.1×10^{41}	1.38
$\Sigma 25(4\ 3\ 0)/[0\ 0\ 1]$	0.73	2.80	3.13	3.5×10^{40}	1.04
$\Sigma 85(7\ 6\ 0)/[0\ 0\ 1]$	0.59	2.94	3.27	5.8×10^{41}	0.78
$\Sigma 85(13\ 1\ 0)/[0\ 0\ 1]$	0.56	2.97	3.30	2.5×10^{43}	0.93
$\Sigma 3(1\ 1\ 1)/[1\ 1\ 0]$	0.25	3.28	3.61	3.9×10^{48}	0.48
$\Sigma 3(1\ 1\ 2)/[1\ 1\ 0]$	2.82	0.71	1.04	2.8×10^5	5.16
$\Sigma 9(1\ 1\ 4)/[1\ 1\ 0]$	0.52	3.01	3.34	1.3×10^{44}	1.27
$\Sigma 9(2\ 2\ 1)/[1\ 1\ 0]$	0.40	3.13	3.50	1.3×10^{46}	0.71
$\Sigma 11(1\ 1\ 3)/[1\ 1\ 0]$	0.46	3.07	3.40	1.4×10^{45}	0.96
$\Sigma 11(3\ 3\ 2)/[1\ 1\ 0]$	0.93	2.60	2.93	1.5×10^{37}	1.79

Table S8. Some parameters describing the interaction of a V with a GB, including the minimal vacancy formation energy ($E_{V_f}^{GB}$) near the GB, the maximal V segregation energy (E_{seg}^V), the maximal V emission energy barrier from the GB (E_a^{VE}), the time for V emission from the GB at 300 K (t_{VE}), the minimal di-V formation energy near the GB ($E_{V_2f}^{GB}$). Note that, the GB with a V or di-V was relaxed at 300 K to find the stable site for the V/V₂ location at the GB.

GB	$E_{V_f}^{GB}$ (eV)	E_{seg}^V (eV)	E_a^{VE} (eV)	t_{VE} (s)	$E_{V_2f}^{GB}$ (eV)
bulk	1.71	0.00	0.63	3.8×10^{-2}	
$\Sigma 5(2\ 1\ 0)/[0\ 0\ 1]$	1.22	0.49	1.12	5.6×10^6	2.00
$\Sigma 5(3\ 1\ 0)/[0\ 0\ 1]$	1.20	0.51	1.11	3.8×10^6	1.85
$\Sigma 13(5\ 1\ 0)/[0\ 0\ 1]$	0.85	0.86	1.49	9.3×10^{12}	1.28
$\Sigma 13(3\ 2\ 0)/[0\ 0\ 1]$	0.80	0.91	1.54	8.2×10^{13}	1.08
$\Sigma 25(4\ 3\ 0)/[0\ 0\ 1]$	0.78	0.93	1.56	1.7×10^{14}	0.93
$\Sigma 85(7\ 6\ 0)/[0\ 0\ 1]$	0.66	1.05	1.34	3.3×10^{10}	0.75
$\Sigma 85(13\ 1\ 0)/[0\ 0\ 1]$	0.71	1.00	1.63	2.6×10^{15}	0.89
$\Sigma 3(1\ 1\ 1)/[1\ 1\ 0]$	0.35	1.37	1.99	3.2×10^{21}	1.79
$\Sigma 3(1\ 1\ 2)/[1\ 1\ 0]$	1.53	0.18	0.81	3.8×10^1	2.96
$\Sigma 9(1\ 1\ 4)/[1\ 1\ 0]$	0.70	1.01	1.62	1.9×10^{15}	1.25
$\Sigma 9(2\ 2\ 1)/[1\ 1\ 0]$	0.34	1.37	2.00	3.3×10^{21}	0.93
$\Sigma 11(1\ 1\ 3)/[1\ 1\ 0]$	0.55	1.16	1.79	1.3×10^{18}	1.18
$\Sigma 11(3\ 3\ 2)/[1\ 1\ 0]$	1.14	0.57	1.20	1.6×10^8	1.84

3. Supplementary text

Text S1. Derivation for the linear increase of the GB energy with the defects concentration at the GB.

The meaning of the relevant symbols is defined as follows. S_{GB} : the area of a GB, N : the number of atoms in a GB system, E_{coh} : cohesive energy per atom in the bulk, n : the number V/SIA at the GB, E_{GB}^{tot} : the total energy of a GB system, C : the V/SIA concentration at the GB, E_b : the average V-V/SIA-SIA binding energy at the GB.

The GB energy of a pure GB, by definition, is given by:

$$E_{GB1} = [E_{GB}^{tot}(N) - N \times E_{coh}] / S_{GB}, \quad (1)$$

The GB energy of the GB with a certain number of defects is given by:

$$E_{GB2} = [E_{GB}^{tot}(N \pm n) - (N \pm n) \times E_{coh}] / S_{GB}, \quad (2)$$

The energy difference is:

$$\begin{aligned} \Delta E_{GB} &= E_{GB2} - E_{GB1} = [E_{GB}^{tot}(N \pm n) - E_{GB}^{tot}(N) \mp n \times E_{coh}] / S_{GB} \\ &= \left[\frac{E_{GB}^{tot}(N \pm n) - E_{GB}^{tot}(N)}{n} \mp E_{coh} \right] n / S_{GB}, \\ &= \left[\frac{E_{GB}^{tot}(N \pm n) - E_{GB}^{tot}(N)}{n} \mp E_{coh} \right] C \end{aligned} \quad (3)$$

The V/SIA formation energy, by definition, is given by:

$$E_{SIA/Vf}^{GB} = E_{GB}^{tot}(N \pm 1) - E_{GB}^{tot}(N) \mp E_{coh}, \quad (4)$$

In Eq. 3, the term $\frac{E_{GB}^{tot}(N \pm n) - E_{GB}^{tot}(N)}{n}$ means the average energy variation induced by the adding of n defects. In Eq. 4, the term $E_{GB}^{tot}(N \pm 1) - E_{GB}^{tot}(N)$ means the energy variation induced by adding of one defect.

If there is no interaction among defects, the two terms would be the same. In this case, we obtain:

$$\Delta E_{GB} = E_{SIA/Vf}^{GB} \times C, \quad (5)$$

If there is interaction among defects, then we obtain:

$$\Delta E_{GB} \approx (E_{SIA/Vf}^{GB} - fl \times E_b) \times C, \quad (6)$$

where fl is approximately the fraction of defects pairs relative to the total number of defects.

From Eqs. 5 and 6, one could see the linear dependence of the GB energy on the defects concentration at the GB.

Acknowledgments

This work was supported by the National Key Research and Development Program of China (Grant Nos.: 2017YFE0302400, 2018YFE0308102, 2017YFA0402800), the National Natural Science Foundation of China (Nos.:11735015, 51871207, 51671185, 51771181, and 51971212, U1832206, 11575229), and by the Center for Computation Science, Hefei Institutes of Physical Sciences.

Supplementary references

- [S1] D. Chen, J. Wang, T. Chen, L. Shao, Defect annihilation at grain boundaries in alpha-Fe. *Sci. Rep.* 3 (2013) 1450.
- [S2] M.I. Mendelev, S. Han, D.J. Srolovitz, G.J. Ackland, D.Y. Sun, M. Asta, Development of new interatomic potentials appropriate for crystalline and liquid iron. *Philos. Mag.* 83 (2003) 3977–3994.
- [S3] J.F. Ziegler, M.D. Ziegler, J.P. Biersack, SRIM C The stopping and range of ions in matter, *Nucl. Instrum. Methods Phys. Res. B* 268 (2010) 1818–1823.
- [S4] M. Rose, A.G. Balogh, H. Hahn, Instability of irradiated induced defects in nanostructured materials. *Nucl. Instr. and Meth. B* 127 (1997) 119–122.
- [S5] C.M. Barr, N. Li, B.L. Boyce, K. Hattar, Examining the influence of grain size on radiation tolerance in the nanocrystalline regime. *Appl. Phys. Lett.* 112 (2018) 181903.
- [S6] J. Li, K.Y. Yu, Y. Chen, M. Song, H. Wang, M.A. Kirk, M. Li, X. Zhang, In situ study of defect migration kinetics and self-healing of twin boundaries in heavy ion irradiated nanotwinned metals. *Nano Lett.* 15 (2015) 2922–2927.
- [S7] C. Sun, M. Song, K.Y. Yu, Y. Chen, M. Kirk, M. Li, H. Wang, X. Zhang, In situ evidence of defect cluster absorption by grain boundaries in Kr ion irradiated nanocrystalline Ni. *Metall. Mater. Trans. A* 44A (2013) 1966–1974.
- [S8] Y. Chimi, A. Iwase, N. Ishikawa, M. Kobiyama, T. Inami, S. Okuda, Accumulation and recovery of defects in ion-irradiated nanocrystalline gold. *J. Nucl. Mater.* 297 (2001) 355–357.
- [S9] K.Y. Yu, Y. Liu, C. Sun, H. Wang, L. Shao, E.G. Fu, X. Zhang, Radiation damage in helium ion irradiated nanocrystalline Fe. *J. Nucl. Mater.* 425 (2012) 140–146.
- [S10] O. El-Atwani, J.E. Nathaniel II, A.C. Leff, B.R. Muntifering, J.K. Baldwin, K. Hattar, M.L. Taheri, The role of grain size in He bubble formation: Implications for swelling resistance. *J. Nucl. Mater.* 484 (2017) 236–244.
- [S11] B. Muntifering, Y. Fang, A.C. Leff, A. Dunn, J. Qu, M.L. Taheri, R. Dingreville, K. Hattar, In situ transmission electron microscopy He⁺ implantation and thermal aging of nanocrystalline iron. *J. Nucl. Mater.* 482 (2016) 139–146.

- [S12] W.B. Liu, J.H. Zhang, Y.Z. Ji, L.D. Xia, H.P. Liu, D. Yun, C.H. He, C. Zhang, Z.G. Yang, Comparative study of He bubble formation in nanostructured reduced activation steel and its coarsen-grained counterpart. *J. Nucl. Mater.* 500 (2018) 213–219.
- [S13] M. Song, Y.D. Wu, D. Chen, X.M. Wang, C. Sun, K.Y. Yu, Y. Chen, L. Shao, Y. Yang, K.T. Hartwig, X. Zhang, Response of equal channel angular extrusion processed ultrafine-grained T91 steel subjected to high temperature heavy ion irradiation. *Acta Mater.* 74 (2014) 285–295.
- [S14] C. Du, S. Jin, Y. Fang, J. Li, S. Hu, T. Yang, Y. Zhang, J. Huang, G. Sha, Y. Wang, Z. Shang, X. Zhang, B. Sun, S. Xin, T. Shen, Ultrastrong nanocrystalline steel with exceptional thermal stability and radiation tolerance. *Nat. Commun.* 9 (2018) 5389.
- [S15] C. Sun, S. Zheng, C.C. Wei, Y. Wu, L. Shao, Y. Yang, K.T. Hartwig, S.A. Maloy, S.J. Zinkle, T.R. Allen, H. Wang, X. Zhang, Superior radiation-resistant nanoengineered austenitic 304L stainless steel for applications in extreme radiation environments. *Sci. Rep.* 5 (2015) 7801.
- [S16] N. Li, J. Wang, Y. Q. Wang, Y. Serruys, M. Nastasi, A. Misra, Incoherent twin boundary migration induced by ion irradiation in Cu. *J. Appl. Phys.* 113 (2013) 023508.
- [S17] Y. Chen, J. Li, K.Y. Yu, H. Wang, M.A. Kirk, M. Li, X. Zhang, In situ studies on radiation tolerance of nanotwinned Cu. *Acta Mater.* 111 (2016) 148–156.
- [S18] W. Han, E.G. Fu, Irradiation damage of single crystal, coarse-grained, and nanograined copper under helium bombardment at 450 °C. *J. Mater. Res.* 28 (2013) 2763–2770.
- [S19] G.M. Cheng, W.Z. Xu, Y.Q. Wang, A. Misra, Y.T. Zhu, Grain size effect on radiation tolerance of nanocrystalline Mo. *Scr. Mater.* 123 (2016) 90–94.
- [S20] O. El-Atwani, K. Hattar, J.A. Hinks, G. Greaves, S.S. Harilal, A. Hassanein, Helium bubble formation in ultrafine and nanocrystalline tungsten under different extreme conditions. *J. Nucl. Mater.* 458 (2015) 216–223.
- [S21] O. El-Atwani, A. Suslova, T.J. Novakowski, K. Hattar, M. Efe, S.S. Harilal, A. Hassanein, In-situ TEM/heavy ion irradiation on ultrafine-and nanocrystalline-grained tungsten: Effect of 3 MeV Si, Cu and W ions. *Mater. Charact.* 99 (2015) 68–76.
- [S22] O. El-Atwani, E. Esquivel, M. Efe, E. Aydogan, Y.Q. Wang, E. Martinez, S.A. Maloy, Loop and void damage during heavy ion irradiation on nanocrystalline and grained tungsten: Microstructure, effect of dpa rate, temperature, and grain size. *Acta Mater.* 149 (2018) 206–219.
- [S23] O. El-Atwani, J.A. Hinks, G. Greaves, S. Gonderman, T. Qiu, M. Efe, J.P. Allain, In-situ TEM observation of the response of ultrafine- and nanocrystalline-grained tungsten to extreme irradiation environments. *Sci. Rep.* 4 (2014) 4716.
- [S24] O. El-Atwani, E. Esquivel, E. Aydogan, E. Martinez, J.K. Baldwin, M. Li, B.P. Uberuaga, S.A. Maloy, Unprecedented irradiation resistance of nanocrystalline tungsten with equiaxed nanocrystalline grains to dislocation loop accumulation. *Acta Mater.* 165 (2019) 118–128.

